

Dissertation
submitted to the
Combined Faculties of the Natural Sciences and
Mathematics
of the Ruperto-Carola-University of Heidelberg, Germany
for the degree of
Doctor of Natural Sciences

Put forward by
Jonas Frings
born in: Siegburg
Oral examination: 11 July 2018

Structure and evolution of simulated dwarf galaxies and Milky Way satellites in Cold and Warm dark matter models

Referees: Prof. Dr. Andrea Valerio Macciò
Prof. Dr. Björn Malte Schäfer

Aufbau und Entwicklung simulierter Zwerggalaxien und Satellitengalaxien der Milchstraße in kalten und warmen Modellen dunkler Materie

Wir verfügen heute über detaillierte Beobachtungsdaten der Satellitengalaxien und Zwerggalaxien in der Umgebung der Milchstraße, die sich hervorragend dazu eignen, das Standardmodell der Kosmologie und Strukturentstehung, das Λ CDM-Modell, zu überprüfen. Zunächst stelle ich 27 hydrodynamische Simulationen mit einer Virialmasse zwischen 5×10^8 und $10^{10} M_{\odot}$ vor, die dazu dienen sollen, die Eigenschaften von Zwerggalaxien vor ihrer Akkretion auf einen der Milchstraße ähnlichen Halo zu untersuchen. Die simulierten Galaxien befolgen die beobachteten Relationen zwischen mittlerer Metallizität und Sternenmasse sowie Geschwindigkeitsdispersion und Größe. Bedingt durch die Zufälligkeit der von Kollisionen getriggerten Sternentstehung, entsteht eine große Streuung um die Sternenmasse-Halomasse-Relation. In Galaxien, deren Masse unter $10^6 M_{\odot}$ liegt, ist das stellare Feedback nicht stark genug, um die Halostruktur zu beeinflussen, und daher bleibt deren zentrales Dichteprofil spitz. Sieben ausgewählte Halos wurde daraufhin als Startbedingungen für Simulationen zur Untersuchung der Interaktion zwischen Satellitengalaxien und einem Zentralhalo der Masse der Milchstraße verwendet. Der Masseverlust durch Gezeitenkräfte erzeugt flache Geschwindigkeitsdispersionsprofile und verringert die Zirkulargeschwindigkeit effektiv bis zu einem Radius von 0.5 kpc, ohne dabei zu einem Verlust größerer Mengen Sterne zu führen. Zusätzlich führt der Masseverlust zu steileren zentralen Profilen der Dichteverteilung der dunklen Materie. Um die Auswirkungen von warmer dunkler Materie auf Zwerggalaxien und Satellitengalaxien zu untersuchen, wiederholte ich die Simulationen in einem 3 keV-Szenario warmer dunkler Materie. Dafür präsentiere ich Simulationen von 21 Halos, die sowohl in kalter (KDM) als auch in warmer dunkler Materie (WDM) durchgeführt wurden. In WDM wird die kritische Halomasse für Sternentstehung zu größeren Massen verschoben, wobei die Simulationen, in denen Galaxien entstehen, die üblichen Relationen, ebenso wie KDM-Galaxien, erfüllen. Allerdings verzögert WDM die Sternentstehung und lässt KDM-Galaxien um 2 Gyr älter erscheinen. Während die Konzentrationen in WDM-Halos deutlich geringer sind, ist das zentrale Dichteprofil der dunklen Materie im unteren Massenbereich geringfügig steiler. Für vier Halos (in WDM und KDM) simulierte ich erneut deren Entwicklung als Satelliten der Milchstraße. WDM-Halos leiden mehr unter dem Massenverlust durch die Gezeitenkräfte wegen ihrer geringeren Konzentrationen. Die Überlebenswahrscheinlichkeit hingegen ist nicht unbedingt geringer = dank des steileren zentralen Dichteprofiles. Wieder enden WDM- und KDM-Zwerggalaxien mit sehr steilen Dichteprofilen, nachdem sie ihre Entwicklung als Satellitengalaxien vollzogen haben. Letzendlich komme ich zum Schluss, dass die Voraussagen meiner Simulationen, vor dem Hintergrund der aktuellen Beobachtungsdaten, das Λ CDM-Modell nicht Frage stellen. Lediglich eine eindeutige Beobachtung eines flachen zentralen Dichteprofiles in einer Galaxie mit einer sehr geringen Masse würde uns zwingen das Modell dunkler Materie zu überdenken. Auch WDM stellt keine Lösung zu diesem Problem dar.

Structure and evolution of simulated dwarf galaxies and Milky Way satellites in Cold and Warm dark matter models

The satellite galaxies and dwarf galaxies in the neighborhood of the Milky Way provide us with detailed observations that can be used to test our standard model of cosmology and structure formation, the Λ CDM model. I present a sample of 27 cosmological hydrodynamical simulations with virial masses between 5×10^8 and $10^{10} M_{\odot}$ that are aimed to study the properties of dwarf galaxies before accretion. The simulated galaxies are able to reproduce observed scaling relations like the dispersion - size and metallicity - stellar mass relation. The stochasticity of merger induced star formation causes a large scatter in the stellar mass - halo mass relation. In galaxies of stellar masses below $10^6 M_{\odot}$ stellar feedback is unable to affect the dark matter halo and hence those galaxies retain a cuspy profile. A subsample of 7 halos is used as initial conditions for simulations of satellite - host galaxy interactions in a Milky Way mass halo. The mass removal due to tidal forces creates flat stellar velocity dispersion profiles and efficiently decreases the circular velocity at 0.5 kpc without stripping a large amount of stars. Additionally the stripping seems to happen in a way that effectively steepens the central dark matter density slope. To investigate the effects of warm dark matter on dwarf galaxies and Milky Way satellites I repeat the study in a 3 keV warm dark matter scenario. I present the simulations of 21 halos in both CDM and WDM. In WDM the critical halo mass for the onset of star formation is shifted towards higher masses, while the simulations that do produce stars, reproduce the same scaling relations as their CDM counterparts. However, WDM seems to delay the bulk star formation, making galaxies in CDM look about 2 Gyr older. While halo concentrations are significantly lower in WDM, the central dark matter density slope is slightly steeper for the low mass end. For four halos (in WDM and CDM) I present their evolution as Milky Way satellites. In contrast to the CDM halos, WDM halos are stripped more effectively due to their lower concentrations. The survival probability for WDM satellites, on the other hand, is not necessarily lower because of their steeper central slope. Again, the WDM as well as CDM satellites end up with very cuspy profiles after being stripped. I come to the conclusion that the predictions from my simulations do not challenge the Λ CDM compared to current observational data of dwarf galaxies and Milky Way satellites. An observation of a cored density profile in one of the very low mass objects, however, would force us reconsider the dark matter model. Also WDM would pose a solution to this problem.

“War der Förster da?”

Peter Birschen, Tonale (2016)

Contents

1	Introduction	0
I	Theoretical foundations	2
2	Cosmology	3
2.1	Friedmann Cosmology	3
2.1.1	Gravity	3
2.1.2	Isotropy and homogeneity	3
2.1.3	Evolution equations	4
2.2	The Cosmological Standard Model	5
2.2.1	Radiation	6
2.2.2	Matter	6
2.2.2.1	Baryons	6
2.2.2.2	Dark matter	7
2.2.3	The Cosmological constant	7
2.3	Evidence and properties of dark matter	8
2.3.1	Evidence for dark matter	8
2.3.2	Properties of dark matter	8
2.3.3	Production mechanisms and dark matter candidates	10
3	Structure formation	11
3.1	Linear structure formation	13
3.1.1	Evolution of the linear power spectrum	13
3.2	Non-linear structure formation	15
3.2.1	Spherical collapse	15
3.2.2	The Zel'dovich approximation	16
3.3	Galaxies	16
3.3.1	Galaxy properties	16
3.3.1.1	Morphology and mergers	16
3.3.1.2	Dark matter structure	17
3.3.2	Galaxy formation	17
3.3.2.1	Gas cooling	18
3.3.2.2	Star formation and feedback	18

3.3.3	Small scale challenges of Λ CDM	19
3.3.3.1	The missing satellite problem	19
3.3.3.2	The cusp-core tension	21
3.3.3.3	The too big to fail problem	21
3.4	Structure formation in WDM	23
3.4.1	Constraints on WDM relic mass by studies of the Lyman-alpha forest	23
3.4.2	The linear power spectrum in WDM	23
3.4.3	Halo structures in WDM	24
4	Numerical simulation of structure formation	27
4.1	Gravity	27
4.1.1	Tree algorithm	27
4.1.2	Particle mesh	28
4.2	Smoothed particle Hydrodynamics	28
II	Numerical methods	30
4.3	Generation of Initial Conditions	31
4.4	SPH and gravity code	31
III	Cold dark matter	33
5	Introduction	35
6	Dwarf galaxies	37
6.1	Simulations	37
6.1.1	Initial Conditions	37
6.1.2	Hydrodynamical code	38
6.2	Results	40
6.2.1	Dark, stellar and gas masses at $z=1$	40
6.2.2	Galaxy properties and scaling relations	43
6.2.3	Star formation rate and halo response	47
6.2.4	Diversity of star formation histories and the DM assembly	52
6.2.5	Dark halos	53
7	Milky Way satellites	56
7.1	Simulations	56
7.1.1	Satellite initial conditions	56
7.1.2	Central object parametrization	56

7.1.3	Orbits	57
7.1.4	Ram pressure	58
7.2	Results	59
7.2.1	Rotational support	59
7.2.2	Environmental effects on galaxy properties	62
7.2.2.1	Evolution of the dark matter profile	72
7.2.2.2	Central dark matter density slope and satellite survival	76
IV	Warm dark matter	79
8	Introduction	81
9	Dwarf galaxies	82
9.1	Simulations	82
9.2	Results	84
9.2.1	Halo masses	84
9.2.2	Star formation and luminous fraction	85
9.2.3	Scaling relations	88
9.2.4	Stellar ages	88
9.2.5	Halo structure	91
10	Milky Way satellites	93
10.1	Simulations	93
10.2	Results	93
10.2.1	Mass loss	93
10.2.2	Central dark matter density slope	95
V	Summary and conclusions	98
10.3	Summary	99
10.4	Final conclusions and outlook	102
10.5	List of Figures	105
List of Figures		110
10.6	List of Tables	110
List of Tables		111
11	Bibliography	112

1 Introduction

In the most successful model for the formation and evolution of the Universe, gravity is described by general relativity under the presence of a cosmological constant Λ (Riess et al., 1998; Perlmutter et al., 1999) and with collisionless, Cold Dark Matter (CDM) dominating the matter component (Peebles, 1984). Structure formation in this model is supposed to happen in a hierarchical manner, where small dark matter structures (so-called halos) collapse first under the influence of their own gravity and subsequently merge to form more massive structures (White & Rees, 1978; Blumenthal et al., 1984). The gas, initially coupled to the photon gas and thus unable to form any structures yet, can evolve freely as soon as the first atoms form. Accreted by the potential wells of the dark matter halos, the gas is able to cool and eventually reach densities high enough to ignite star formation.

On large ($>Mpc$) scales this model is very successful in predicting the observed structure of the Universe. However, on the low mass end of the galaxy population it has been often claimed to struggle reproducing observed properties of the smallest galaxies. The most important challenges of the Λ CDM model on small scales are the missing satellites problem (Klypin et al., 1999; Moore, 1994), the cusp-core tension (Flores & Primack, 1994; Moore, 1994; Oh et al., 2015) and the too-big-to-fail problem (Boylan-Kolchin et al., 2011).

To study structure formation at the scale of dwarf galaxies, baryonic effects, that themselves are not fully understood yet, like gas cooling processes, star formation and feedback play an important role. However, those effects can be modeled in advanced hydrodynamical simulations including sub-grid models for galaxy formation.

In this thesis I want to study the formation of smallest galaxies using hydrodynamical cosmological simulations and ascertain if current observations force us to reconsider our cosmological standard model.

The best studied objects with detailed observational data at the dwarf galaxies scale are the satellites of the Milky Way and M31. Therefore I want to investigate the environmental effects on the satellite properties, besides the baryonic effects, as well as the interplay between the two.

The thesis is structured as follows: in part I I lay the theoretical foundations for this thesis by introducing the concept of the standard cosmological model and structure formation therein. In the following part (part II) I quickly

describe the numerical code used for the setup and evolution of the initial conditions before I present the results of the simulations of dwarf galaxies and Milky Way satellites in a CDM model and their implications in part [III](#). The results of a similar study in a WDM scenario and their interpretations are stated in part [IV](#) and I finally summarize the thesis and draw the conclusions in part [V](#).

Part I
Theoretical foundations

2 Cosmology

2.1 Friedmann Cosmology

2.1.1 Gravity

As gravity has infinite range and can not be shielded it is the driver the of the evolution of our Universe. This makes the publication of Einstein's theory of general relativity ([Einstein, 1916](#)) the starting shot for modern cosmology. Einstein's field equations

$$G_{\alpha\beta} = \frac{8\pi G}{c^4} T_{\alpha\beta} + \Lambda g_{\alpha\beta} \quad (2.1)$$

couple the energy-momentum tensor T to a combination of second derivatives of the metric tensor g that describes the geometry of space-time. There also appears a constant term Λ in the equation that is referred to as the cosmological constant. Assuming a perfect fluid, the energy-momentum tensor expressed by its density ρ and pressure p

$$T_{\alpha\beta} = (p + \rho c^2) u_\alpha u_\beta - p g_{\alpha\beta} \quad (2.2)$$

where u is the 4-velocity. Though providing the link between matter content of the universe and space-time geometry, a general solution to the field equations can only be found assuming certain symmetries.

2.1.2 Isotropy and homogeneity

There are two fundamental assumptions that simplify (2.1) drastically for cosmological purposes and lead to the so called Friedmann equations: If averaged over sufficiently large scales our Universe is isotropic, i. e. observable properties do not depend on direction. Further, the cosmological principle states that there is no preferred position in the Universe. Taken together, these assumption are often referred to as isotropy and homogeneity of the Universe (the latter is a consequence of the cosmological principle and isotropy). Given these two properties of the Universe and choosing spherical coordinates the line element can be written in the form

$$ds^2 = c^2 dt^2 + a^2(t) [dr^2 + S_K^2(r) d\omega^2]. \quad (2.3)$$

with the radial function

$$S_K(r) = \begin{cases} K^{-1/2} \sin(K^{1/2}r), & K > 0 \\ r, & K = 0 \\ |K|^{-1/2} \sin(|K|^{1/2}r), & K < 0. \end{cases} \quad (2.4)$$

The time dependent function $a(t)$ called the scale factor which we chose to be $a(t = t_0) = a_0 = 1$ today. All other quantities evaluated today will just be indicated by the underscore 0. The value of K is linked to the global spatial curvature of the space-time. Besides a spatially flat space-time ($K = 0$) in principle also a spherical ($K > 0$) or hyperbolic space-time ($K < 0$) is allowed. In the upper form the metric is called the Friedmann-Lemaître-Robertson-Walker (FLRW) metric.

2.1.3 Evolution equations

For a Universe filled with a perfect fluid and a geometry described by the FLRW metric, Einstein's equations collapse to two independent components that can be rewritten to the Friedmann equations ([Friedmann, 1922](#))

$$\left(\frac{\dot{a}}{a}\right)^2 = \frac{8\pi G}{3}\rho(t) + \frac{\Lambda c^2}{3} - \frac{kc^2}{a^2} \quad (2.5)$$

and

$$\frac{\ddot{a}}{a} = -\frac{4\pi G}{3}\left(\rho(t) + \frac{3p(t)}{c^2}\right) + \frac{\Lambda c^2}{3}. \quad (2.6)$$

These equations describe the evolution of the scale factor given the density and pressure of the fluid. Combining both equations leads to the adiabatic equation

$$\frac{d}{dt}(a^3 \rho c^2) + p \frac{d}{dt}a^3 = 0 \quad (2.7)$$

that can be solved for the density assuming an equation of state. For $p = w\rho c^2$ with a constant equation of state parameter w the density as a function of the scale factor is given by

$$\rho(a) = \rho_0 a^{-3(1+w)}. \quad (2.8)$$

Because our Universe consist of several components i with different equations $p_i = w_i \rho_i c^2$ of state it is convenient to rewrite the Friedmann equations in

terms of the Hubble function $H(t) = \frac{\dot{a}}{a}$ and the density parameters Ω_i . With the critical density $\rho_{c,0} = \frac{3H_0^2}{8\pi}$ where $H(t = t_0) = H_0$ is the value of the Hubble function today, the Hubble parameter, the density parameter is defined by $\Omega_i = \frac{\rho_i}{\rho_{c,0}}$. Furthermore absorbing the curvature and the cosmological constant into the unit free parameters

$$\Omega_k = -\frac{Kc^2}{H_0^2} a^{-2} \quad (2.9)$$

and

$$\Omega_\Lambda = \frac{\Lambda c^2}{3H_0^2} \quad (2.10)$$

one can write the first Friedmann equation as

$$\begin{aligned} H^2(a) &= H_0^2 \sum_i \Omega_i \\ &= H_0^2 \sum_i \Omega_{i,0} a^{-3(1+w_i)}. \end{aligned} \quad (2.11)$$

A direct consequence of (2.11) is that the sum of all density parameters today is equal to one: $\sum_i \Omega_{i,0} = 1$.

2.2 The Cosmological Standard Model

The cosmological standard model assumes a flat Universe that evolved from an initially very hot and dense state through several epochs of expansion in which it adiabatically cools down. In radiation and matter domination the expansion was decelerated while currently it is in a state of accelerated expansion dominated by a cosmological constant. In the last few decades more and more cosmological probes were discovered and more observational data could be analyzed and we know the values of the cosmological parameters to an incredible precision today. The most important probes today are the cosmic microwave background (CMB), supernovae type Ia, weak lensing of the CMB and galaxies. The cosmological parameters from the 2015 results of the Planck collaboration (Ade et al., 2016) are:

$$\begin{aligned} H_0 &= 67.8 \text{ km s}^{-1} \text{ Mpc}^{-1} \\ \Omega_{r,0} &= 8.5 \times 10^{-5} \\ \Omega_{m,0} &= 0.3175 \\ \Omega_\Lambda &= 0.6824. \end{aligned} \quad (2.12)$$

The knowledge of these parameters fixes the evolution of the Universe in principle back to a singular state. However the physics at the high energy densities can not be properly described by general relativity and quantum field theory, so one can only trace back the evolution of the Universe to an hot and dense initial state. An inflationary period at the very beginning of the Universe is an scenario that solves a lot of problems concerning causality, flatness and seed perturbations for structure formation (Linde, 2008). The standard cosmological model, however, only describes the evolution after a possible inflationary epoch under the influence of the three components: radiation, matter and a cosmological constant.

2.2.1 Radiation

In a cosmological sense radiation is defined by the equation of state $p_r = \frac{1}{3}\rho_r c^2$. This is the case for all relativistic particles (both bosons and fermions), e.g. photons or neutrinos. The equation of state implies the density evolution $\rho_r(a) \propto a^{-4}$ making the radiation the dominating fraction of the energy density in the Universe at early stages. Using the second Friedmann equation (2.6) we can see that $\ddot{a} < 0$ and the expansion is decelerating.

2.2.2 Matter

For non-relativistic matter however the pressure is negligible compared to the rest mass energy density, the equation of state parameter is then given by $w_m = 0$ and the density scales like $\rho_m \propto a^{-3}$. Matter takes over being the dominant component at the scale factor $a_{\text{eq}} = \frac{\Omega_r}{\Omega_m}$. During the epoch of matter domination the expansion of the Universe is still decelerating.

2.2.2.1 Baryons

The origin of baryons in our Universe is still vague because if thermally produced in the early Universe they should soon have annihilated with their simultaneously produced anti-particles. One explanation could be an interaction that violates CP symmetry in quantum field theory and that does not conserve the baryon number. From the initial quark-gluon-plasma Protons and Neutrons form and heavier elements up to Lithium can be stably build as the Universe cools down. All the heavier elements are only produced fusion in stars by or in supernovae explosions by neutron capture. At the high temperatures in the early Universe the thermal velocities of protons and electrons are still too high to form atoms and the plasma is in thermal equilibrium with the photon gas. As the Universe cools down atoms can form and the photons,

maintaining their thermal distribution, can freely stream through space. This signature of the so called recombination of proton and electrons is measurable today as the Cosmic Microwave Background (CMB) which has cool down to a temperature of $T_{\text{CMB}} \approx 2.735$ K. However, estimates of the amount of baryons in the local Universe only account for around 5% of the total energy content of the universe which leaves 26% of matter to be of a non-baryonic kind.

2.2.2.2 Dark matter

With baryons only covering on sixth of the matter content of the Universe there has to be another form of matter with $w = 0$ that we called dark matter to make up for that. For the Friedmann equations the distinction between baryons and dark matter is not necessary and properties of this species beyond the equation of state does not play a role. But dark matter is also essential for structure formation, galaxy formation and observed kinematics of stars and galaxies where observational data are able to constrain dark matter properties. Dark matter is treated in detail in section 2.3.

2.2.3 The Cosmological constant

The cosmological constant is a mathematical freedom in the derivation of Einstein's field equations that was later used by Einstein to enforce an at that time plausible idea of a static Universe. After the discovery of the expanding Universe by [Hubble \(1929\)](#) the idea of a cosmological constant was dropped. But it has had its comeback when in the 1990's analysis of supernovae of type Ia data supported the idea that the Universe is currently in a state of accelerated expansion ([Perlmutter et al., 1998](#); [Schmidt et al., 1998](#)) which is also confirmed by recent experiments ([Ade et al., 2016](#)). By absorbing the cosmological constant into a density parameter with an equation of state parameter $w = -1$ the cosmological constant can also be interpreted as a contribution to the energy content of the Universe instead of an artifact of gravity. A more general concept, called dark energy, has a free equation of state $p_{\text{de}} = w_{\text{de}}(a)\rho_{\text{de}}c^2$ which in the case of $w_{\text{de}}(a) = -1$ mimics a cosmological constant. Dark energy again can be interpreted as a new contribution to the energy density or in the case of $w_{\text{de}}(a) \neq -1$ a deviation from general relativity.

2.3 Evidence and properties of dark matter

2.3.1 Evidence for dark matter

The first events that led to the idea of dark matter were the measurement of kinematics of stars in the Milky Way by [Kapteyn \(1922\)](#) and [Oort \(1932\)](#) and of galaxies of the Coma cluster performed by [Zwicky \(1933\)](#). The kinematics did not fit to the potential generated by the estimated stellar and gas mass but suggested that there is much more mass present that is not detectable, i.e. dark. Observations of galaxy rotation curves that do not fall off as expected from the observable mass distributions ([Rubin et al., 1980](#)) but stay constant, the missing matter to account for $\Omega_m = 0.3175$, the necessity of dark matter for efficient structure formation (see [3](#)) and observations like the Bullet cluster (see [fig. 2.3.1](#)) established the dark matter theory in the late 20th century. In the Bullet cluster two galaxy clusters that are dominated by hot intergalactic gas in their baryonic component collide. While the galaxies with negligible chance of a collision just pass by each other, the gas of the two clusters, shown in magenta in [fig. 2.3.1](#), interacts and lags behind the galaxy distributions. However being just sensitive to the gravitational potential, the mass distribution can be reconstructed using gravitational lensing ([Clowe et al., 2006](#)). This lensing mass is shown in blue and is consistent with the galaxy distributions of the two clusters. But keeping in mind that the mass of the galaxies is tiny compared to the intergalactic gas, there has to be a large fraction of dark matter in clusters contributing to the lensed gravitational potential. Although dark matter explains the observations listed above surprisingly well a dark matter particle has not yet been found even under large effort. Until that happens dark matter still stays speculative even if alternative theories that in most cases propose deviation from the standard gravity model like MOND ([Milgrom, 1983](#)) never had the success like dark matter has in predicting all the phenomena listed above.

2.3.2 Properties of dark matter

Dark matter can give an explanation to all the observations listed in [2.3.1](#) if the dark matter particle has the following properties.

First of all the dark matter particle has to be massive because a relativistic particle would prevent any structure formation. The smallest dark matter structures whose existence can be deduced from observations are dark matter halos of dwarf galaxies. Since early fluctuations in the dark matter density field

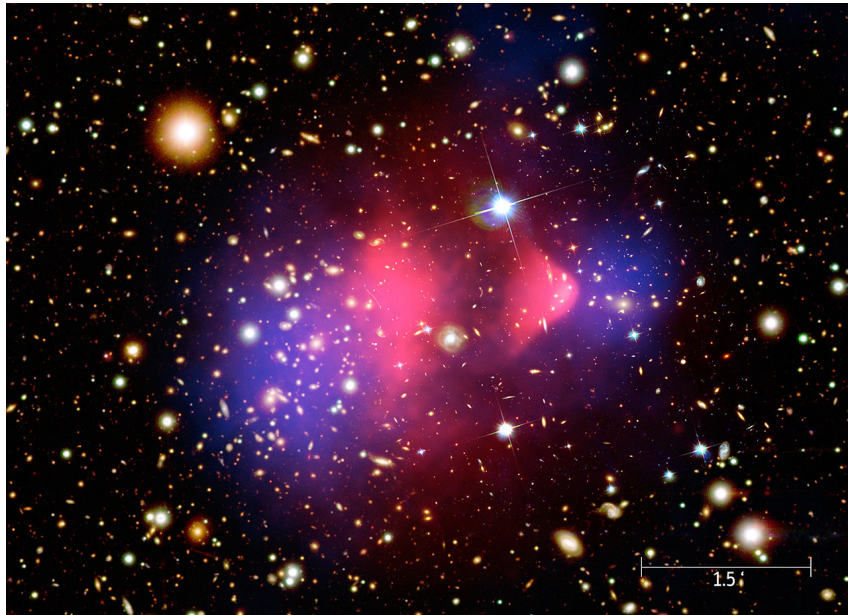


Figure 2.1: The bullet cluster shows the collision of two galaxy clusters, the lensing mass is shown in blue, X-rays from the hot gas in magenta.

on scales below a critical scale length λ_{dm} defined (see [Bartelmann \(2012\)](#)) by

$$\lambda_{\text{dm}} = \sqrt{\frac{\pi}{a^2 G \rho_0 \langle v^2 \rangle}} \quad (2.13)$$

with the average density ρ_0 are damped efficiently due to the velocity dispersion $\langle v^2 \rangle$ of dark matter, this already puts a lower bound on $\langle v^2 \rangle$. Depending on the velocity dispersion dark matter can be categorized to cold, warm and hot dark matter. For Cold Dark Matter (CDM) the velocity dispersion is small enough to have no effect even on the scales of the smallest observed galaxies. Hot dark matter on the other side has a velocity dispersion high enough to make λ_{dm} larger than typical galaxy scales and thus making the formation of galaxies in a hierarchical bottom to top structure formation scenario (see section 3) impossible. That is why pure hot dark matter theories rely on a scenario where larger structures form first that later segment into galaxy size halos. However, this scenario is not supported by current observational data. Somewhere in between hot and cold dark matter with velocities that affect but does not prevent galaxy formation in a bottom to top scenario lies Warm Dark Matter (WDM). It may well be possible that dark matter does not consist of only one species but is e. g. a mixture of cold and warm dark matter.

Second, the interactions with baryonic matter and photons as well as the self interaction has to be very weak because no signals of dark matter have

been detected yet. Further, this property is needed in structure formation for the dark matter to be able to clump and form potential wells for the baryons before recombination (see 3).

Finally dark matter particles have to be sufficiently stable since we do observe consequences of the presence of dark matter today and decay rates are low enough to produce no detectable signal.

2.3.3 Production mechanisms and dark matter candidates

The dark matter production in the early Universe is considered to have happened in one of two ways. Either dark matter is produced thermally, i.e. produced by scattering or decay of particles in thermal equilibrium, or non-thermally from bosonic field coherent motion or decay of particles outside equilibrium (Baer et al., 2015). The production mechanism together with the particle mass fixes the free streaming length of the dark matter particles but generally, larger masses imply smaller free streaming lengths.

The most famous candidates for thermal production are the WIMPs (Weakly Interacting Massive Particles) that are predicted either by supersymmetry or other extensions of the standard model of particle physics. From the theoretical side the mass of WIMPs is expected to be of the order of a few GeV (Baer et al., 2015) making them viable candidates for CDM. For other scenarios however also lighter particles e.g. the light gravitino are predicted by these theories that can contribute to a WDM component (Viel et al., 2005).

Most important candidates for non-thermal production are axions that were originally postulated to solve the strong CP problem (Banerjee et al., 2003) and sterile neutrinos. While the axion mass is expected to be of the order of 10^{-4} eV they would still act as CDM because they are considered a zero momentum condensate (Peccei, 2008). Sterile or right-handed neutrinos could be produced via neutrino oscillations in the early Universe that have such a low production rate that thermal equilibrium cannot be established in the expanding Universe. With masses of the order of keV sterile neutrinos provide a good candidate for WDM (Viel et al., 2005).

3 Structure formation

Even though cosmology describes the evolution of an homogeneous and isotropic Universe, the observations of galaxy clusters, galaxies, the solar system and even ourselves is an inevitable proof of the existence of structure in our Universe. We know from the cosmic microwave background that the Universe at recombination was homogeneous down to a level of at least 10^{-4} (see fig. 3). These tiny perturbations can be explained by an inflationary epoch in the very early Universe. Inflation was originally proposed by Guth (1981) to solve the flatness and horizon problem of cosmology but also provides an answer for primordial density fluctuations. The sudden and enormous expansion spread regions in space that were in causal contact before inflation so efficiently that they had no chance to interact up to today. In that way quantum fluctuations in the primordial plasma could have been separated and turned to actual Gaussian perturbations in the energy density. Thus structures must have grown from these density fluctuation up to today where the density contrast $\delta = \frac{\rho - \rho_0}{\rho_0}$ with the average density $\rho_0 = \langle \rho \rangle$ for our solar system has a value of

$$\delta_{\text{sol}} \approx \frac{\rho_{\text{sol}}}{\rho_c} = \frac{1M_{\odot}}{(100 \text{ AU})^3 \rho_c} \approx 10^{16} \quad (3.1)$$

under the force of gravity. For the growth of structure to happen that fast one needs Ω_m to be of the order 0.3. With baryons only accounting for 5% of the energy content, this makes the existence of non-linear structures ($\delta > 1$) another evidence for dark matter.

To quantify structure formation in a statistical way one defines the power spectrum $P(k)$ of the density contrast in Fourier space

$$\delta(\vec{k}) = \int d^3r \delta(\vec{r}) \exp(i\vec{k}\vec{r}) \quad (3.2)$$

by

$$\langle \delta(\vec{k}) \bar{\delta}(\vec{k}') \rangle = (2\pi)^3 P(k) \delta_D(\vec{k} - \vec{k}'), \quad (3.3)$$

where δ_D is the Dirac delta distribution. Inflation predicts a primordial power spectrum of the form

$$P_i(k) \propto k^n \quad (3.4)$$

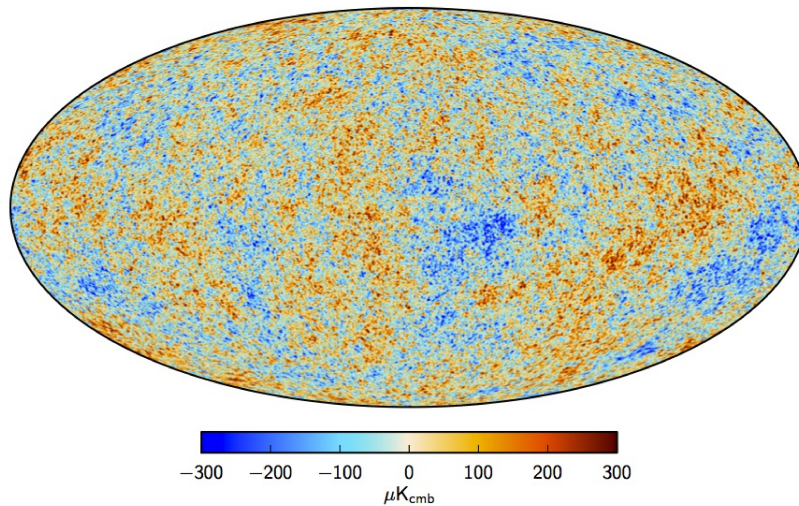


Figure 3.1: The cosmic microwave background temperature anisotropies by [Adam et al. \(2016\)](#).

with the spectral index n being close to 1. Analysis of the cosmic microwave background gives a value of $n = 0.965$ ([Ade et al., 2016](#)). Since initial density fluctuations most likely follow a Gaussian random field, the power spectrum already describes the whole statistic and therefore is an important observable.

The evolution of structures of a perfect fluid under gravity in the Newtonian limit is described by the following equations

$$\frac{\partial \rho}{\partial t} + \vec{\nabla}(\rho \vec{v}) = 0 \quad (3.5)$$

$$\frac{\partial \vec{v}}{\partial t} + (\vec{v} \vec{\nabla}) \vec{v} = -\frac{\vec{\nabla} p}{\rho} - \vec{\nabla} \Phi \quad (3.6)$$

$$\vec{\nabla}^2 \Phi = 4\pi G \rho \quad (3.7)$$

known as the continuity, Euler and Poisson equation, respectively. Here \vec{v} is the fluid velocity, Φ the Newtonian gravitational potential and G the gravitational constant. These equations however are coupled, non-linear, partial differential equations which in general cannot be solved analytically.

3.1 Linear structure formation

3.1.1 Evolution of the linear power spectrum

The most straight forward approach is to linearize the equations in terms of the background quantities $\rho_0 = \langle \rho \rangle$, $\vec{v}_0 = H\vec{r}$, $\Phi_0 = 0$ and linear perturbations $\delta = \frac{\delta\rho}{\rho_0}$, $\delta\vec{v}$, $\delta\Phi = \Phi$. Further using comoving coordinates $\vec{x} = \frac{\vec{r}}{a}$ and $\vec{u} = \frac{\vec{v}}{a}$ the equations can be rewritten as

$$\frac{\partial\delta}{\partial t} + \vec{\nabla}\vec{u} = 0 \quad (3.8)$$

$$\frac{\partial\vec{u}}{\partial t} + 2H\vec{u} = -\frac{\vec{\nabla}\delta p}{a^2\rho_0} - \frac{\vec{\nabla}\Phi}{a^2} \quad (3.9)$$

$$\vec{\nabla}^2\Phi = 4\pi G\rho_0 a^2 \delta. \quad (3.10)$$

Combining the equations (3.8) and going to Fourier space one can write down a single evolution equation for the density contrast

$$\frac{\partial^2\delta}{\partial t^2} + 2H\frac{\partial\delta}{\partial t} - \delta \left(4\pi G\rho_0 - \frac{c_s^2 k^2}{a^2} \right) = 0 \quad (3.11)$$

where the pressure has been replaced by an equation of state $\delta p = c_s^2 \rho_0 \delta$. Equation (3.11) introduces an important scale called the Jeans scale λ_J in the limit of $H = 0$. The solution is an oscillator with frequency

$$\omega = \sqrt{\frac{c_s^2 k^2}{a^2} - 4\pi G\rho_0} \quad (3.12)$$

which is real and describes an actual oscillation for scales smaller than λ_J

$$\frac{2\pi}{k} < \sqrt{\frac{c_s^2 \pi}{a^2 G\rho_0}} = \lambda_J \quad (3.13)$$

and becomes imaginary and describes growth or decay for scales larger than λ_J .

For a relativistic fluid like photons the same approach leads to

$$\frac{3}{4}\frac{\partial^2\delta}{\partial t^2} + \frac{3}{2}H\frac{\partial\delta}{\partial t} - \delta \left(4\pi G\rho_0 - \frac{c_s^2 k^2}{a^2} \right) = 0 \quad (3.14)$$

During radiation domination which last approximately until $z = 3700$ baryons are still ionized and coupled to the photon gas (recombination happens around $z = 1100$). Hence there is no formation of structures in baryonic component possible. For dark matter perturbation one has to distinguish between

super-horizon modes, i.e. modes exceeding the Hubble horizon $r_H = \frac{c}{H}$, and sub-horizon modes. While super-horizon modes can evolve freely and grow like $\delta \propto a^2$ in radiation domination sub-horizon modes very are efficiently damped. The Hubble function in radiation domination evolves like $H \propto a^{-4}$ (2.11) making the horizon grow like $\propto a^4$. Hence there is a range of modes that start growing like $\propto a^2$ then enter the horizon and where growth is damped.

When the matter domination epoch sets in both sub and super-horizon modes just like $\delta \propto a$ independent of wave number. At redshift $z = 1100$ when baryons finally decouple from photons they follow the potential of the dark matter overdensities that were able to form earlier. Thus without dark matter, structure formation of baryons would be delayed to such an extent that the model would fail to explain the abundance of structures observable today.

In general one writes the evolution of of the density contrast in terms of the growth factor

$$\delta(a) = D_+(a) \delta_0 \quad (3.15)$$

which, at later times can be well approximated (see Bartelmann (2012)) by

$$\frac{5a}{2} \Omega_m \left[\Omega_m^{\frac{4}{7}} - \Omega_\Lambda + \left(1 + \frac{\Omega_m}{2}\right) \left(1 + \frac{\Omega_\Lambda}{70}\right) \right]^{-1}. \quad (3.16)$$

The wavenumber dependent growth of modes is usually described by the transfer function $T(k, a)$. With the transfer function the evolution of the power spectrum can be expressed by the initial power spectrum

$$P(k, a) = T^2(k, a) P_i(k). \quad (3.17)$$

In the limit of large scales that did not enter the horizon during matter domination the power spectrum stays proportional to the initial power spectrum $P(k) \propto k^n \approx k$ while at tiny scales the power spectrum asymptotically approaches $P(k) \propto k^{-3}$. Thus the amplitude of the fluctuations given by $k^3 P(k)$ is growing towards smaller scales. This leads to the idea of hierarchical structure growth because smaller scales reach the non-linear regime earlier and eventually collapse earlier. Larger structures are primarily formed by minor (merging of small halos with the progenitor) and major (merging of two halos of comparable size) mergers. However so far we have only considered linear structure formation up to now. At least at a density contrast of $\delta = 1$ the linear description will break down and as shown in the beginning of section 3 for our solar system $\delta \approx 10^{16}$.

3.2 Non-linear structure formation

As shown at the beginning of section 3 the evolution equations for the density and velocity field (3.8) are coupled partial differential equations. Though not solvable analytically there are several approaches to investigate structure formation in the non-linear regime. Besides the numerical approach there is perturbation theory (for an overview see [Bertschinger \(2001a\)](#)), field theoretical approaches ([Bartelmann et al., 2014](#)) and some important simplifying concepts like spherical collapse, the Press-Schechter mass function ([Press & Schechter, 1974](#)) and the Zel'dovich approximation ([Zel'dovich, 1970](#)). I will quickly introduce the concept of spherical collapse and the Zel'dovich approximation in the beginning of this section while the numerical approach will be treated in detail in section 4.

3.2.1 Spherical collapse

The spherical collapse model studies the collapse of an homogeneous spherical overdensity embedded in an expanding background universe. Starting from the Newtonian equation of motion for the radius R of the overdensity

$$\frac{d^2R}{dt^2} = -\frac{GM}{R^2} \quad (3.18)$$

where M is the total mass of the overdensity one can show that for $R(t=0) = 0$ the radius initially following the expansion of the Universe will eventually reach a maximum value at the turn around time t_{ta} and collapse back to a singularity at $t_c = 2t_{\text{ta}}$. At this time the density contrast of the linearly evolved overdensity is $\delta_c = \delta(t_c) \approx 1.69$ and the collapsed structure is called a halo. From virial consideration, virialization of the halo is supposed to happen at an overdensity of $\Delta = 178$ defined by $\rho_{200} = \Delta\rho_0$. This number is often adopted to define the extend of overdensities in numerical simulation where one commonly uses $\Delta = 200$ in comparison to the critical density ρ_c to define the virial mass M_{200} and radius r_{200} of the halo by

$$M_{200} = 200 \rho_c \frac{4\pi}{3} r_{200}^3. \quad (3.19)$$

The Press-Schechter formalism ([Press & Schechter, 1974](#)) makes use of the spherical collapse model and gives an estimate on the number of collapsed structures at given mass bin by counting the overdensities that were able to exceed δ_c when starting from a Gaussian random field of overdensities.

3.2.2 The Zel'dovich approximation

The Zel'dovich approximation (Zel'dovich, 1970) relies on the following Ansatz: the particle trajectories can be described by the initial position x_i following the Hubble flow plus a time dependent displacement \vec{f}

$$\vec{r}(t) = a(t) \left(\vec{x}_i + D_+(a)\vec{f} \right) \quad (3.20)$$

and the displacement can be written as a gradient of scalar field $\vec{f} = \vec{\nabla}\Psi$ called the velocity potential *Psi*. The approximation breaks down when trajectories cross and the displacement can no longer be described by a single velocity potential. However this model can already predict that actual collapse of structures has to happen anisotropically and it has further applications like the generation of initial conditions for numerical simulations (see section 4.3).

3.3 Galaxies

Galaxies like the Milky Way are individual cosmological structures that were able to produce stars during the history of the Universe. Their virial mass ranges from a few 10^8 for dwarf galaxies to about $10^{13}M_\odot$ for the largest galaxies. More massive halos with masses larger than 10^{14} evolve to groups of galaxies called galaxy clusters which are the most massive collapsed structures in the Universe. Galaxies usually consist of three components: a dark matter halo, stars and interstellar gas.

3.3.1 Galaxy properties

3.3.1.1 Morphology and mergers

Galaxies show a large range of morphologies. The stars can form spherical components like a stellar halo and a dense central bulge, a stellar disk and more complex structures like spiral arms and bars. Due to angular momentum conservation the cold gas will initially settle into a rotation supported gaseous disk where the bulk of star formation takes place. However the disk can be perturbed through minor mergers to gradually build up the spherical and dispersion supported components or even completely destroyed by major mergers (Silk & Mamon, 2012). In this way the stochasticity of mergers provided an explanation for the range of morphologies. The more massive the halo is the more likely it has experienced a major merger and thus the fraction of elliptical, dispersion supported galaxies increase drastically at masses above $10^{11}M_\odot$ while at lower masses spiral (disk) galaxies are more common. Dwarf

galaxies however being so sensitive to mergers and feedback are often not able to preserve a disk and are mainly dispersion supported.

There is also substructure in the form of dark and luminous satellites present in the galactic halo. Satellite galaxies are, depending on their orbit, exposed to tidal forces and interactions with the gaseous halo (ram pressure) and disk and therefore can have properties that are very different from isolated galaxies. Star formation in those objects is in most cases completely quenched due to gas removal by ram pressure (Gunn & Gott, 1972).

3.3.1.2 Dark matter structure

Apart from the central dark matter halo numerical simulations of structure formation indicate that there is a large number of dark matter subhalos. This large amount of dark satellites lead to the so-called missing satellite problem that is treated in section 3.3.3. Dark matter only simulation indicate that there seems to be a universal density profile for dark matter halos. The Navarro–Frenk–White (NFW) profile (Navarro et al., 1996)

$$\rho(x) = \frac{\rho_0}{x(1+x)^2} \quad (3.21)$$

provides a decent model for the dark matter density distribution. Here $x = \frac{r}{r_s}$ and the normalization ρ_0 and the scale radius r_s are free parameters that have to be fitted to the distribution. The scale radius r_s describes transition between the $\rho \propto r^{-1}$ regime for $r \ll r_s$ and the $\rho \propto r^{-3}$ regime for $r \gg r_s$. The $\rho \propto r^{-3}$ dependence reproduced flat circular velocity profiles at large radii as observed in galaxy rotation curves (see section 2.3.2). The ratio of virial radius and scale radius defines the concentration of the halo.

$$c = \frac{r_{200}}{r_s}. \quad (3.22)$$

The value of the concentration in simulations of galaxy formation is of the order of 10, which means that the break in the density profile occurs at around 10% of the virial radius.

Even if simulations including baryons and galaxy formation physics show that the dark matter density profile is affected by the presence of baryons (Macciò et al., 2012b), the NFW profile still provides a good approximation and a useful characterization of the halo at scales large than the galaxy.

3.3.2 Galaxy formation

Baryonic structure formation starts at time of recombination that happens around $z = 1100$. For the first time in the age of the Universe baryons can

clump without being exposed to the pressure of the photon gas it was coupled to. Dark matter density perturbations were able to grow already before that and the baryons follow the potential wells created by the dark matter. This incident speeds up the formation baryonic structures massively.

3.3.2.1 Gas cooling

Since dark matter structure have a head start they collapse first to halos that further accrete the surrounding gas. The gas falling onto the halo is then shock heated to the virial temperature $T_{\text{vir}} \propto \frac{M_{200}}{r_{200}}$ and a hydrostatic equilibrium between gravity and the thermal gas pressure prevents the gas from collapsing further. Unlike dark matter the gas is able to lose energy and cool through the following processes:

- Bremsstrahlung of the ionized plasma $T > 10^6$ K
- helium atomic lines 5×10^4 K $< T < 10^6$ K
- hydrogen lines 10^4 K $< T < 5 \times 10^4$
- molecular hydrogen excitation $T < 10^4$ K (only at very high densities molecular hydrogen can form at such high temperatures)

Once gas cools the pressure decreases, the gaseous halo can collapse further, the gas is heated again and hydrostatic equilibrium can be reestablished. In that way gas reaches much higher densities in the centers of the potential wells than dark matter does.

3.3.2.2 Star formation and feedback

Given a sufficiently massive halo, at a certain density star formation ignites and the first generation of stars is formed. These stars, called Pop III stars, which are made of hydrogen and helium gas are considered to be very massive and therefore short lived. Massive stars usually end up in supernovae which inject the heavier elements produced by the stars into the surrounding medium. These metals open further channels for cooling via addition of a large number of excitable states and making cooling much more effective.

On the other hand, star formation offers self regulating processes that reduce the efficiency of star formation. The supernova explosions and stellar winds inject apart from the metals also a huge amount of energy into the surrounding gas that counteracts cooling and can even accelerate gas to be able to leave to the potential well of the halo, or at least take a long time to be reaccreted (Larson, 1974; Fierlinger et al., 2016). Especially for small halos this has a

severe impact on their stellar mass while for larger halos the potential is deep enough lessen this effect. This first process is usually referred to as stellar feedback.

The second effect, called reionization, which is supposed to be completed at a redshift of $z \geq 6$ (Becker et al., 2001) refers to the ionization of the molecular hydrogen in the Universe in low density regions caused by the ionizing radiation from early stars and early quasars. The intergalactic gas is heated to about 10^4 K during the reionization epoch making it impossible for halos with masses below a few $10^8 M_\odot$ and an associated virial temperature above 10^4 K to even accrete any more gas.

A third phenomenon regulating star formation is feedback due to energy input of Active Galactic Nuclei (AGN). AGN are most likely powered by the accretion of matter onto a super-massive black hole of a mass 10^6 to $10^{10} M_\odot$ in the center of a galaxy (Krawczynski & Treister, 2013). It is not yet fully understood which process distributes the energy in the gaseous halo, but the presence of AGN nuclei can drastically quench star formation (Silk & Mamon, 2012). However, this type of feedback only starts playing a role in galaxies with virial masses above $M_{200} > 10^{12} M_\odot$.

With stellar feedback affecting the low mass end and AGN feedback the high mass end, star formation is most efficient at a halo mass close to a critical mass $M_\star \approx 10^{12} M_\odot$. The relationship between stellar mass and halo mass by Moster et al. (2013) is shown in fig. 3.3.2.2.

3.3.3 Small scale challenges of Λ CDM

Cosmological dark matter only simulation were very successful in predicting the observable structures on scales $> \text{Mpc}$ in an expanding Universe that is dominated by a cosmological constant at late times (see fig. 3.3.3). On scales concerning the low mass end of the galaxy population however the Λ CDM model has often been claimed to have issues reproducing observations. The most relevant challenges are the missing satellites problem (Kauffmann et al., 1993; Klypin et al., 1999; Moore, 1994), the cusp-core tension (Flores & Primack, 1994; Moore, 1994; Oh et al., 2015) and the too-big-to-fail problem (Boylan-Kolchin et al., 2011).

3.3.3.1 The missing satellite problem

The halo mass function of CDM structure formation predicts a increasing number of objects at the low mass end:

$$\frac{dn}{dM} \propto M^{-2} \quad \text{for } M \ll M_\star \quad (3.23)$$

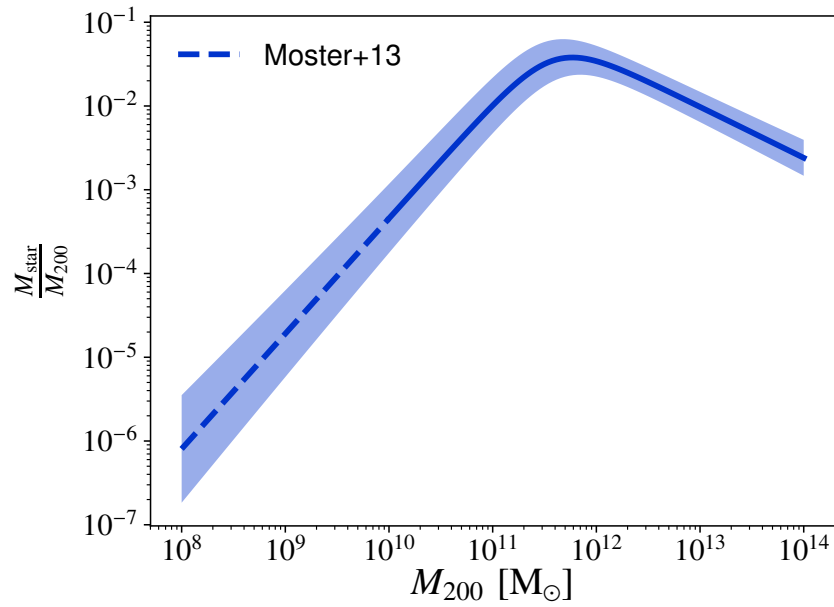


Figure 3.2: Stellar mass-halo mass relation by [Moster et al. \(2013\)](#)

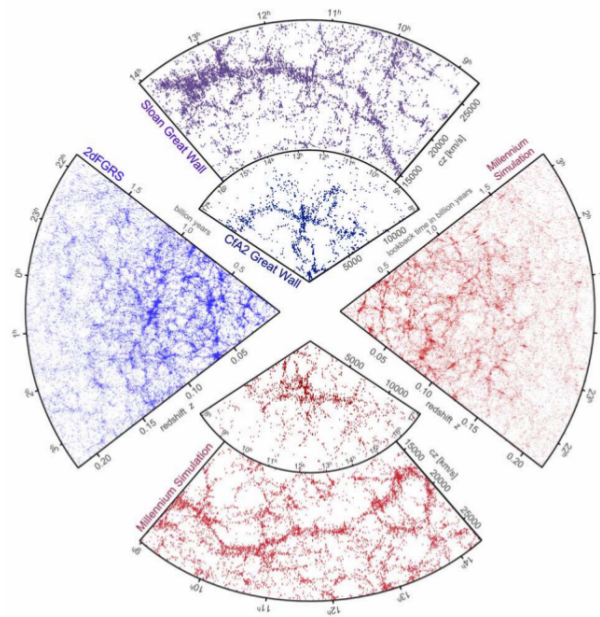


Figure 3.3: Comparison of observations (SDSS, CFA and 2d FGRS) and large scale structure in the Millenium simulation by [Springel et al. \(2006\)](#).

The luminosity function of galaxies however is nearly flat at this mass scale. In fig. 3.3.3.1 from Moore et al. (1999) the cumulative halo mass function for dark matter simulations of a cluster and a Milky Way size galaxy and cumulative galaxy mass function of the Virgo cluster and Milky Way satellites is shown. The mass is expressed in terms of the circular velocity normalized to the host halo circular velocity. As one can see, the dark matter halo counts of the galaxy and cluster size simulation lie just on top of each other, i.e. the dark matter structure formation is scale free. While on the cluster scale the galaxy number counts are also in agreement with the halo number count, on galaxy scale the satellite number counts lie well below the predicted number of dark matter structures. Under the assumption of a one-to-one correspondence between mass and luminosity at all mass scales, this offset in observed satellite number counts leads to the so-called missing satellite problem. In section 3.3.2.2 I have presented reasons for this mass luminosity correspondence to break down at the scale of the smallest galaxies and state-of-the-art cosmological hydrodynamical simulations of Milky Way mass systems including stellar feedback can reproduce observed mass function of Milky Way satellites (Buck et al., 2018). Another limiting factor for the modeling of the correct galaxy luminosity function at low masses investigated by Kim et al. (2017) is the selection due to detection threshold in current surveys.

3.3.3.2 The cusp-core tension

Dark matter only simulations predict a universal density profile for dark matter halos that can be well approximated by an NFW profile (see section 3.3.1.2) (Navarro et al., 1996). The NFW profile has an asymptotic logarithmic slope of $\alpha = -1$ in the center. A slope of the order of $\alpha = -1$ or steeper is associated with a cuspy profile, while profiles with $\alpha = 0$ are called cored. Reconstructions of the inner slope α in nearby galaxies with stellar masses of the order of $10^7 M_{\odot}$ via kinematics (Oh et al., 2015) give values around $\alpha \approx -0.3$ which is clearly favoring a more cored profile than NFW and therefore challenging CDM. Again, using hydrodynamical simulation including stellar feedback Tollet et al. (2016) show that the formation of cores in a certain mass range is possible (see fig. 3.3.3.2). The important parameter is the star formation efficiency M_{star}/M_{200}

3.3.3.3 The too big to fail problem

The too-big-to-fail problem was put forward by Boylan-Kolchin et al. (2011) as they found a large number of sub-halos in their dark matter only simulations that were too massive (big) not to host a galaxy inside them. Their circular

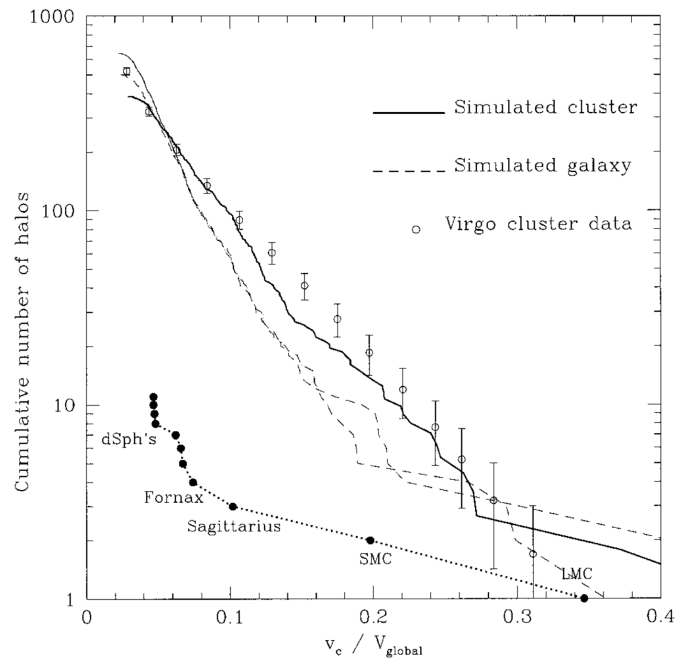


Figure 3.4: Halo mass function for dark matter simulations of a cluster and a Milky Way size halo and galaxy mass function of the Virgo cluster and Milky Way satellites. The mass is expressed in terms of the circular velocity normalized to the host halo circular velocity (Moore et al., 1999).

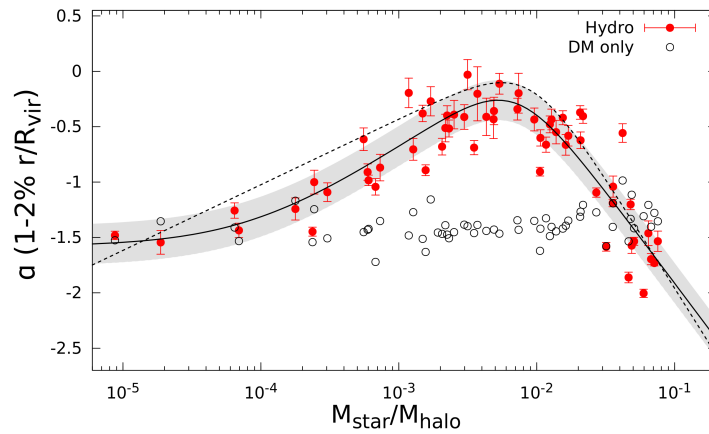


Figure 3.5: The logarithmic inner dark matter density slope α as a function of star formation efficiency, the ratio of stellar and virial mass of the halo (Tollet et al., 2016).

velocity at the radius of an expected galaxies was far higher than observed circular velocities of satellites of the Milky Way. [Boylan-Kolchin et al. \(2011\)](#) claim that Λ CDM predicts too dense sub-halos if baryonic feedback processes are not able to significantly reduce the dark matter density at scales below 1 kpc. It was shown by [Dutton et al. \(2016a\)](#) that baryonic feedback indeed provides one possible solution to the problem as it can reduce the circular velocity at those scales. Further, the reduction of the central density by baryonic effects in combination with enhanced tidal stripping of less concentrated objects seems like a plausible solution.

3.4 Structure formation in WDM

The study of structure formation in warm dark matter is interesting because apart from a cut-off in the linear power spectrum a non-zero velocity dispersion of dark matter will also influence halo and galaxy properties even at scale far above the critical length λ_{dm} . In addition to the baryonic solution to the small scale challenges of Λ CDM the nature of dark matter may also play a role alleviating the deviations of predictions of dark matter only simulations from observations.

3.4.1 Constraints on WDM relic mass by studies of the Lyman-alpha forest

The features of the $\text{H}\alpha$ absorption line in the continuous spectrum of high redshift quasars is called the Lyman- α forest. The spectrum, being gradually redshifted on its way from source to observation, provides a powerful tool to reconstruct the line of sight power spectrum of gas. Using a bias function for the dark matter density, the linear high redshift power spectrum of dark matter can be compared to predictions from WDM simulations and the warm dark matter mass of a thermal relic can be constrained. In recent work by [Iršič et al. \(2017\)](#) in the most general case the dark matter particle mass is constrained to $m_{\text{dm}} > 3.5 \text{ keV}$.

3.4.2 The linear power spectrum in WDM

The presence of streaming velocities (see [2.3.2](#)) in the dark matter component and the associated critical length scale λ_{dm} ([2.13](#)) introduces a natural cut-off in the linear power spectrum at small scales. This cut-off can be described by the function $A(k)$ linking the cold dark matter power spectrum to warm dark

matter one

$$P_{\text{WDM}} = A^2(k) P_{\text{CDM}}(k). \quad (3.24)$$

Through the course of this work I use the following formula by [Bode et al. \(2001\)](#)

$$A^2(k) = [1 + (\alpha k)^{2\nu}]^{-10/\nu} \quad (3.25)$$

where following [Viel et al. \(2005\)](#) I use $\nu = 1.12$ and the parameterization for a thermal dark matter relic with particle mass m_{WDM}

$$\alpha = 0.049 \left(\frac{m_{\text{WDM}}}{1 \text{ keV}}\right)^{-1.11} \left(\frac{\Omega_{\text{DM}}}{0.25}\right)^{0.11} \left(\frac{h}{0.7}\right)^{1.22} h^{-1} \text{Mpc}. \quad (3.26)$$

The power spectra at redshift $z = 99$ for the standard cosmology introduced in section 2.2 for cold dark matter in blue as well as a warm dark matter thermal relic with a particle mass of $m_{\text{WDM}} = 3 \text{ keV}$ in red are shown in fig. 3.4.2. I chose the redshift $z = 99$ because at this redshift I created the initial condition for cosmological simulation from the presented power spectra. As seen in fig. 3.4.2 the warm dark matter particle mass of $m_{\text{WDM}} = 3 \text{ keV}$ is related to a cut-off in the linear power spectrum at $k \approx 20 \text{ Mpc}^{-1}$.

3.4.3 Halo structures in WDM

In a CDM scenario an important contribution to the growth of structure on intermediate scales is the merging of small scale structure. Since the power spectrum of WDM is efficiently damped on scales below λ_{dm} the structure formation of WDM on scales slightly larger than λ_{dm} is efficiently delayed ([Bode et al., 2001](#)) compared to CDM. This has an effect on the halo concentrations c introduced in 3.3.1.2. Halos that form earlier decouple from a higher background density and therefore end up with higher concentrations ([Schneider et al., 2012](#)). The effect of WDM on the concentration - mass relation is shown in fig. 3.4.3 by [Schneider et al. \(2012\)](#).

Thermal velocities further prevent the formation of cusps in the density profile of dark matter halos. However [Macciò et al. \(2012b\)](#) show that for the formation of kpc scale cores in dwarf galaxies a dark matter particles mass of about 0.1 keV is required (see 3.4.3) which however prevents the formation of dwarf galaxy size halos in the first place.

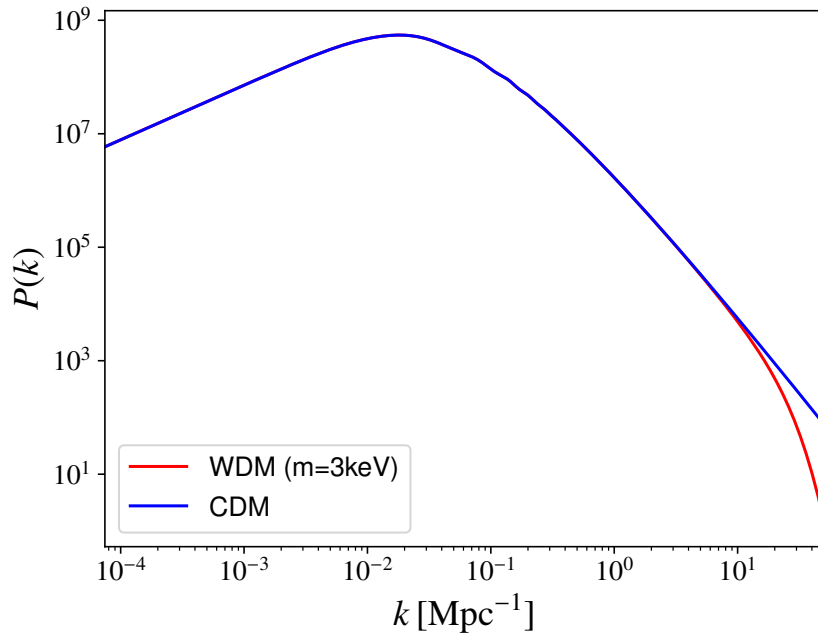


Figure 3.6: Dark matter power spectrum for the Planck 2015 cosmology (Ade et al., 2016) for cold (blue) and warm thermal relic dark matter with a particle mass of 3 keV (red) at redshift $z = 99$.

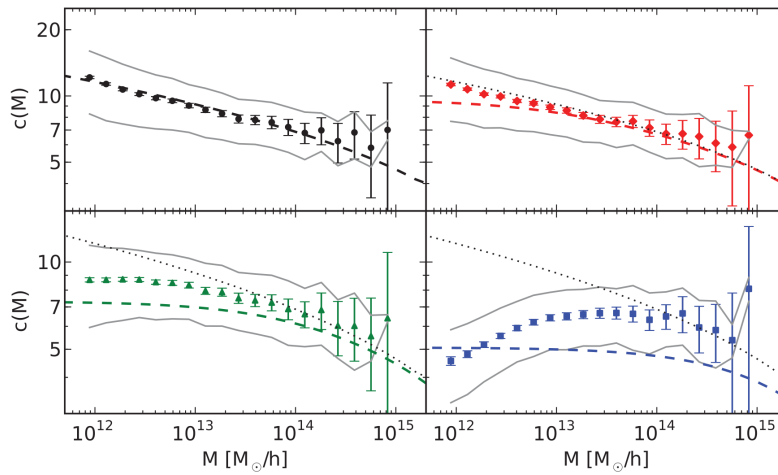


Figure 3.7: Concentration mass relation for CDM (black circles), 1 keV (red diamonds), 0.5 keV (green triangles) and 0.25 keV (blue squares) simulations performed by Schneider et al. (2012).

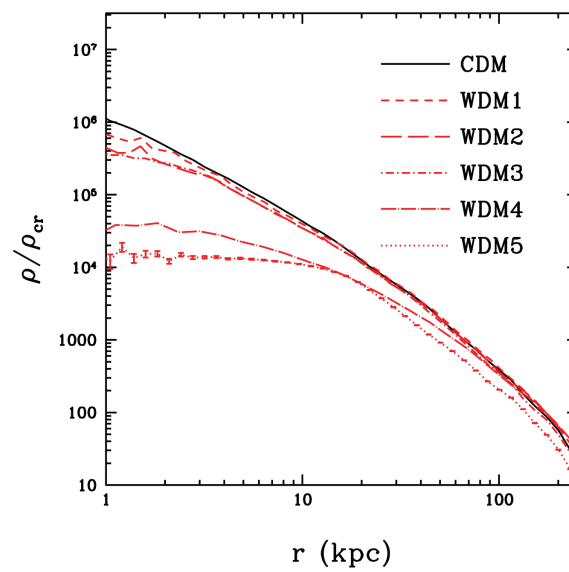


Figure 3.8: Density profiles for CDM (black) and WDM models that are associated with thermal velocities of particles with masses between 0.05 (WDM5) and 2 keV (WDM1).

4 Numerical simulation of structure formation

With the enormous progress in the computational sector over the last decades the possibility of numerical solutions to computationally very intense physical problems became viable. Pure gravity simulations are today replaced by simulations including hydrodynamics, star formation and feedback physics. This can give us new insights in galaxy formation and helps us test the current standard model of structure formation.

4.1 Gravity

The most common approach to solve the equations of structure formation numerically is to discretize the density field to N particles. In this way the partial differential equations transform to the ordinary differential equations for each particle i

$$\begin{aligned}\ddot{\vec{x}}_i &= \vec{\nabla}\Phi(\vec{x}_i) \\ \Phi(\vec{x}_i) &= -G \sum_{j \neq i}^N \frac{m_j}{[(\vec{x}_i - \vec{x}_j)^2 + \varepsilon^2]^{1/2}}\end{aligned}\tag{4.1}$$

where the gravitational softening ε is introduced to avoid unphysical scattering. By further discretizing time, the particle trajectories can be constructed where forces and velocities are updated every time step. However, the evaluation of the forces at all positions is numerically very costly because it scales like $\mathcal{O}(N^2)$ with the particle number.

4.1.1 Tree algorithm

One way to simplify the force evaluation is the tree algorithm ([Appel, 1985](#)). To calculate the force at a given position \vec{x} the surrounding volume is divided into sub-volumes that, as seen from \vec{x} , fit into a cone of opening angle ϑ . The force contribution of each sub-volume is then calculated from its multipole expansion that is usually cut after the quadrupole term. The contributions of all sub-volumes can be saved in a tree structure and reused for the force

calculation at the next position. In this way the numerical cost can be reduced to $\mathcal{O}(N \log N)$. A disadvantage of this method is that errors in the force calculation add up in quadrature and momentum conservation can be violated.

4.1.2 Particle mesh

The particle mesh method suggested by [Bertschinger & Gelb \(1991\)](#) constructs the density field on a regular grid from the particles by assignment the masses to circumjacent grid cells. On a regular grid the equation can be very efficiently solved in Fourier space via fast Fourier transform methods. In the end the particle mesh can also lower the computational cost to $\mathcal{O}(N \log N)$. The disadvantage of the particle mesh is the fixed resolution on a regular grid making even low density regions also contribute to the number of force evaluations and limiting the resolution in the high density regions. Very versions of the particle mesh use an adaptive, moving mesh (see e.g. [Vogelsberger et al. \(2014a\)](#)).

4.2 Smoothed particle Hydrodynamics

To solve the equations of hydrodynamics numerically, one approach, just like for pure gravity, is to discretize the continuum into particles where the state vector $\vec{F} = (\rho, \vec{v}, u)$ is evolved at the particle positions \vec{x}_i . The continuous field can be obtained by convolution of the discrete field with a smoothing kernel $W(\vec{x} - \vec{x}', h(\vec{x}))$

$$F_i(\vec{x}) = \sum_j \frac{m_j}{\rho(\vec{x}_j)} F(\vec{x}_j) W(\vec{x} - \vec{x}_j, h(\vec{x})). \quad (4.2)$$

This approach is called Smoothed Particle Hydrodynamic (SPH). The most common choice for the $W(\vec{x}, h)$ is a cubic spline kernel and the smoothing length $h(\vec{x})$ is defined such that the mass of a fixed number of particles N_{smooth} are enclosed by the sphere with radius $h(\vec{x})$ around \vec{x}

$$\rho(\vec{x})h^3(\vec{x}) = m N_{\text{smooth}} \quad (4.3)$$

The hydrodynamical equations for an inviscid fluid in the Lagrangian frame are given by

$$\begin{aligned}\frac{d\rho}{dt} + \rho \vec{\nabla} \cdot \vec{v} &= 0 \\ \frac{d\vec{v}}{dt} + \frac{\vec{\nabla} p}{\rho} &= 0 \\ \frac{du}{dt} + p \vec{\nabla} \cdot \vec{v} &= 0\end{aligned}\tag{4.4}$$

where I used the advective derivative $\frac{d}{dt} = \frac{\partial}{\partial t} + \vec{v} \cdot \vec{\nabla}$. For the fields evaluated at the particle positions I will use the abbreviation $v(\vec{x}_i) = \vec{v}_i$. The pressure can be replaced with an equation of state

$$p_i = A_i \rho_i^\gamma = (\gamma - 1) \rho_i u_i\tag{4.5}$$

and the adiabatic index γ . The entropic function A_i is supposed to be constant in absence of shocks or thermal diffusion (Springel, 2010). Further following Springel (2010), from the discretized Lagrangian $L_{\text{SPH}} = \sum_i (\frac{m_i}{2} \vec{v}_i^2 - m_i u_i)$ the equations of motions can be obtained by the Euler-Lagrange equations leading to

$$\frac{d\vec{v}_i}{dt} = - \sum_j m_j \left[f_i \frac{p_i}{\rho_i^2} \vec{\nabla}_i W_{ij}(h_i) + f_j \frac{p_j}{\rho_j^2} \vec{\nabla}_i W_{ij}(h_j) \right]\tag{4.6}$$

where $\vec{\nabla}_i$ is the derivative with respect to the coordinates of particle i and

$$f_i = \left[1 + \frac{h_i}{3p_i} \frac{\partial \rho_i}{\partial h_i} \right]^{-1}.\tag{4.7}$$

The continuity and energy equation are inherently fulfilled given the constant mass and entropy of the particles.

Even though the equations of ideal hydrodynamics can describe the formation of shocks they fail to describe the physics of the shocks themselves because at the discontinuity the assumptions of the ideal fluid breaks down. To be able to also describe shocks in the framework of SPH the concept of an artificial viscosity is used to allow dissipation of energy. This introduced additional force terms in the equation of motion and the source terms in the energy equation (for details see Springel (2010)).

Part II

Numerical methods

4.3 Generation of Initial Conditions

The initial conditions for the cosmological box and zoom simulations are created using a modified version of the program GRAFIC2 by [Bertschinger \(2001b\)](#) described in [Penzo et al. \(2014\)](#).

The side length of the box L_{box} together with the number of particles by $N_{\text{side}} = \sqrt[3]{N_{\text{tot}}}$ defines a regular grid on the volume L_{box}^3 . Volume and particle number together with critical density and Ω_m further define the mass resolution $m = \rho_c \Omega_m \left(\frac{L_{\text{box}}}{N_{\text{side}}} \right)^3$. The initial conditions are usually set up at redshift $z = 99$ where the power spectrum on the relevant scales is still linear. Following [Klypin \(2000\)](#) particle positions and momenta are then assigned using the Zel'dovich approximation ([3.2.2](#))

$$\begin{aligned}\vec{x}_{ij} &= \vec{q}_{ij} - \alpha D_+(z) \sum_k \vec{\nabla}_q \Psi(k, \vec{q}_{ij}) \\ \vec{p}_{ij} &= -\alpha a^2 \dot{D}_+(z) \sum_k \vec{\nabla}_q \Psi(k, \vec{q}_{ij})\end{aligned}\quad (4.8)$$

where α is a parameter linked to the normalization of the power spectrum, q_{ij} a the grid point and \vec{x}_{ij} and \vec{p}_{ij} the position and velocity of the particle assigned to the grid point. Further Ψ denotes the velocity potential

$$\Psi(k, \vec{q}) = \sum_k \frac{\sqrt{P(k)}}{k^2} [a_k \cos(k\vec{q}) + b_k \sin(k\vec{q})] \quad (4.9)$$

with the sum over all Fourier modes allowed on the grid \sum_k and the coefficients a_k and b_k being random numbers uniformly distributed between 0 and 1.

The resulting density distribution is then described by the desired matter power spectrum $P(k)$ and the particle velocities initially describe Zel'dovich trajectories.

Regions of interest in dark matter only box simulation, e.g. that include a halo in the desired mass range at later stages, can be traced back to the initial conditions. For the initial conditions of so-called zoom simulations these selected regions are then sampled at a higher resolution and including gas particles besides dark matter.

4.4 SPH and gravity code

The initial conditions are evolved using the SPH tree code GASOLINE ([Wadley et al., 2004](#)) which is an extension of the pure gravity code PKDGRAV

(Stadel, 2001). Besides the hydrodynamics the code includes additional, so-called sub-grid physics like gas cooling, chemical enrichment, star formation and feedback from supernovae (SNe) and massive stars (early stellar feedback) (Stinson et al., 2013). The implemented cooling is described in detail in Shen et al. (2010) and includes photoionization and heating from the Haardt & Madau (2012) ultraviolet (UV) background, Compton cooling, and Hydrogen, Helium and metal line cooling. Star formation is triggered when a certain threshold density $\rho_{\min} = 60m_p$ (with the proton mass m_p) is reached and the temperature is below 15000 K. In this case the high density gas is transformed to stars with a star formation efficiency $c_* = 0.1$. The masses of neighboring gas particles are reduced and turned into a collisionless star particle. One stellar particle represents a stellar population following an initial mass function by Chabrier (2003). The supernova feedback is implemented following the blastwave model described in Stinson et al. (2006) where the cooling for the gas particles that the energy was injected to is delayed.

Part of the simulations were run with an updated version of the code GASOLINE2 (Wadsley et al., 2017; Keller et al., 2014) where the same sub-grid physics as above are implemented. Due to a change in the smoothing kernel size from 32 to 50 particles masses the critical density for star formation is adjusted to $\rho_{\min} = 10.3 m_p$ here.

Part III

Cold dark matter

In this part I want to present the results of the part of my project that focuses on the formation of the smallest galaxies in a Universe that is dominated by a cosmological constant and cold dark matter. It is based on the two papers of the “The edge of galaxy formation” series, [Macciò et al. \(2017\)](#) for the dwarf galaxies and [Frings et al. \(2017\)](#) for the Milky Way satellites. The generation of the cosmological initial conditions and cosmological simulations was carried out by Andrea Macciò. In the chapter on dwarf galaxies the analysis of star formation rates and mass accretion histories was done of by Tobias Buck while I investigated stellar kinematics and halo structure. The initial conditions and simulations for the study of the Milky Way satellites and all associated analysis was entirely done by myself.

5 Introduction

Hydrodynamical simulations of galaxy formation usually divide into cosmological volume simulations (Grand et al., 2017; Schaye et al., 2015; Vogelsberger et al., 2014a; Sawala et al., 2016b) and zoom-in simulations of single objects (Macciò et al., 2012a; Stinson et al., 2013; Aumer et al., 2013; Hopkins et al., 2014; Marinacci et al., 2014; Wang et al., 2015; Dutton et al., 2016a; Wetzel et al., 2016). Nowadays it is possible to achieve resolutions of few million particles per object and with a set of different zoom-in simulations the whole mass spectrum of galaxy formation can be covered (Wang et al., 2015; Chan et al., 2015). On the other hand interacting systems like the Milky Way and its satellite galaxies, that differ by a factor 10^4 in mass, cannot be easily simulated; in fact to achieve a sufficient resolution in the satellite ($\approx 10^6$ particles) one would end up with 10^{10} particles in the Milky Way halo, which is far from manageable even for modern supercomputers. For comparison the simulation with the best mass resolution of a Milky Way system, the Latte project (Wetzel et al., 2016), has total of a few 10^7 particles.

To overcome this issue different approaches have been suggested in the literature. The majority of studies have been made using modeled (pre-cooked) galaxies and then studying their evolution on (several) orbits around their host in isolated simulations (Kazantzidis et al., 2004b; Mayer et al., 2006; Kang & van den Bosch, 2008; D’Onghia et al., 2009; Chang et al., 2013; Kazantzidis et al., 2017). While this may be a good approach to investigate the second part of the evolution of a satellite galaxy, the interaction of the satellite with its host, the use of these modeled galaxies neglects the first part of the life of satellite: its formation and evolution before the accretion onto the host.

However we have decided to use a new approach, which aims to combine the insights from full cosmological hydrodynamical simulations with the very high resolution attainable in simulations of binary galaxy interactions. Namely we use cosmological hydrodynamic simulations to produce realistic initial conditions for the isolated simulation of satellite-host interaction. In the first chapter (chapter 6) I will introduce our cosmological simulations and presented a detailed analysis of the properties of our simulated galaxies *before* the accretion. In the second chapter (chapter 7) I will show the of study the evolution of these galaxies after they have been exposed to the environmental effects of their central object. The final goal is to study the effects of accretion and

environment on realistic satellite galaxies.

6 Dwarf galaxies

6.1 Simulations

6.1.1 Initial Conditions

The simulations presented here are a series of fully cosmological “zoom-in” simulations of galaxy formation run in a flat Λ CDM cosmology with parameters from the 7th year data release from the WMAP satellite (Komatsu et al., 2011): Hubble parameter $H_0 = 70.2 \text{ km s}^{-1} \text{ Mpc}^{-1}$, matter density $\Omega_m = 0.2748$, dark energy density $\Omega_\Lambda = 1 - \Omega_m - \Omega_r = 0.7252$, baryon density $\Omega_b = 0.04572$, power spectrum normalization $\sigma_8 = 0.816$, power spectrum slope $n = 0.968$. The halos simulated for this work have been initially selected from two cosmological boxes of size $L = 10$ and $L = 15 h^{-1} \text{ Mpc}$ and initially run at two different resolutions either with 400^3 or 350^3 dark matter particles.

We chose 27 halos to be re-simulated at much higher resolution using (depending on the mass) a zoom in factor of 8^3 or 12^3 , and with the inclusion of baryons. We use a modified version of the GRAFIC2 package (Bertschinger, 2001b) as described in Penzo et al. (2014) to create the zoom-in initial conditions. Depending on the initial number of particles (400^3 or 350^3), the box size (10 or $15 h^{-1} \text{ Mpc}$) and on the zoom level (8 or 12) we attain slightly different mass resolutions for the different galaxies. In all cases we have about one million elements within the virial radius at $z = 1$. The softening has been chosen to be $\approx 1/70$ of the intra-particle distance (Power et al., 2003) for the dark matter, and it has been rescaled for the gas as the square root of the mass difference in order to ensure a constant force resolution (Moster et al., 2010). For the dark matter it ranges from 47 pc to 21 pc and from 21 to 9.4 pc for the gas. Our choice of softening is just a rescaling of the NIHAO resolution (Wang et al., 2015), which provides a convergence radius well below 1% of the virial radius (see discussion in Tollet et al., 2016). Our high numerical resolution also ensures us that the half mass radius of the galaxy is resolved with at least few hundred mass elements, allowing us to study the response of dark matter to galaxy formation on the scales probed by the observations. Table 6.1 contains all the needed information about the mass and space resolution.

Star particles have an initial mass set to equal to $1/3$ of the gas particle mass, They then return a fraction of their mass to the IGM via stellar winds

Res	m_{dm}	m_{gas}	ϵ_{dm}	ϵ_{gas}
	M_{\odot}	M_{\odot}	pc	pc
1	4.58×10^3	9.14×10^2	47	21
2	2.02×10^3	4.04×10^2	31	14
3	1.36×10^3	2.70×10^2	31	14
4	6.00×10^2	1.19×10^2	21	9

Table 6.1: The four different Mass and spatial resolution levels used in our simulations.

(see Shen et al., 2010, for more details), this implies that even our least (stellar) massive galaxies are resolved with several hundred stellar particles. Table 6.2 contains the detailed information on the properties of each galaxy, the last column refers to the corresponding resolution in table 6.1.

Since we aim to compare our $z = 1$ simulation results with the properties of local galactic satellites one might wonder if selecting halos that are actual satellites at $z = 0$ (but still isolated at $z = 1$) would make a difference w.r.t. using halos that are isolated (centrals) also at $z = 0$.

In order to test this point we have selected our halos to be zoomed from two different environments. Galaxies at resolution 2 and 4 have been selected to be isolated by $z = 0$, meaning they are the "central" object in their halo. Galaxies at resolution 1 and 3, on the contrary, are all "satellites" of a more massive object (at least a factor of 20) by $z = 0$. Despite the very different final environment, the two classes of objects have, at a fixed mass, very similar mass accretion histories (up to $z = 1$) and formation redshifts as shown in figure 6.1. As a consequence the luminous properties of the galaxies at $z = 1$ do not clearly separate in any of the correlations we have studied in this chapter; we have then decided to treat all halos as a single family.

6.1.2 Hydrodynamical code

All halos have been run only to $z = 1$, since after this time we assume that the halos will be accreted onto a more massive object, becoming hence satellites (e.g. Macciò & Fontanot, 2010). The evolution of our halos after accretion is described in chapter 7. Here we will only present the properties of our simulated galaxies at $z = 1$ or earlier times.

The simulations have been performed with the SPH code GASOLINE (Wadsley et al., 2004) as described in section 4.4. The halos in our zoom-in simulations were identified using the MPI+OpenMP hybrid halo finder AHF¹ Knoll-

¹<http://popia.ft.uam.es/AMIGA>

M_{200}	M_{star}	$M_{\text{gas}}^{\text{cold}}$	r_h^{2D}	σ_v	Res
M_{\odot}	M_{\odot}	M_{\odot}	pc	km s^{-1}	
1.13×10^{10}	4.47×10^6	8.62×10^7	337	12.3	3
1.03×10^{10}	8.97×10^6	2.44×10^7	630	15.1	3
6.33×10^9	1.05×10^6	1.73×10^7	148	9.3	1
6.02×10^9	3.74×10^6	1.46×10^7	553	13.1	3
5.72×10^9	1.81×10^6	3.22×10^7	243	8.3	3
5.70×10^9	1.19×10^6	3.08×10^5	219	5.6	2
5.55×10^9	4.53×10^6	1.31×10^6	394	10.6	2
5.01×10^9	4.59×10^4	2.08×10^6	151	6.2	2
4.48×10^9	5.65×10^5	5.48×10^6	301	10.6	3
4.45×10^9	1.27×10^6	1.29×10^7	212	7.6	2
4.09×10^9	7.41×10^5	9.78×10^6	172	8.6	2
3.89×10^9	1.29×10^6	8.05×10^6	260	11.3	2
3.81×10^9	0	0	-	-	2
3.61×10^9	4.01×10^5	5.86×10^6	152	9.45	2
3.51×10^9	4.07×10^5	3.99×10^5	194	7.15	2
3.19×10^9	0	0	-	-	2
3.08×10^9	0	0	-	-	2
2.95×10^9	5.46×10^5	3.33×10^5	172	8.9	3
2.85×10^9	0	0	-	-	3
1.82×10^9	1.45×10^5	2.99×10^3	202	7.23	4
1.70×10^9	1.96×10^5	2.43×10^3	77	3.4	4
1.38×10^9	0	6.1×10^4	-	-	4
1.32×10^9	0	4.81×10^2	-	-	4
1.11×10^9	0	1.18×10^5	-	-	2
1.07×10^9	4.48×10^4	8.91×10^5	138	5.7	3
8.01×10^8	0	0	-	-	4
4.50×10^8	4.25×10^4	4.14×10^5	102	4.8	3

Table 6.2: Parameters of the simulated galaxies: total halo mass (M_{200}), stellar mass (M_{star}), cold ($T < 15000$) gas mass ($M_{\text{gas}}^{\text{cold}}$), 2D half mass radius (r_h^{2D}), l.o.s. stellar velocity dispersion (σ_v). The last column (Res) indicates the resolution of the simulation, see table 6.1 for more details. Galaxies are listed in order of (decreasing) halo mass, dark halos have zero stellar mass.

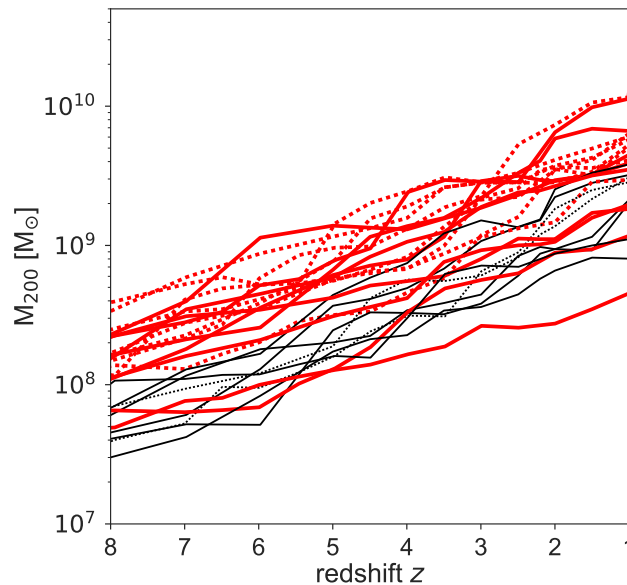


Figure 6.1: The mass accretion history of our simulations. Solid (dotted) lines indicate halos that are "centrals" ("satellites") at $z = 0$. Red is used for luminous satellites, while black represents dark ones.

[mann & Knebe \(2011\)](#). The virial masses of the halos are defined as the mass within a sphere containing $\Delta = 200$ times the cosmic critical matter density. The virial (total) mass is denoted as M_{200} , the virial radius as r_{200} , finally M_{star} indicates the total stellar mass within $0.1r_{200}$.

6.2 Results

In the following we will present the results of our simulated galaxies. In all plots simulations are always shown at $z = 1$, which represents the time at which (on average) these halos will be accreted onto a more massive halo. In most of the plots the simulation results are represented by color dots or lines. The same color corresponds to the same galaxy in all plots, making easier to connect the different properties of the same galaxy across the various figures.

6.2.1 Dark, stellar and gas masses at $z=1$

At first we look into the relation between stellar mass and halo mass for our galaxies. Results are shown in figure 6.2, where colorful circles represent halos that did form stars, while empty red circles show "dark" halos. The grey

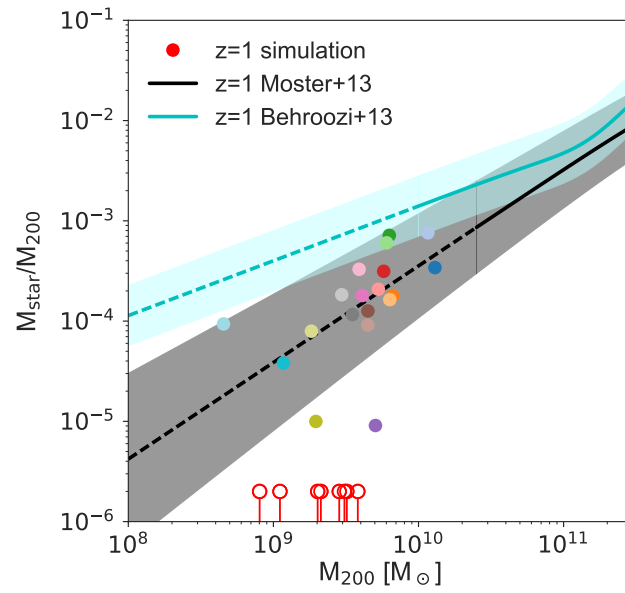


Figure 6.2: The stellar mass halo mass relation for our simulated galaxies at $z = 1$. The colorful points are halos with stars, while the red empty circles represent dark halos. The abundance matching relations from [Moster et al. \(2013\)](#) and [Behroozi et al. \(2013\)](#) are shown in black and cyan respectively, the dashed lines indicate the extrapolation to lower masses.

and cyan lines represent the abundance matching relations from [Moster et al. \(2013\)](#) and [Behroozi et al. \(2013\)](#), respectively. All our galaxies seem to prefer a lower stellar mass than what is predicted by Behroozi and collaborators and being more in agreement with a simple extrapolation of the Moster relation (the extrapolated part is marked by a dashed line in both cases).

An interesting thing to notice is the very large scatter (0.45 dex) in stellar mass at a fixed halo mass: for example for a halo mass around $7 \times 10^9 M_{\odot}$ the ratio between stellar mass and halo mass changes by about two orders of magnitude from 10^{-3} to 10^{-5} . We will return to the origin of this scatter later in section 6.2.4.

For halo masses below $4 \times 10^9 M_{\odot}$ about half of the halos remain dark, in other words they are not able to create a single stellar particle. This is in fairly good agreement with previous results of [Sawala et al. \(2016a\)](#), (see also [Simpson et al. \(2013\)](#)) which use several hydrodynamic cosmological simulations of the Local Group to study the discriminating factors for galaxy formation (i.e. being luminous) in low mass halos. Based on their (larger) sample of halos they also found about half of the halos remaining dark at $z = 1$ at these mass scales. Such a dark fraction is also consistent with what is required to solve the so-called missing satellite problem ([Klypin et al., 1999](#); [Macciò et al., 2010](#); [Sawala et al., 2016a](#)). Despite the large number of dark halos, it is interesting to notice that the lowest mass halo in our sample (cyan point with $M_{200} = 5 \times 10^8 M_{\odot}$) is nevertheless luminous with about $10^4 M_{\odot}$ of stars.

At the mass scales analyzed in this work, we expect galaxies to be quite inefficient in accreting baryons due to the UV background (e.g. [Gnedin, 2000](#); [Hoeft et al., 2006](#); [Okamoto et al., 2008](#); [Simpson et al., 2013](#); [Noh & McQuinn, 2014](#)). In figure 6.3 we show the gas to total mass fraction as a function of stellar mass. All galaxies are strongly baryon “deprived” with respect to the universal baryon fraction (represented by the grey dashed line), with some galaxies able to accrete (and retain) less than 10% of the available baryonic budget, almost regardless of their stellar mass.

On the other hand the very low gas fraction could also be a result of gas outflows due to SNe, given that the mass loading factor of winds increases at lower circular velocities ([Dutton, 2012](#)).

Such question has been raised before, for example [Simpson et al. \(2013\)](#) used a set of AMR (adaptive mesh refinement) cosmological simulations to study the effect of reionization on the gas fraction of halos with masses about $10^9 M_{\odot}$. They found that reionization is primarily responsible for preventing gas accretion in their simulations.

In our case we can use the “dark” halos, i.e. halos that did not form any stars, to also address this question, since obviously they have been affected by the UV background but not by SN explosions. In figure 6.4 we plot the gas

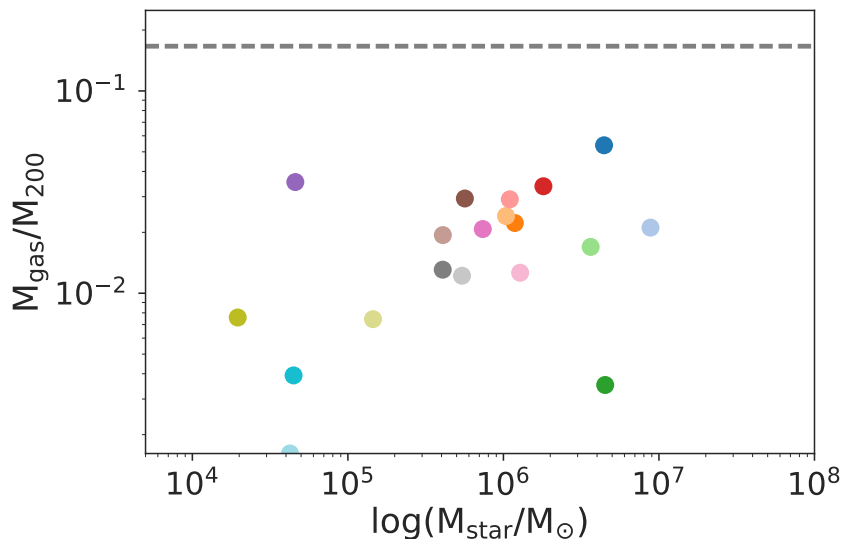


Figure 6.3: The gas to total mass ratio as a function of stellar mass. The grey dashed line represents the cosmic value $\Omega_b/\Omega_m = 0.155$ for the WMAP7 cosmology. The galaxy color coding is the same as in figure 6.2.

fraction as a function of the virial mass of the halo. Dark halos (represented by empty symbols) have similar gas fractions as luminous halos with the same total mass, strongly suggesting that the UV background is the main reason for the lack of baryons at these mass scales in good agreement with previous studies (Simpson et al., 2013; Sawala et al., 2016a)

Our galaxies are quite inefficient in converting their (cold) gas into stars, as shown in figure 6.5, where we plot the cold gas fraction, defined as the mass in gas with $T < 15000$ and hence eligible for star formation, as a function of the total stellar mass. Most galaxies have four to six times more cold gas than stars at $z = 1$. Since today’s Milky Way and M31 satellites are very gas poor, this implies that environmental transformation (e.g. ram pressure stripping) should play an important role in removing gas and completely quenching these galaxies after accretion (see chapter 7).

6.2.2 Galaxy properties and scaling relations

Despite that our simulations are for isolated halos, their aim is to predict the properties of the progenitor (pre-infall) of galactic satellites. It then makes sense to compare their structural parameters (radius, velocity dispersion etc.) at $z = 1$, before infall, with the observations of Milky-Way and Andromeda

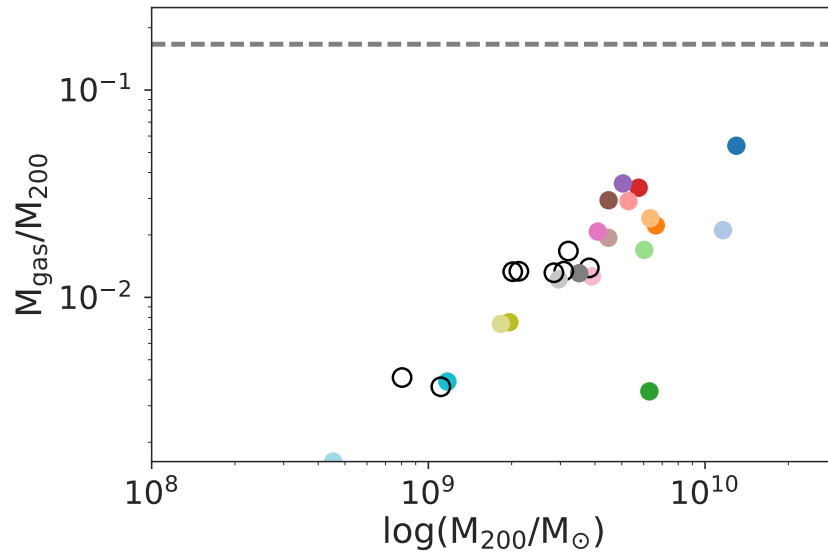


Figure 6.4: The gas to total mass ratio as a function of virial mass. The grey dashed line represents the cosmic value $\Omega_b/\Omega_m = 0.155$ for the WMAP7 cosmology. The galaxy color coding is the same as in figure 6.2, while empty circles represent dark halos (i.e. halos that did not form stars).

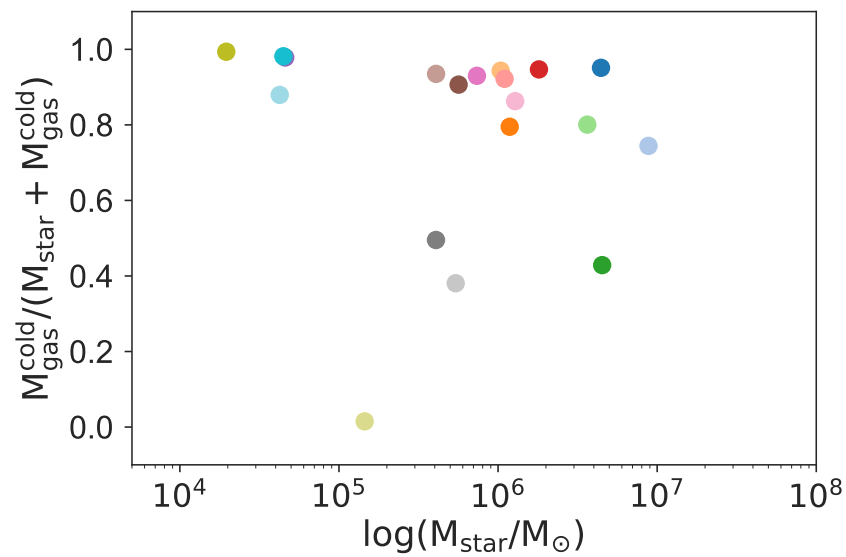


Figure 6.5: The cold gas mass fraction as function of stellar mass. Cold gas is defined as gas with $T < 15000\text{K}$. The galaxy color coding is the same as in figure 6.2.

satellites.

For the observational data we have used a compilation from M. Collins (private communication) which includes results for the Milky-Way and the Andromeda (M31) galaxy satellites including: Walker et al. (2009, MW), Koposov et al. (2011, MW), Tollerud et al. (2012, 2013, M31), Ho et al. (2012, M31), Collins et al. (2013, M31), Collins et al. (2013, M31), Kirby et al. (2013, MW), and Martin et al. (2014, M31).

In figure 6.6 we show the relation between the half (stellar) mass radius and the stellar velocity dispersion. In order to mimic observations, the r_h^{2D} has been computed in two dimensions, meaning that we randomly project each galaxy and then compute the half mass radius using 2D shells; the velocity dispersion is computed along the projection radius of the satellite, equivalent to a line of sight velocity dispersion. We then repeat this procedure ten times for each galaxy and show the average result and its one sigma scatter for every galaxy.

The simulations reproduce quite nicely the trend of the observations especially for isolated halos (blue crosses), but they have a smaller scatter than the one observed in the MW and M31. We will show in chapter 7, that this scatter increases substantially after the satellite is accreted and tidally perturbed.

In figure 6.6 the properties of the galaxies are shown at $z = 1$ which we assume to be the accretion redshift for all satellites. This is clearly a quite strong assumption since both observations and simulations do show a quite large scatter in the satellite accretion redshift (Macciò & Fontanot, 2010; Weisz et al., 2014). In order to test the impact of our *single accretion redshift* approach, in figure 6.7 we show the same quantities as in figure 6.6, but this time we have computed them at a different redshift (chosen random between 1 and 3) for every galaxy. While some points do move, we do not see any particular systematic change in the plot, which makes us confident that we are not introducing any strong bias by performing our study at $z = 1$.

Figure 6.8 shows the relation between stellar mass and metallicity. The simulated galaxies have the same color coding as in figure 6.2 and are compared with observations from Kirby et al. (2011, 2013). Down to a stellar mass of about $10^6 M_\odot$ there is a fairly good agreement between simulations and observations. Between stellar masses of $10^5 M_\odot$ and $10^6 M_\odot$ the simulations start to have lower metallicity compared with observations, and below $10^5 M_\odot$ they have too low metallicities, by more than two dex. We ascribed this difference to the inability of our enrichment algorithms to cope with very rapid and very small star formation bursts. At these very low stellar masses, our galaxies have a very rapid single stellar burst (see figure 6.9) which happens on time scales comparable to our internal time stepping. This means that the time resolution is too short to properly enrich the gas and hence the very low

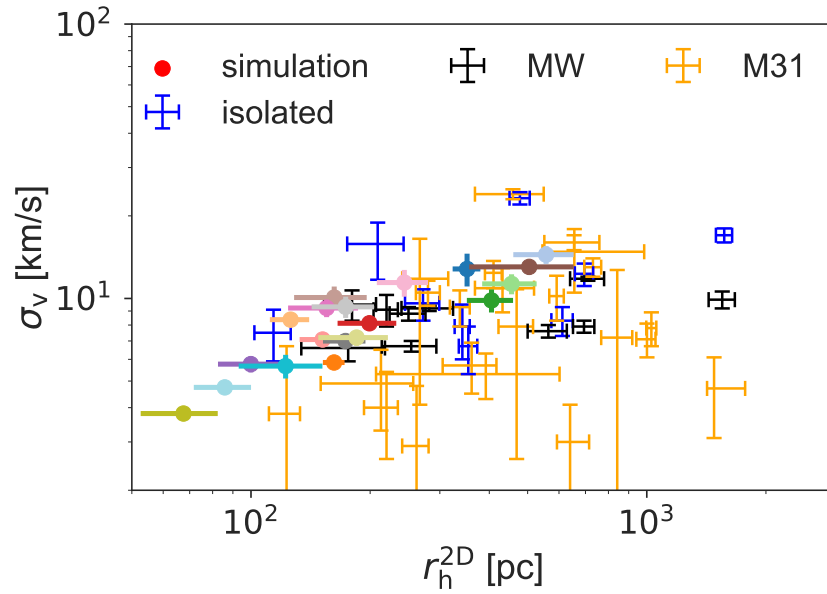


Figure 6.6: The 2D half mass radius vs. the line of sight stellar velocity dispersion. Simulation results are color coded as in figure 6.2, the error bars represent the $1-\sigma$ scatter from ten different projections. Crosses with error bars represent observational data from Collins et al. (2013), see text for more details.

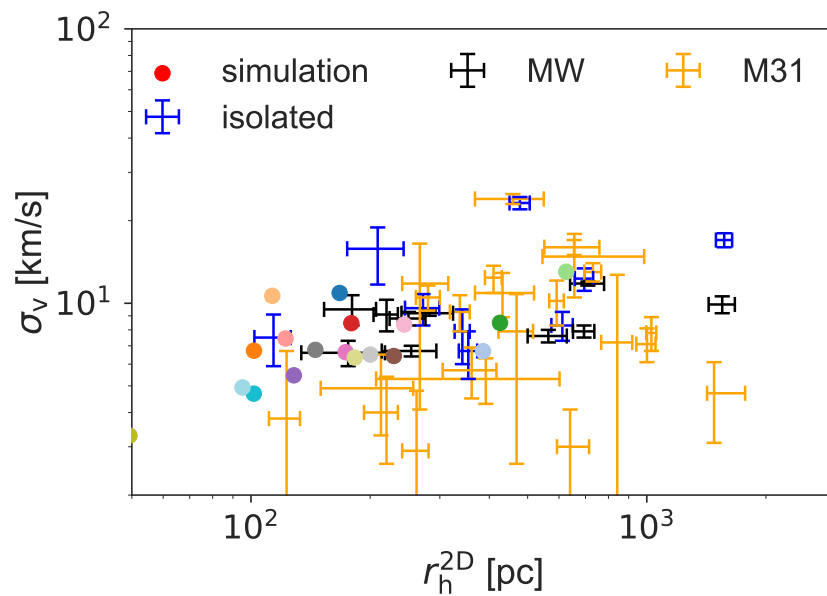


Figure 6.7: Same as figure 6.6 but using a random redshift between 1 and 3 to compute the properties of the galaxies.

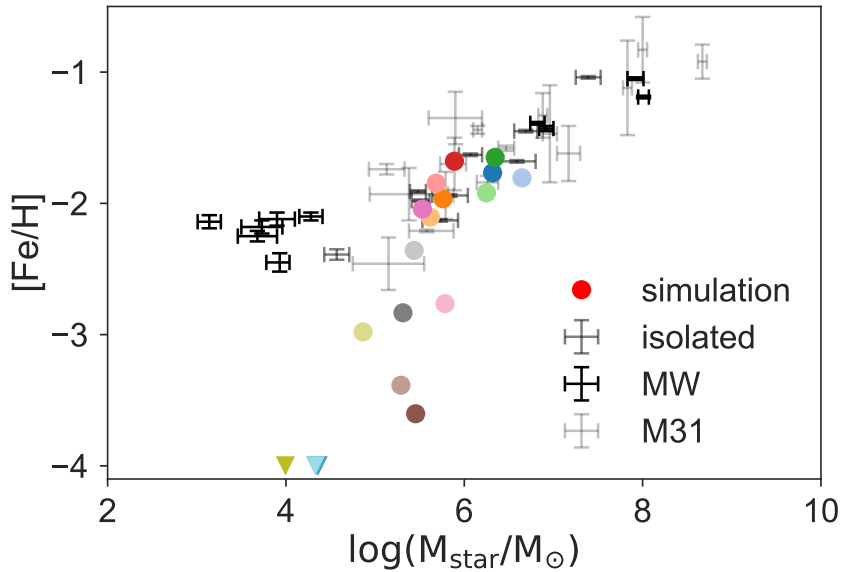


Figure 6.8: Stellar mass - metallicity relation. Observations from Kirby et al. (2011, 2013) are represented by black and grey symbols with error bars. Simulation results are color coded as in figure 6.2; the triangles represent an upper limit to the satellite metallicity.

metallicity. We plan to improve our chemistry network and revisit this issue in a future publication.

The ability of our more luminous galaxies to match the stellar mass metallicity relation suggests that this relation is already in place *before* the infall and that tidal effects will make the galaxies move along the relation, see chapter 7 for more details.

6.2.3 Star formation rate and halo response

As already mentioned above the star formation rate at the edge of galaxy formation is quite stochastic and made of rapid bursts, followed by long quiescent periods, as shown in figure 6.9, where the star formation is computed over a period of 100 Myrs. In this figure galaxies are ordered by halo mass (according to table 6.2) but retain the same coloring scheme as in figure 6.2.

Galaxies with similar halo mass (i.e. in neighboring panels in figure 6.9) show quite diverse star formation histories, with different times and intensities for the stellar bursts. This is in quite good agreement with the diversity in the stellar mass assembly of satellites in the Milky Way and M31, as observed by Weisz et al. (2014). In figure 6.10 we directly compare the cumulative stellar

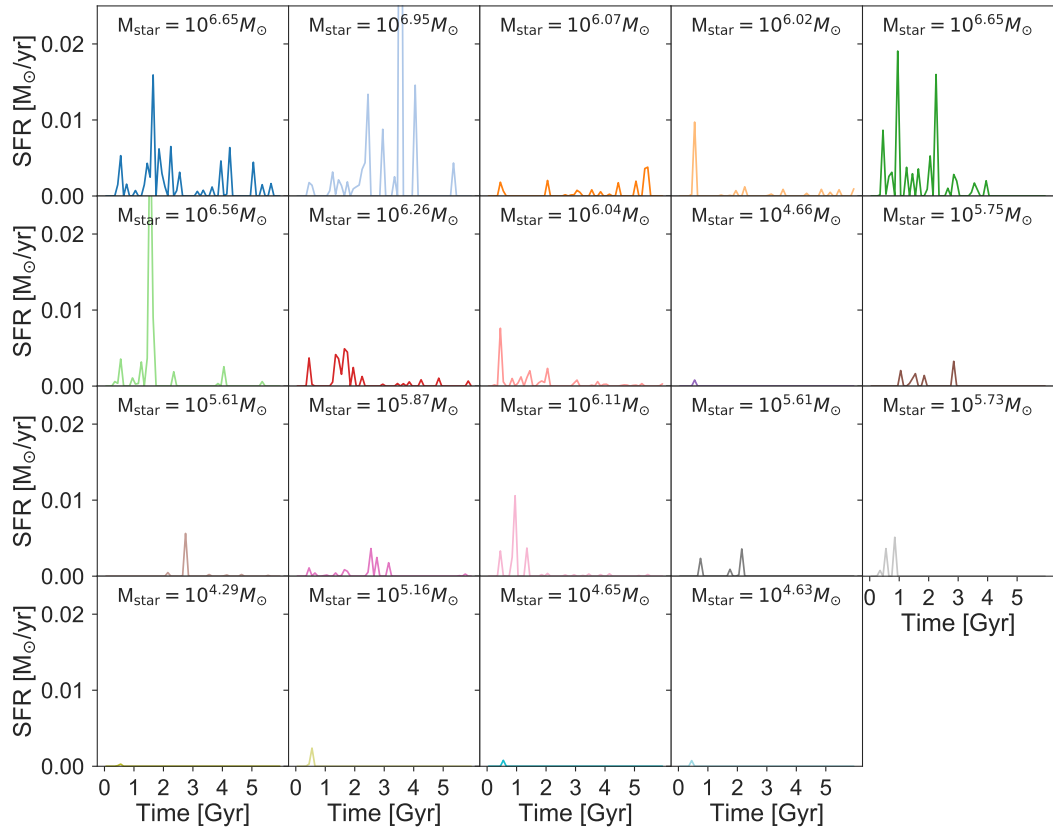


Figure 6.9: Galaxy star formation histories computed over a period of 100 Myrs. The galaxies are ordered with decreasing total mass (as in table 6.2). The values of the stellar masses are reported in each single box. The color coding is the same as in figure 6.2.

mass growth of our simulated galaxies (color coded according to their stellar mass) with the results of Weisz and collaborators up to $z = 1$. As already noted in previous simulations (Governato et al., 2015; Fitts et al., 2017; Wetzel et al., 2016) we are also able to nicely reproduce the diversity of the observed dwarf galaxies star formation histories.

Several recent papers have pointed out a correlation between repeated gas outflows due to star formation bursts and the expansion of the inner dark matter distribution (Pontzen & Governato, 2012; Macciò et al., 2012b; Di Cintio et al., 2014; Madau et al., 2014; Chan et al., 2015; Dutton et al., 2016b; Read et al., 2016; Tollet et al., 2016). It is then interesting to look at the inner slope of the dark matter density profile in the hydro simulations and to compare this to their Dark Matter Only (DMO) counterparts. In figure 6.11 we show

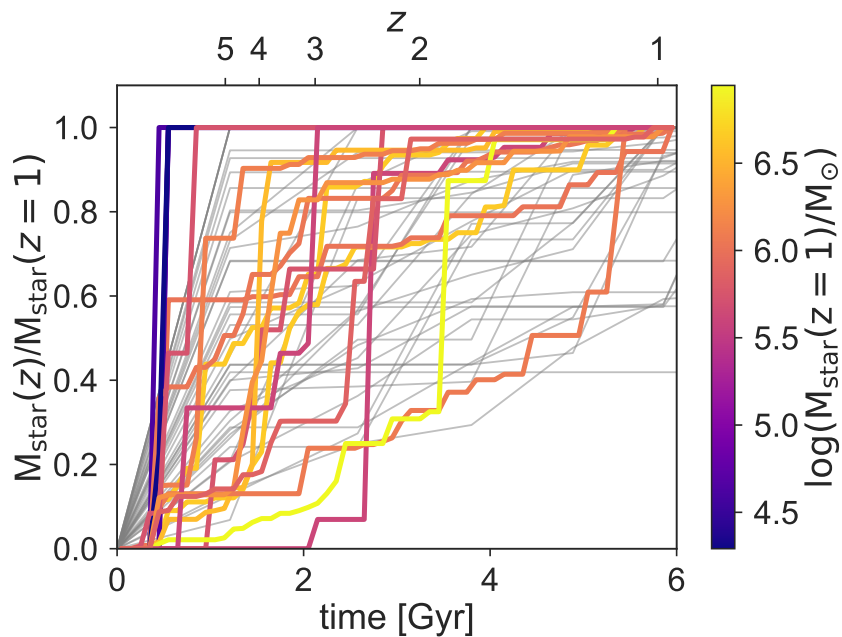


Figure 6.10: Cumulative stellar mass growth up to $z = 1$. Simulations are color coded according to their final stellar mass (right side bar). Observations from Weisz et al. (2014) are also limited to $z = 1$ and are shown in grey.

the logarithmic slope of the dark matter density profile ($\alpha = d \log(\rho) / d \log r$) computed between 1 and 2% of the virial radius, versus the stellar mass to halo mass ratio. We chose the latter quantity since it has been shown to be the most correlated with α (Di Cintio et al., 2014). Results from hydro simulations are represented by the usual color symbols while the corresponding DMO (i.e. Nbody) results are shown as black squares; in both cases the error bars represent the uncertainty from the fitting routine. In the same plot we show the fitting formula from Tollet et al. (2016), which was based on the analysis of 90 galaxies from the NIHAO suite (Wang et al., 2015).

There is a quite good agreement with the results from Tollet et al. (2016), (see also Chan et al., 2015), meaning that we see a partial halo expansion for a star formation efficiency (M_{star}/M_{200}) close to 10^{-3} (the first two points on the right), but then for lower star formation efficiency our galaxies retain the same dark matter density profiles as their pure N-body counterparts. Baryons are able to alter dark matter profiles possibly only in very massive satellites, while smaller objects are supposed to retain the typical CDM cuspy Einasto-like profiles (Dutton & Macciò, 2014) as already pointed out in several previous

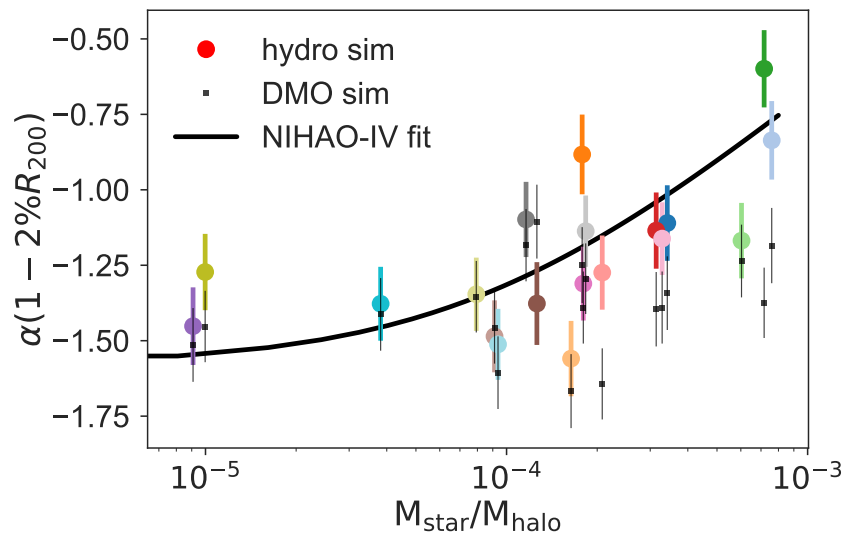


Figure 6.11: Logarithmic slope of the dark matter halo profiles in the hydro simulation (color symbols) and in the dark matter only simulation (black dots). The solid line shows the fitting formula proposed in the NIHAO-IV paper (Tollet et al. 2016). The slope α is computed between 1 and 2% of the virial radius, while the error bars represent the uncertainty from the fitting routine.

studies like (e.g. Governato et al., 2012; Oñorbe et al., 2015, and references therein)

In figure 6.12 following Governato et al. (2012) we also show the same slope α as a function of stellar mass to facilitate a possible comparison with observations, symbols have the same meaning as in figure 6.11.

Our choice of measuring the profile slope between 1 and 2% of the virial radius is somehow arbitrary; for this reason we also compute it at a more natural length scale as the 2D half mass radius (r_h^{2D} , for this measurement we used five equally spaced logarithmic bins around the radius.). Figure 6.13 shows the behavior of this new measurement of alpha as a function of the galaxy stellar mass. By comparing the slope for the Dark Matter Only (DMO) simulations with the one of the Hydro ones, also in this case there seems to be a particular stellar mass (around $M_{\text{star}} \approx 10^6 M_{\odot}$) above which the dark matter profiles becomes flatter in the hydro simulations. It is also interesting to note that for very low stellar masses, the hydro simulations are slightly contracted w.r.t. N-body ones on the scale of r_h^{2D} .

Recently Read et al. (2016) presented very high resolution simulations of isolated dwarf galaxies reporting that if star formation proceeds for long enough,

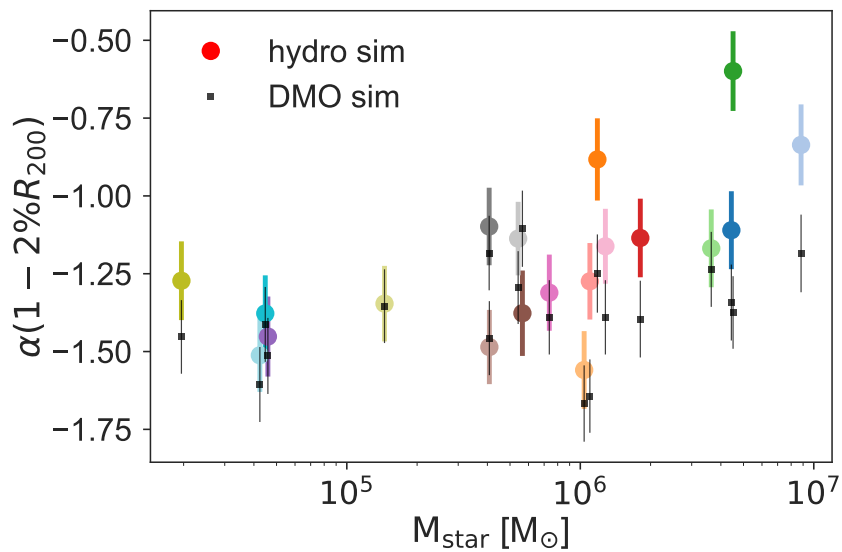


Figure 6.12: Logarithmic slope of the dark matter halo profiles in the hydro simulation (color symbols) and in the dark matter only simulation (black dots) as a function of galaxy stellar mass. The slope α is computed between 1 and 2% of the virial radius.

dark cores of size comparable to r_h^{2D} always form. The key factor is to have an extended star formation period, of about 4 Gyr for a $10^8 M_\odot$ halo and 14 Gyr for $10^9 M_\odot$ one. Our galaxies from one side seem to support Read et al. findings in a sense that galaxies with "continuous" star formation do seem to have flat profiles at the half mass radius, as can be seen by looking at the galaxies in the first row of figure 6.9 and their respective position in figure 6.13. On the other hand none of our low (stellar) mass galaxies has a cored profile, not even at the half mass radius. This could be an indication that in a more realistic, cosmological set up (which also includes the UV background, an ingredient missing in Read et al.) all star formation histories are indeed truncated after the first bursts and no cores should be expected in low mass galaxies.

A corollary of our simulation results is that, under the assumption that environmental process do not strongly modify the dark matter distribution (see chapter 7), a firm detection of a large core in any of the Milky Way satellites with a stellar mass below few $10^6 M_\odot$ will call for a revision of the simple Cold Dark Matter model . It will possibly point towards a different nature for dark matter, either warm (but see Macciò et al., 2012a), or self interacting (Vogelsberger et al., 2014b; Elbert et al., 2015) or even more exotic

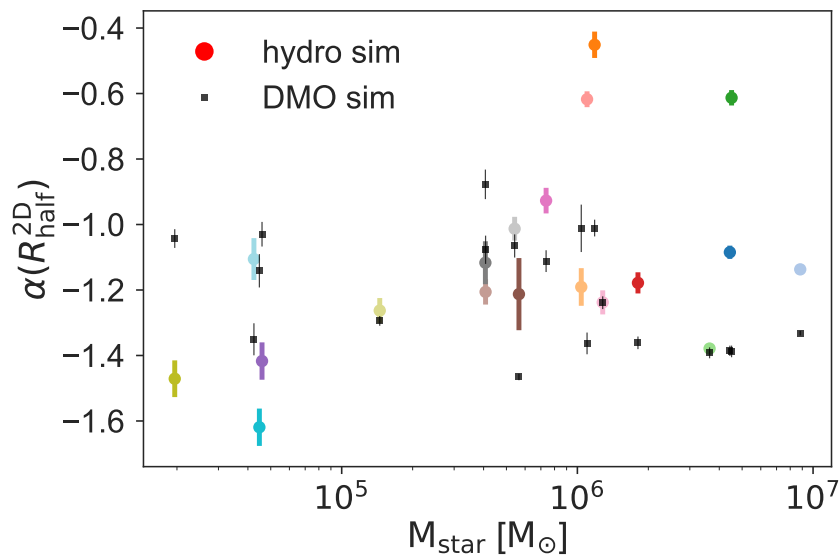


Figure 6.13: Logarithmic slope of the dark matter halo profiles at the scale of the half mass radius. Color symbols represent the hydro simulation (same scheme as previous plots), the black squares the dark matter only runs.

models (e.g. [Macciò et al., 2015](#)).

6.2.4 Diversity of star formation histories and the DM assembly

In this section we want to better understand the origin of the diversity in star formation histories shown in figure 6.9. To this extent, we will focus our attention on just four halos that have very similar dark matter masses, all around $10^{9.75}M_{\odot}$, but have considerably different stellar masses at $z = 1$ from 4.5×10^4 to $3.63 \times 10^6M_{\odot}$.

In figure 6.14 we show the star formation histories of these four galaxies (upper panels) compared to their inner mass accretion (middle panels) defined as the mass within a sphere of 2 kpc from the center of the galaxy.

There is a clear correlation between the infall of new mass (gas and dark matter) and the onset of star formation. This is particularly evident in the case of sudden jumps in the enclosed mass, as for example at $t \approx 1$ Gyr for the second (green) and the third (red) object. These are clearly major merger events that are able to double the mass in practically less than 100 Myrs, as we have also confirmed by visual inspection. Corresponding to these mergers

there is a quick rise in star formation, which in the case of the “red” galaxy is even followed by an extended (≈ 2 Gyr) period of activity.

On the contrary, the fourth galaxy (purple) has an extremely quiet mass accretion history, characterized by continuous smooth accretion and no mergers. In this case the star formation is limited to a single early burst which led to a very low stellar mass at $z = 1$.

The increase in SFR is due to two effects: the merging halo brings in new gas for star formation but it also compresses (due to shocks) the gas inside the main halo, increasing its density and hence reducing the cooling time.

In order to disentangle these two effects, for every newly formed star (during the SF peak) we traced back the origin of its parent gas particle and checked if it was outside the virial radius at the previous snapshot (about 500 Myrs ago), meaning that that gas particle came in inside the merging halo. The results are shown in the lowest panels of figure 6.14. For the two galaxies that undergone a merger, about half of the newly formed stars were generated from "ex-situ" gas particles. This results, even though based only on two galaxies, seem to imply that there is an equal contribution of new and old gas to star formation.

Overall our analysis suggest that the large scatter in the stellar mass halo mass relation we find at the “edge” of galaxy formation is due to the strong impact that mergers have in triggering star formation and to their intrinsically stochastic nature.

6.2.5 Dark halos

As shown in figure 6.2, almost half of the halos with a mass below $5 \times 10^9 M_{\odot}$ did not manage to form any stars, and remained dark. This is due to the effect of the ultraviolet (UV) background parameterized following Haardt & Madau (2001). This background takes into account the ionization field produced by quasars and stars and quenches star formation in small galaxies by photo-heating their gas, which gets too hot to be confined in their shallow potential wells (Bullock et al., 2000; Somerville, 2002; Okamoto et al., 2008). The extent to which this field is able to affect star formation depends on the halo mass, and it is usually described by the so called characteristic mass (M_c) which is defined as the mass at which halos on average have lost half of their baryons (e.g. Simpson et al., 2013)

In figure 6.15 following Fitts et al. (2017), we show the mass accretion history of nine halos, four dark (black lines) and five luminous (colored lines), that have similar masses at $z = 1$, together with the redshift evolution of the characteristic mass as computed by Okamoto et al. (2008, dashed grey line). Luminous halos have a more rapid accretion history which brings their virial

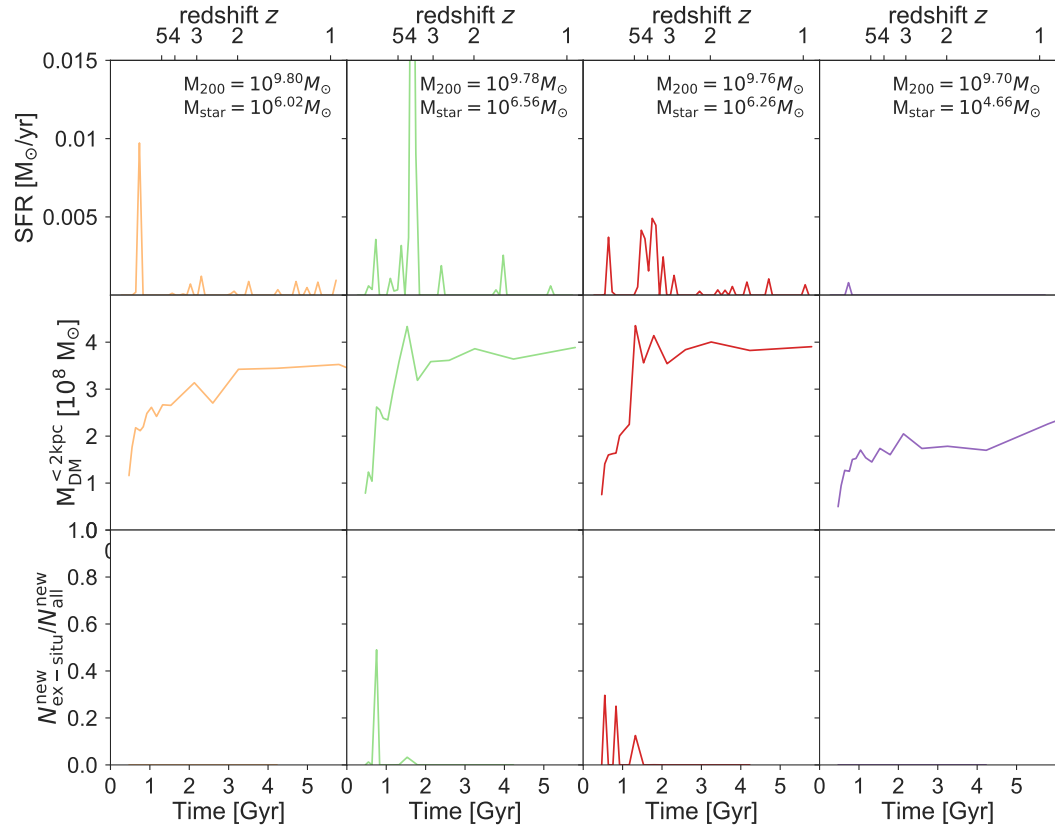


Figure 6.14: The star formation rate (upper panels), the mass accretion history (middle panels) and the fraction of stars form from in-situ vs. ex-situ gas particles (lower panels). The results are shown for four galaxies with similar halo mass at $z = 1$, but very different stellar mass. There is a clear correlation between mergers, i.e. sudden jump in the mass accretion history, and strong star formation episodes.

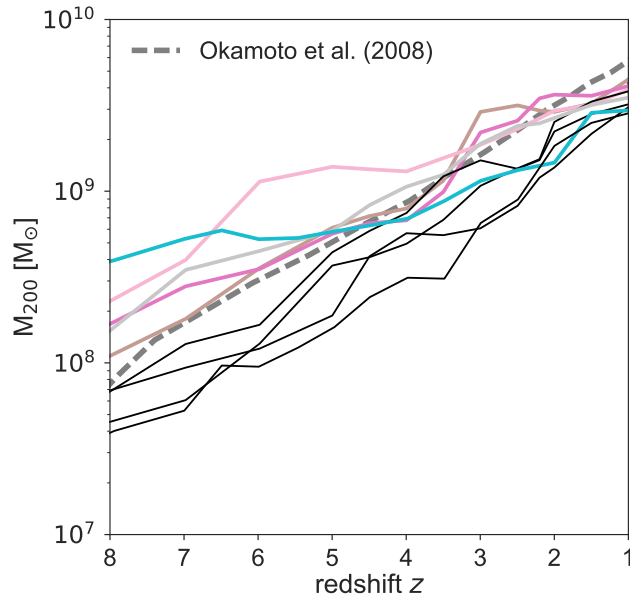


Figure 6.15: Mass accretion history of luminous and dark halos with similar $z = 1$ masses. The grey dash line shows the characteristic mass M_c (mass at which halos on average have lost half of their baryons) as computed by Okamoto et al. 2008.

masses above M_c at high redshift, allowing then gas to successfully cool in the center of the halo. The three dark halos, despite achieving the same final ($z = 1$) mass as the luminous ones, are characterized by a slow mass accretion at high redshift (Benítez-Llambay et al., 2017). This sets them below the critical mass at any redshift, and hence their gas cooling is strongly suppressed in agreement with previous works (Sawala et al., 2016b; Fitts et al., 2017, and references therein)

7 Milky Way satellites

7.1 Simulations

We use a subsample of seven simulations of the dwarf galaxy sample introduced in chapter 6 to study the effect of accretion onto a Milky Way size halo. The original sample contains 27 cosmological zoom-in simulations of central halos in the mass range of $5 \times 10^8 < M_{\text{dark}}/M_{\odot} < 2 \times 10^{10}$ of which 19 form a galaxy in their center. The simulations were run using the smoothed particle hydrodynamics code GASOLINE (Wadsley et al., 2004) as described in section 4.4. The mass resolution of the zoom-in region of the simulations is shown in Table 7.1. Gas particles have an initial mass of $m_{\text{gas,init}} = f_{\text{bar}} \cdot m_{\text{DM}}$ while stellar particles start with initial masses $m_{\text{star,init}} = \frac{1}{3}m_{\text{gas,init}}$, where $f_{\text{bar}} = \frac{\Omega_{\text{b}}}{\Omega_{\text{dark}}}$ is the cosmic baryon fraction.

7.1.1 Satellite initial conditions

Starting from the redshift $z = 1$ snapshots of the cosmological simulations described in chapter 6 we cut out seven halos and their surrounding structures up to a distance of four virial radii from their center (for the virial radius we used the region enclosing a density equal to 200 times ρ_{crit} , where ρ_{crit} is the cosmic critical matter density). These cut out regions were then transformed from cosmological (i.e. expanding) coordinates to physical ones and used as initial conditions for our subsequent accretion simulations. Table 7.1 contains the main parameters of our selected halos, the name *sat* is used for halos that contained stars at the starting redshift ($z = 1$) while we reserve the name *dark* for halos without stars. As a first step we run all the halos (dark and luminous) “in isolation” from $z = 1$ to $z = 0$, meaning we evolved them without the presence of the central halo, in order to have a base line for the evolution of our galaxies; we will refer to this set of simulations as the *isolated* runs.

7.1.2 Central object parametrization

We used two different models for the parametrization of the central object. At first we described it as an analytical potential consisting of the superposition of two distinct potentials for the dark matter and the stellar disk. For the dark

Table 7.1: Virial dark matter mass, stellar mass, virial radius (defined by an overdensity of $200 \rho_{\text{crit}}$) and dark matter particle mass of the selected subsample of simulations. For all simulations the gravitational softening for the dark matter, stellar and gas particles is $\varepsilon_{\text{DM}} = 31 \text{ pc}$ and $\varepsilon_{\text{gas}} = \varepsilon_{\text{star}} = 14 \text{ pc}$, respectively.

Name	$M_{\text{DM}}[M_{\odot}]$	$M_{\text{star}}[M_{\odot}]$	$r_{200}[\text{kpc}]$	N_{star}	$m_{\text{DM}}[M_{\odot}]$
satI	1.02e+10	8.97e+06	31.34	81629	1.36e+03
satII	5.52e+09	1.81e+06	25.65	16822	1.36e+03
satIII	5.61e+09	1.20e+06	25.60	6902	2.02e+03
satIV	2.92e+09	5.46e+05	20.65	5202	1.36e+03
satV	4.49e+08	4.25e+04	10.97	408	1.36e+03
darkI	3.04e+09	0	20.93	0	2.02e+03
darkII	2.81e+09	0	20.32	0	1.36e+03

matter halo we used a Navarro-Frenk-White (NFW) potential (Navarro et al., 1996) with a mass $M_{200} = 1 \times 10^{12} M_{\odot}$, a concentration parameter $c = 10$ (Dutton & Macciò, 2014), and a virial radius $r_{200} = 210 \text{ kpc}$. For the stellar body we used a Miyamoto & Nagai potential (Miyamoto & Nagai, 1975) with a disk mass $M_{\text{disk}} = 5 \times 10^{10} M_{\odot}$, disk scale length $R_{\text{disk}} = 3.0 \text{ kpc}$ and height $h_{\text{disk}} = 0.3 \text{ kpc}$. The disk is aligned with the $x - y$ plane of the simulation.

The use of an analytic potential makes the simulation faster but misses one possible important ingredient: dynamical friction. In order to estimate its effect we also used a live halo (i.e. made with particles) without a disk component.

To construct the (central) galaxy model we apply the method described in Springel et al. (2005) and in Moster et al. (2014). The halo is described by a NFW density profile with the same parameters used for our analytic potential (a virial radius of $r_{200} = 210 \text{ kpc}$, a virial mass of $M_{200} \approx 1 \times 10^{12} M_{\odot}$ and a concentration parameter of $c = 10$). We used two resolution levels for this live halo with 10^5 and 10^7 particles, respectively. Runs performed with the live halo are discussed in the next section.

7.1.3 Orbits

We select six different orbits and run the simulations until redshift $z = 0$.

All orbits start at the virial radius at the coordinates $(x, y, z) = (210.0, 0, 0) \text{ kpc}$ but they differ in the initial velocity of the satellite and in the angle between the plane of the orbit and the stellar disk of the host halo. The parameters of all orbits are summarized in table 7.2, where we have ordered the six orbits by

their “disruptiveness”, i.e. *orbitI* is the most gentle orbit, causing the least deviations from the isolated run (for example in mass loss) while *orbitV* provides the most violent interaction between the satellite and the central object, with the exception of the complete radial infall. The pericenter distance is shown only for *satV*. We want to point out that compared to the orbits of surviving Milky Way satellites even *orbitI* with a pericenter of 25 kpc is quite extreme. [Garrison-Kimmel et al. \(2017\)](#) show that in their simulations only 5% of the surviving satellites around Milky Way mass galaxies have orbital pericenters below 20 kpc. The choice for such strong orbits has been dictated by our aim to bracket the possible scenarios between unperturbed evolution (the isolation case) and strong interactions.

In [Fig. 7.1](#) we show the trajectory of *satV* on the orbits from *I* to *V* from $z = 1$ to $z = 0$ (5.7 Gyr). The colors correspond to individual orbits as introduced in [Table 7.2](#). The center of each satellite is defined as the position of the maximum of the stellar (dark matter) density distribution for the luminous (dark) satellites. The position of this maximum is derived via a shrinking spheres algorithm according to [Power et al. \(2003\)](#).

In [Fig. 7.2](#) we compare the orbit evolution of *orbitIII* in the analytic potential in the live halo at two different resolutions levels: 10^5 and 10^7 particles. Dynamical friction does slightly modify the orbit, but the effect is quite small and independent of the resolution of the live halo, the same result holds also for the other orbits. Since our choice of orbits has been practically random it is fair to say that the small effect of dynamical friction is very similar to a slightly different choice of orbits, and can be then neglected in our study.

7.1.4 Ram pressure

Even with a live halo our set up is not able to take into account the effect of ram pressure between the (hot) gas in the host halo and the gas in the satellite. We therefore add an analytic recipe for ram pressure to our simulations. At every basic time-step (1 Myr), we remove all gas particles within the satellite that are below a certain threshold density ρ_{th} .

This density threshold evolves with time according to the following expression:

$$\rho_{\text{th}}(t) = \begin{cases} \rho_{\text{max}} \left[\frac{\rho_{\text{min}}}{\rho_{\text{max}}} \right]^{(1 - \frac{t}{\tau_{\text{ram}}})^a}, & \text{for } t < \tau \\ \rho_{\text{max}}, & \text{for } t > \tau \end{cases} \quad (7.1)$$

where ρ_{min} is the gas density at four virial radii; ρ_{max} is the gas density in the center of the halo; τ_{ram} is the gas removal time scale (see later for more details); a is a free parameter and t denotes the runtime of the simulation.

Table 7.2: Compilation of the different orbit scenarios with their initial velocity, pericenter distance and orbit inclination with respect to the host galaxy disk. All orbits initiate at the coordinates $x = 210$ kpc, $y = z = 0$. The color indicates the color coding in Fig. 7.1.

Name	(v_x, v_y, v_z) [v_{200}]	τ_{ram} [Gyr]	r_{min} [kpc]	ϑ [deg]
<i>orbitI</i>	(−0.45, 0.3, 0)	1.5	25.52	0
<i>orbitII</i>	(−0.45, 0, 0.3)	1.5	25.46	90
<i>orbitIII</i>	(−0.2, 0.2, 0.2)	1.5	25.26	45
<i>orbitIV</i>	(−0.5, 0, 0.1)	1.4	7.94	90
<i>orbitV</i>	(−0.5, 0.1, 0)	1.4	7.2	0
<i>radial</i>	(−0.5, 0, 0)	1.3	-	0

If in equation (7.1) we set $\rho_{\text{th}}(t = 0) = \rho_{\text{min}}$ and $\rho_{\text{th}}(t = \tau_{\text{ram}}) = \rho_{\text{max}}$, this implies that all gas will be removed (outside in) at time $t = \tau_{\text{ram}}$. We fixed the value of the parameter a at 0.2, since this ensures that ρ_{th} follows the radial profile of the gas density. Finally we set the gas removal time scale τ_{ram} approximately equal to a half the dynamical time scale of the orbit, so that all gas is removed after one pericenter passage (see Table 7.2).

We do not expect ram pressure to be important from a dynamical point of view, since our galaxies are very strongly dark matter dominated (see chapter 6), but it might be important to accelerate the galaxy quenching. On the other hand by comparing *satIV* on *orbitII* with and without ram pressure we found no strong changes in its star formation rate, with both set ups showing a very similar quenching behaviour compared to the isolated run.

Even if we do not see a large difference in the outcomes of the simulations with and without the ram pressure model, we still apply the ram pressure model to all simulations since it decreases the computational cost (by reducing the number of gas particles within the galaxy).

7.2 Results

7.2.1 Rotational support

One main difference between our approach and previous studies in the literature is the use of cosmological simulations as initial conditions, it is then interesting to check the dynamical state of our galaxies before the infall. In Fig. 7.3 we show the amount of rotational support of the stellar component in the dwarf galaxies at $z = 1$. We obtain the rotational velocity v_φ by averaging the individual velocities of the stellar particles in \vec{e}_φ direction. The unit vector

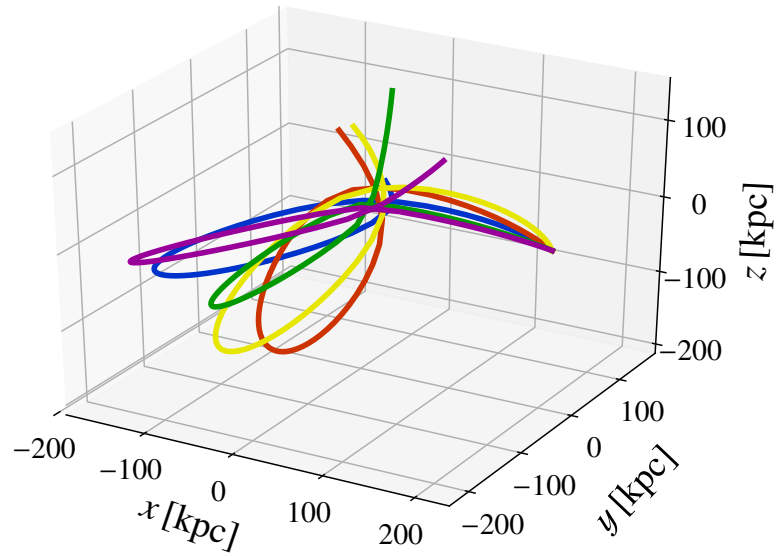


Figure 7.1: Visualization of the orbits (*orbit I* to *orbit V*) presented in Table 7.2 from infall to 5.7 Gyr after infall. The color coding is the same as in Table 7.2.

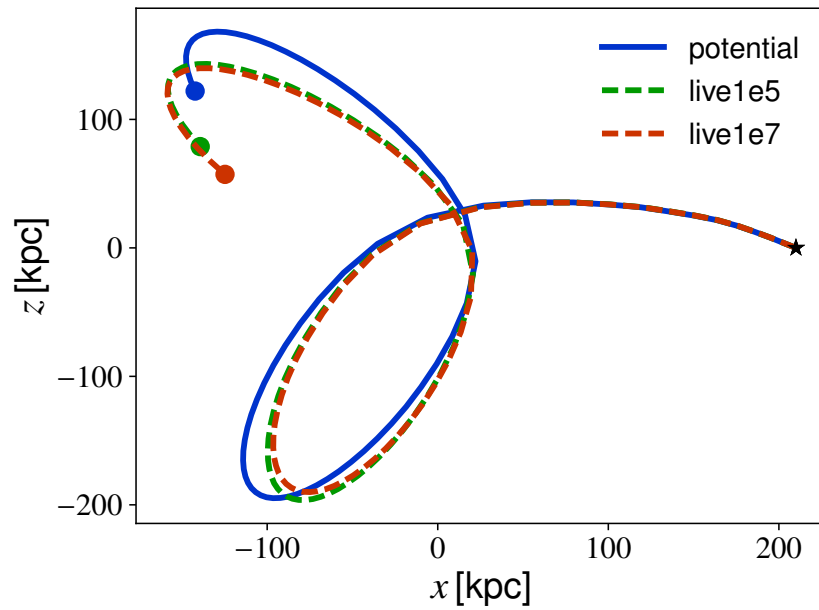


Figure 7.2: Projection of *orbit II* onto the $x - z$ plane comparing the evolution in an analytic potential (blue), in a live halo with 10^5 (green) and 10^7 (red) dark matter particles. A star marks the start of the orbit while the dot marks the end.

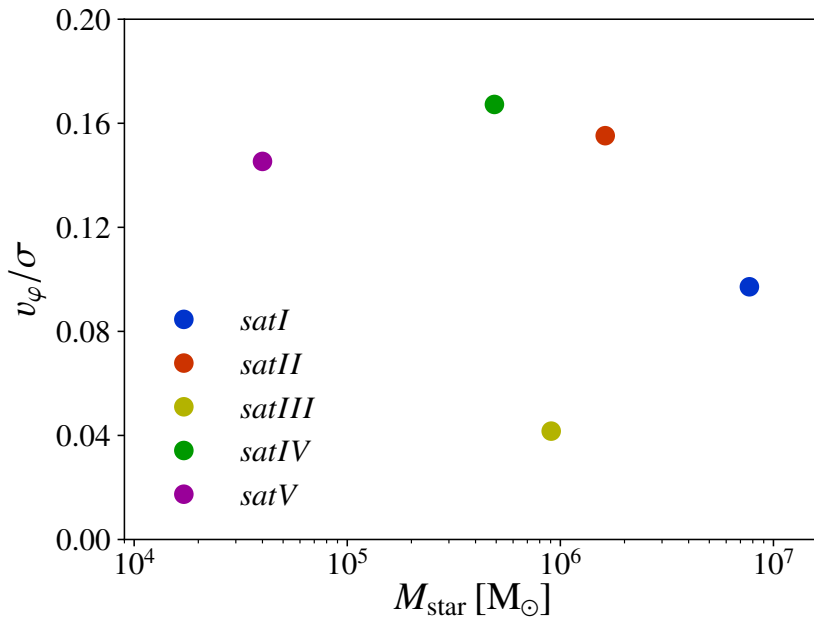


Figure 7.3: Amount of rotation along the axis of total stellar angular momentum of the stars compared to stellar velocity dispersion as a function of stellar mass.

\vec{e}_{ϕ} is set as the circumferential direction with respect to the axis defined by the total stellar angular momentum of stars within the half mass radius. The velocity dispersion σ is simply given by $\sigma = \sigma_{3D}/\sqrt{3}$, where σ_{3D} is the three dimensional velocity dispersion of the stellar particles in the half mass radius. As shown in Fig. 7.3 our galaxies show that there is not much rotational support and their structure can be described by a single isotropic component with practically no signs of a stellar disk even before infall. This is in agreement with previous studies which showed that in cosmological simulations isolated dwarf galaxies as well as satellite galaxies at the low mass end seem to be dispersion supported systems (Wheeler et al., 2017).

However this is quite different from several previous works studying satellite-host interaction, which usually adopted values of $v_{\text{rot}}/\sigma \approx 2$ (Kazantzidis et al., 2017) with a well defined disk component, and then witness a “morphological transformation” within the host halo (Lokas et al., 2010). In our case no morphological transformation is needed since cosmological simulations seem to indicate that galaxies, on our mass scales, are already quite “messy” and do not show the presence of a stellar disk.

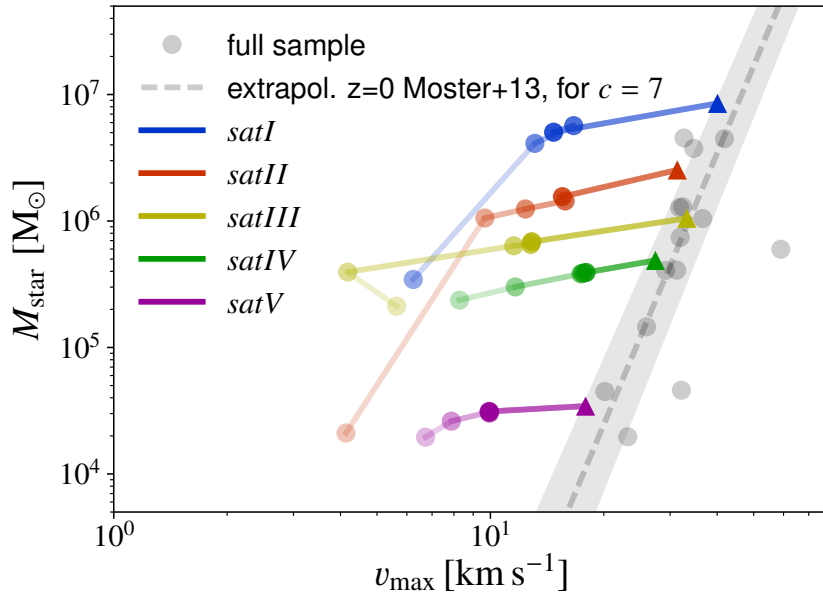


Figure 7.4: The stellar mass within three stellar 3D half mass radii (at infall) as a function of the maximum circular velocity. The gray band shows the Moster relation and its errors translated to a function of v_{\max} for a concentration of $c = 7$. Triangles denote the isolated simulations while the filled circles denote the different orbits. The more violent the orbit, the fainter is the color of the dots.

7.2.2 Environmental effects on galaxy properties

All the satellites survive till redshift $z = 0$ on orbits from *orbitI* to *orbitV* with the exception of *satI* on *orbitV*, since in this case our centering algorithm is not able to find a well defined stellar (or dark matter) center for the satellite, as it is also confirmed by a visual inspection which shows the satellite being completely destroyed. The same happens for the radial orbit scenario, in which all satellites are destroyed with no exceptions. Since in this work we are interested in the properties of “alive” satellites at $z = 0$, we will therefore focus on *orbitI* to *orbitV* for all our satellites but excluding *orbitV* for *satI*.

Mass loss and abundance matching

In Fig. 7.4 we show the stellar mass within three half mass radii at infall as a function of the maximum of the total circular velocity profile v_{\max} . The half light radius is determined by the radius of a sphere around the center of the satellite containing half of its stellar mass, we will refer to this measure

as the $3D$ half mass radius. The (colored) triangles mark the results for the isolated runs at redshift zero. The (colored) filled circles represent the runs in the disk+halo potential, same colors refer to the same satellite (they are also connected by a line to facilitate the comparison), while the strength of the color goes from dark to faint as the orbit becomes more destructive, i.e. from orbits (*orbitI* to *orbitV*). We will use the same color scheme in the rest of the chapter. Finally the grey circles represent the full sample of halos presented in chapter 6 at $z = 1$ and are only added for comparison.

The dashed grey line shows the extrapolation to low mass halos of the abundance matching relation from (Moster et al., 2013) and its error band. Since for satellites it is hard to define the total halo mass we have translated this last quantity into a maximum circular velocity. This has been assuming a NFW potential for the total matter distribution with concentration $c = 7$ (which is the average concentration of our simulated halos) and also assuming that the maximum circular velocity occurs at the radius $r = 2.16 r_s$ (Bullock et al., 2001) where r_s is the NFW scale radius.

Our galaxies started on the abundance matching relation (grey circles, see also chapter 6), and they remain there when run in isolation (colored triangles). Then depending on the orbit, they leave the relation as a consequence of tidal stripping. For quiet orbits they move almost parallel to the x-axis (i.e. with constant stellar mass), meaning that the central region of the satellite is fairly unaltered, then for more disruptive orbits also the stellar component is affected and the stellar mass can shrink to up to 1% of its initial value. Overall the satellites seem to perform a characteristic curve in the stellar mass vs. maximum circular velocity plane due to tidal stripping.

It is interesting also to look at the time evolution of the dark matter mass near the (luminous) center of our halos. In Fig. 7.5 we show the evolution of the dark matter mass enclosed in 10% of the initial (at infall) virial radius for all our satellites on the same orbit, namely *orbitII*.

Until the first pericenter passage at $t \approx 8$ Gyr the dark matter mass is more or less stable with the exception of *satIV* in which a (sub)substructure that passed nearby the center led to an overestimation of the initial enclosed mass. During the first pericenter passage the satellites lose about half their inner dark matter mass. Then we find again a quite stable period until the second pericenter passage at $t \approx 11$ Gyr, when the satellites are stripped again and left with 15 – 50% of their initial dark matter mass at redshift $z = 0$.

The second stripping event, corresponding to the second pericenter passage, occurs in the time range 11 to 12 Gyr for all the satellites. The more massive satellites however seem to experience this event earlier (shortly after 11 Gyr) than the less massive ones. This implies a sort of "decay" of the orbital trajectory for more massive satellites even in the absence of dynamical friction. This

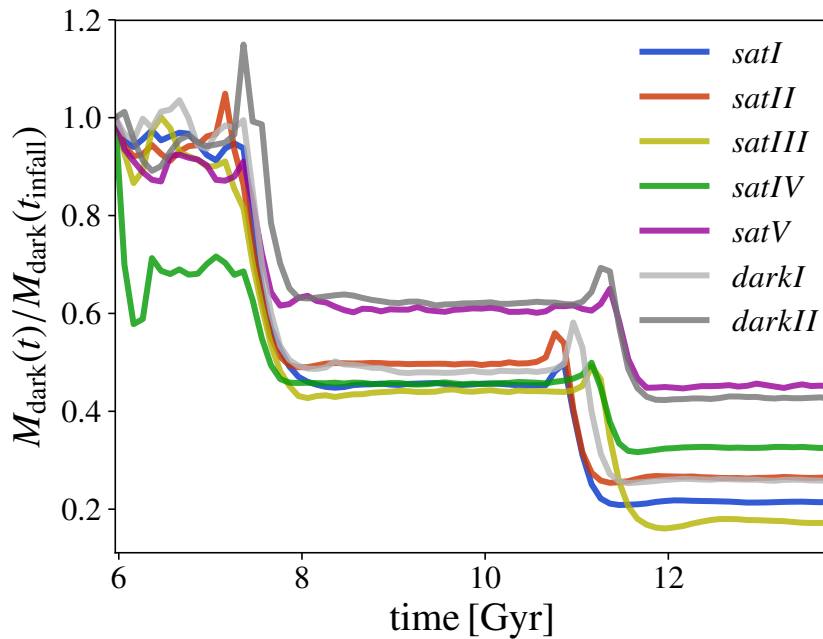


Figure 7.5: Evolution of the dark matter mass in terms of the dark matter mass at infall of the seven satellites on *orbitII*. Only the mass in 10% of the virial radius at infall is considered.

can be ascribed to the different redistribution of energy and orbital angular momentum between stripped material and the satellite remnant. Finally in Fig. 7.6 we show the evolution of the dark matter mass this time for a single satellite (*satII*) on all five orbits. The fraction of dark matter remaining in the halo at redshift $z = 0$ varies from 30% on *orbitI* to just a few percent on *orbitV*.

Stellar mass assembly

We now turn our attention to the luminous part of the satellites. The evolution of the stellar mass in the cosmological simulations until redshift $z = 1$ (dashed) and physical simulations (solid) is shown in Fig. 7.7 for the isolated run and *orbitII* (faint lines).

The stellar mass as a function of time is reconstructed from the formation times of the individual stellar particles. All stellar particles that remain within 10% of the virial radius $r_{200,\text{infall}}$ at infall at redshift $z = 0$ are considered and weighted with their initial stellar mass $m_{\text{star,init}}$. We will use the virial radius at infall as a scale for the dark matter halo during the satellite evolution and we will refer to it just as the virial radius r_{200} . The star formation before infall has

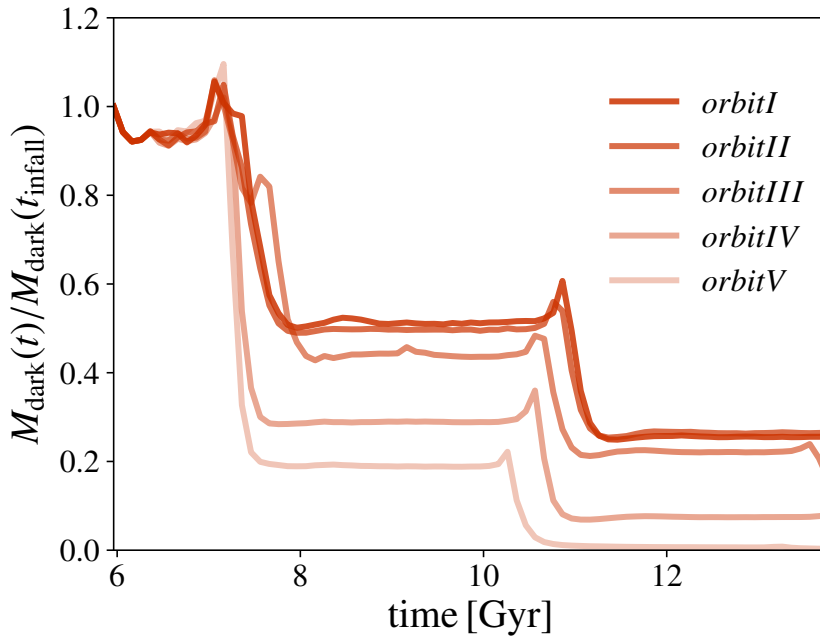


Figure 7.6: Evolution of the dark matter mass in terms of the dark matter mass at infall for *satII* on the five orbits. Only the mass in 10% of the virial radius at infall is considered.

been further investigated in (Macciò et al., 2017). The galaxies show various behaviours of star formation in isolation, from absence of star formation in *satV* to a starburst due to a merger with substructure in *satII*. On the orbit however the star formation plays no or at least a minor role.

Metallicity

We present the mass weighted stellar metallicity as a function of stellar mass enclosed in a sphere of three 2D half mass radii in Fig. 7.8. Where the 2D half mass radius is defined as the radius of a cylinder along the z -axis (our line-of-sight) containing half of the galaxy stellar mass.

As before the triangle marks the position of the isolated simulation, while the different colored circles mark the results for the different orbits, with faint colors being associated with more disruptive orbits. The grey circles and triangles represent observational results for the Milky Way and the M31 galaxy respectively. Our isolated runs nicely reproduce the observational trend from Kirby et al. (2014), with the exception of *satV*, the apparent failure of this satellite is related to the very short time scale of star formation compared with the time-step of the simulation, which does not allow for a proper treatment of the

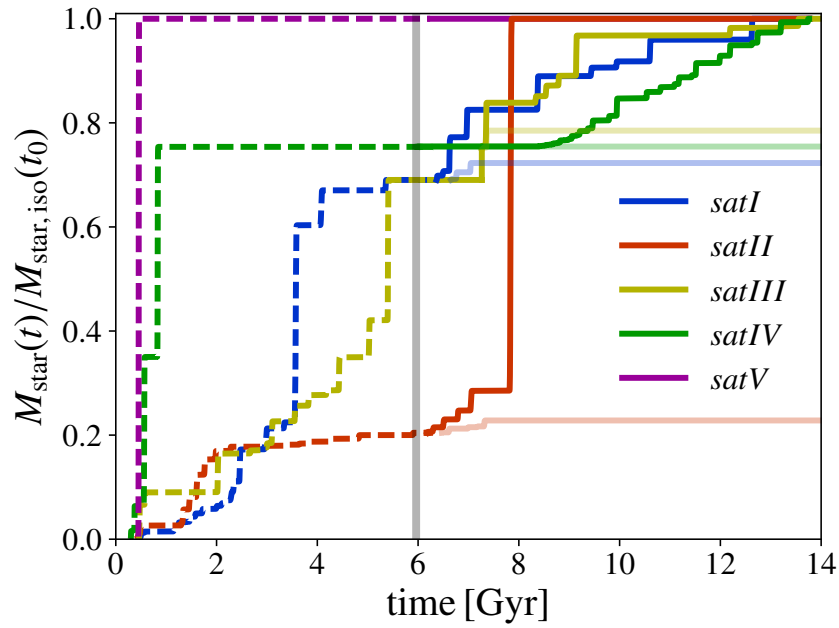


Figure 7.7: Evolution of the stellar mass of the 5 luminous satellites before (dashed) and after (solid) the infall time ($z = 1$). Isolated runs are shown with darker colors while orbits (specifically *orbitII*) are shown with fainter ones. The stellar mass is shown in terms of the stellar mass at time $z = 0$.

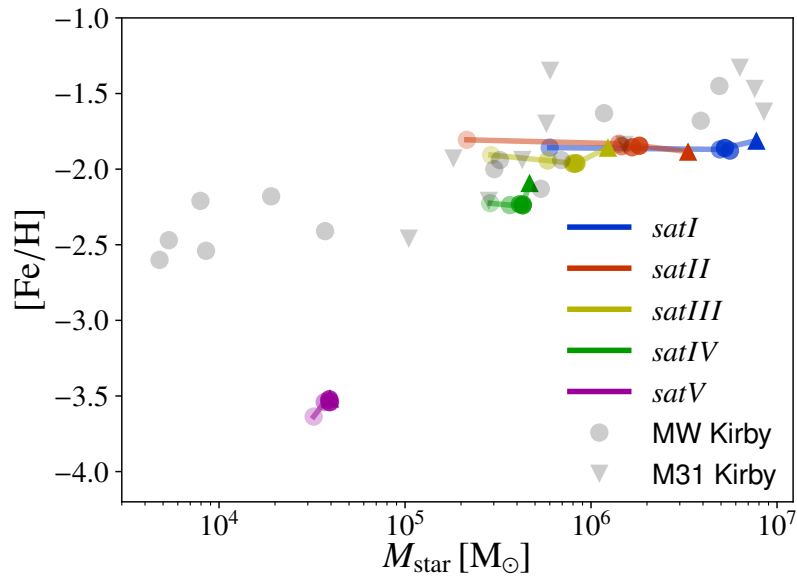


Figure 7.8: Metallicity as a function of the stellar mass. The colored triangles denote the isolated simulations while the filled circles denote the different orbits. The more violent the orbit, the fainter is the color of the dots. Observations of Milky Way and M31 satellites from (Kirby et al., 2014) are shown as grey dots and triangles, respectively.

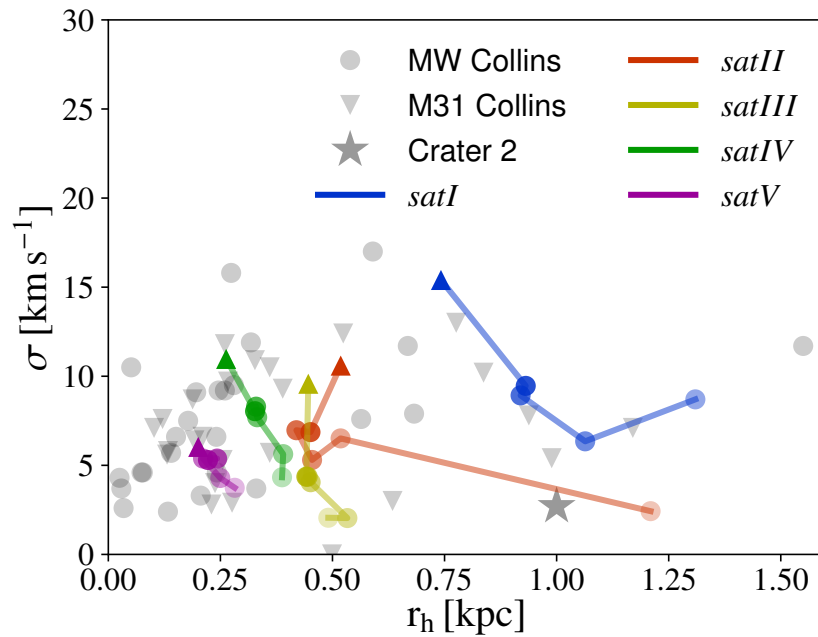


Figure 7.9: Projected velocity dispersion inside the stellar 2D half mass radius as a function of the stellar 2D half mass radius. colored triangles denote the isolated simulations while the filled circles denote the different orbits. The more violent the orbit, the fainter is the color of the dots. Observations of Milky Way and M31 satellites (for references see section 7.2.2) are shown as grey dots (and a star for the recently discovered satellite Crater 2) and triangles, respectively.

enrichment (see chapter 6 for a thorough explanation of this issue).

When the satellites are exposed to the presence of a central halo, they do lose stellar mass (as expected), but they still move parallel to the relation, with an almost constant metallicity, due to the very low metal gradient in their stellar population.

Stellar kinematics

The effect of accretion onto a more massive galaxy is instead clearly visible in the velocity dispersion-size relation which is shown in Fig. 7.9. The size (r_h) is again the 2D half mass radius already introduced above, while the velocity dispersion is the 1D dispersion along the line of sight (the z -axis in our case) computed within r_h . In this plot the observational data are represented by grey dots and triangles for Milky way and M31 satellites, respectively. They are taken from a compilation from M.Collins (private communication) including

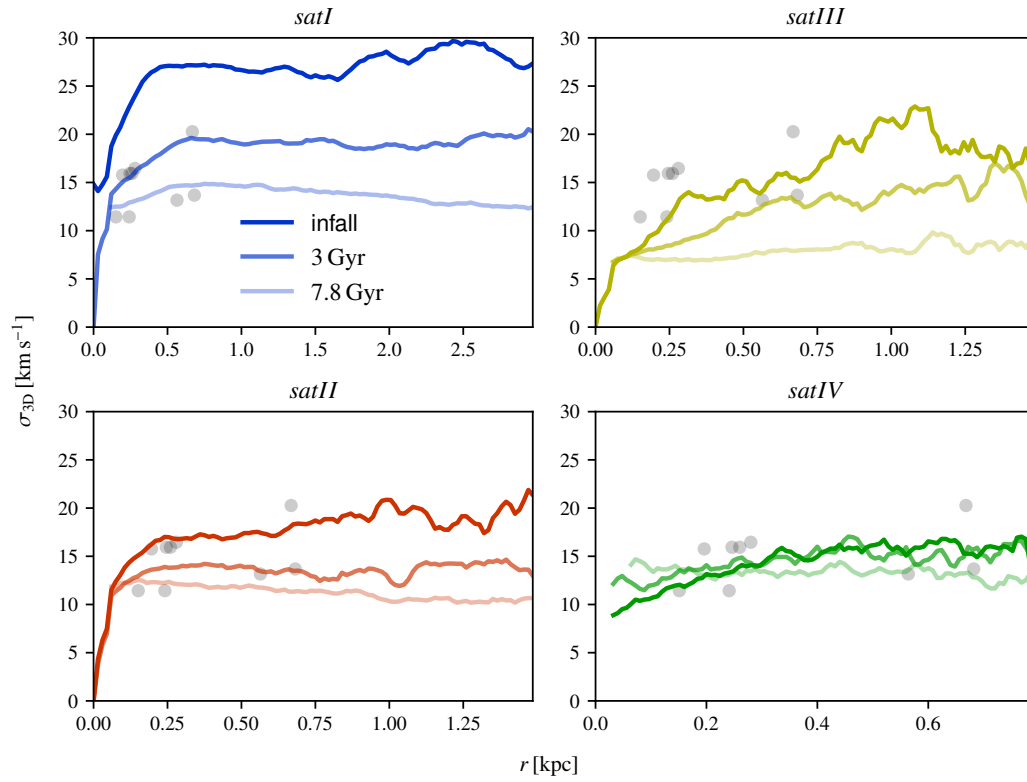


Figure 7.10: Three dimensional velocity dispersion of the stellar particles on *orbitII* evaluated at infall (solid), 3 Gyr and 7.8 Gyr ($z \approx 0$) (faint, solid). Grey points denote line of sight velocity dispersion measurements from Walker et al. (2009) of the nine most massive Milky Way satellites rescaled by a factor of $\sqrt{3}$ (Wolf et al., 2010).

data from Walker et al. (2009) for the Milky Way and Tollerud et al. (2012, 2013); Ho et al. (2012); Collins et al. (2013); Martin et al. (2014) for M31 satellites. The size and dispersion measurements of the recently discovered satellite Crater 2 are taken from Caldwell et al. (2017).

Our isolated halos (triangles) lie well within the relation as were our initial conditions (see chapter 6). Stripping and tidal forces modify both the size and the velocity dispersion of the galaxies, which, depending on the orbit, at redshift zero tend to occupy the whole space covered by the observations.

It is interesting to note that simulated galaxies with larger sizes tend to have a larger deviation (both in size and dispersion) from the isolated runs, suggesting that small galaxies tend to be more resilient to tidal effects. Overall the scatter in our simulated size-dispersion velocity is in very good agreement with the observed one. Further we want to emphasize that *satII* and *orbitV* end up with an extremely low velocity dispersion at a half mass radius of about 1.2 kpc. This is in very good agreement with the properties of the recently discovered Crater2 satellite (Caldwell et al., 2017). This implies that the formation of such extended and cold structures is not a challenge for the current LCDM model, which can be explained as highly perturbed objects (see also Munshi et al. (2017)).

To better understand the time evolution of the stellar kinematics in our satellites, in Fig. 7.10 we show the radial profile of the three dimensional stellar velocity dispersion on *orbitII* at three different times: at infall and after 3 and 7.8 Gyr (corresponding to redshift $z = 0$). Here we only consider *satI* to *satIV* because *satV* has not sufficient stellar particles to resolve the kinematics properly (see Table 7.1). In the same plot we also show as reference (grey circles) the line of sight velocity dispersion measurements for the nine most massive Milky Way satellites at the half light radius from Walker et al. (2009) rescaled by a factor of $\sqrt{3}$ (see Wolf et al., 2010)). As time goes by the mass (DM+stellar) loss causes an overall decrease of stellar velocity dispersion, which also tends to become more isothermal, with a very flat distribution (see for example the case for *satIII*) at redshift zero. We ascribe this effect to the particle phase space mixing due to tidal effects, which seems to “thermalize” the galaxy.

Another interesting (and measurable) quantity to look at is the circular velocity, defined as $v_{\text{circ}} = \sqrt{\frac{GM(<r)}{r}}$, where $M(<r)$ is the total mass enclosed in a sphere with radius r around the center. In Fig. 7.11 we show the final ($z = 0$) circular velocity radial profile for all our seven satellites and for different orbits. In each panel the black line represents the isolated run, while the colored lines are the orbit runs, with, as before, fainter colors for more disruptive orbits. We also show, as in the previous figures, the observations of the

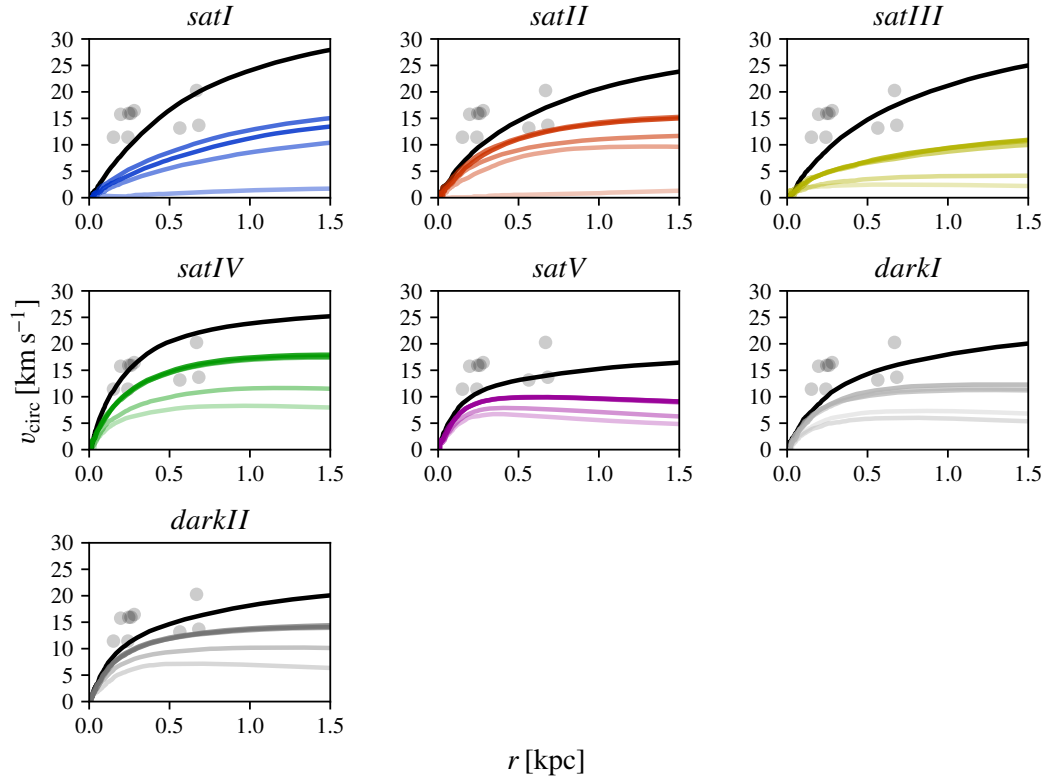


Figure 7.11: Circular velocity profiles for the five luminous satellites for the isolated run (black) and the orbits (color coding as before). The more violent the orbit, the fainter is the line color. Grey points denote line of sight velocity dispersion measurements from Walker et al. (2009) of the nine most massive Milky Way satellites rescaled by a factor of $\sqrt{3}$ (Wolf et al., 2010).

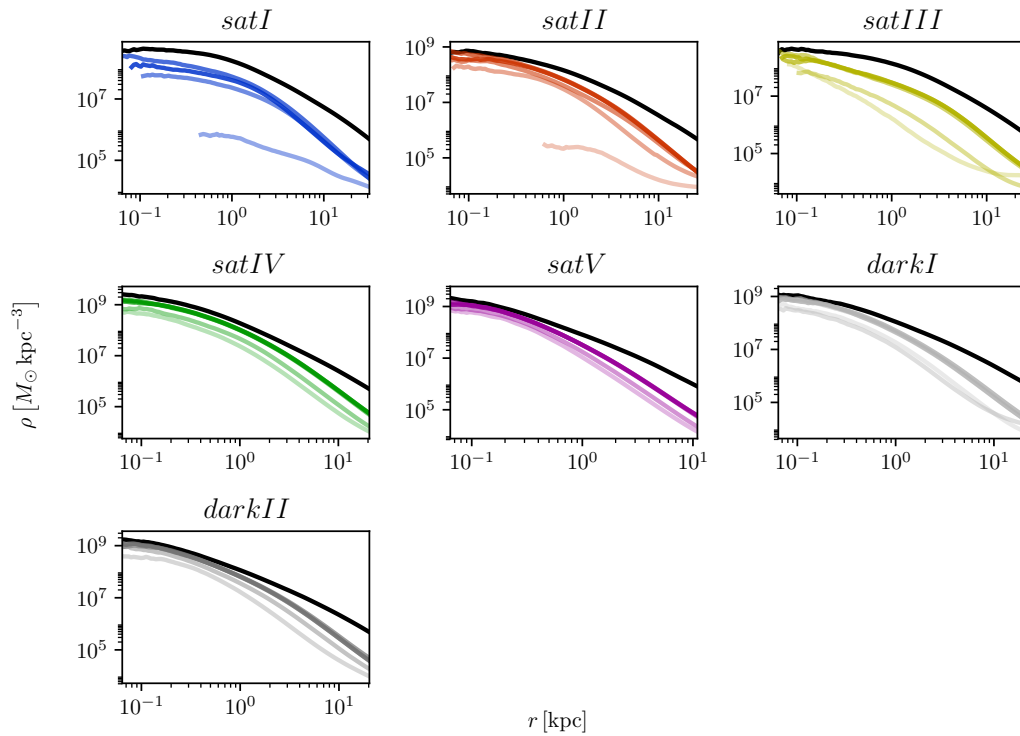


Figure 7.12: Dark matter density profile of all the satellites in isolation (black) and on the orbits (color coding as before) at redshift $z = 0$. The more violent the orbit, the fainter is the line color. The profiles are shown from twice the softening length up to the virial radius at infall.

nine most massive Milky Way satellites as an orientation (data from [Walker et al., 2009](#)). As already noted in previous studies, circular velocity profiles can be significantly lowered in the inner few hundred parsecs, even without losing a large amount of mass on these scales (see Fig. 7.4). The profiles also tend to evolve in a sort of self-similar way, preserving their initial shape, with the exception of the most extreme orbit.

7.2.2.1 Evolution of the dark matter profile

We now turn our attention to the dark (matter) component of our satellites. In Fig. 7.12 we show the redshift zero dark matter distribution for all our galaxies in the various runs at redshift $z = 0$, as before the black line represents the isolation run, while the colored lines are for the different orbits. The profiles are shown from twice the gravitational dark matter softening to the virial

radius at infall (the exceptions are satellites *satI*, *satII* and *satIII* on the most extreme orbit, since they end up with a very low dark matter content at $z = 0$ and which pushes the convergence radius to larger scales). As expected the tidal stripping due to the central potential is stronger in the outer parts of the profile, which depart more from the isolation case. On the other hand the stripping does not happen in an “onion-like” fashion, with the outer part being progressively removed while the center remains unaltered. On the contrary, the whole profile reacts to the stripping and the central density is also lowered even on the most mild orbits. This global reaction can be ascribed to the typical box orbits of dark matter particles (e.g. Bryan et al., 2012), which allow particles in the center at a given time step, to spend quite some time in the outskirts of the halo at a subsequent time, and hence are prone to be stripped.

As already described in chapter 6, some of our satellites (*satI*, *satII*, *satIII* as shown by the isolation runs) start with a cored dark matter profile (or at least a profile with a shallower slope than NFW), this is due to the fact that for those satellites, the star formation rate is vigorous enough to create large gas outflows, which in turn flatten the dark matter profile (Read & Gilmore, 2005; Pontzen & Governato, 2012; Macciò et al., 2012b; Di Cintio et al., 2014; Oñorbe et al., 2015). Fig. 7.12 seems to suggest a steepening of the profile during its evolution. To better look into this possibility we plot in Fig. 7.13 the inner logarithmic dark matter density slope α as a function of stellar mass. The slope α is computed between 1-2% of the initial (at infall) virial radius, following Tollet et al. (2016) and chapter 6; the triangles mark the isolation runs, while the circles represent the different orbits, finally the stellar mass for the two dark halos has been arbitrarily set.

No matter if the halo contained stars or not, or whether it starts with a flattened profile (blue and yellow symbols) or with a cuspy one (green symbols), in all cases the effect of accretion is to steepen the dark matter profile. It is important to notice that the profile steepening is not due to a contraction of the halo but it is due to a slightly stronger mass removal in the outer regions of the halo with respect to its very center.

In Fig. 7.12 we do not show the final density profile slope for *satI* (blue), *satII* (red) and *satIII* (yellow) for the most extreme orbit. This is because at $z = 0$ these satellites do not have a clear dark matter center to build the profile. It is nevertheless interesting to look at the evolution of the dark matter profile as a function of time before the satellite disruption. This is shown in Fig. 7.14 where we present the difference of the density slope α w.r.t. to the isolation case as a function of time: the plots show *satI* (blue line), *satII* (red line) and *satIII* (yellow line) on *orbitIV* (for *satI*) and *orbitV* (for *satII* and *satIII*), respectively, and the profile slopes are averaged over five time-steps to

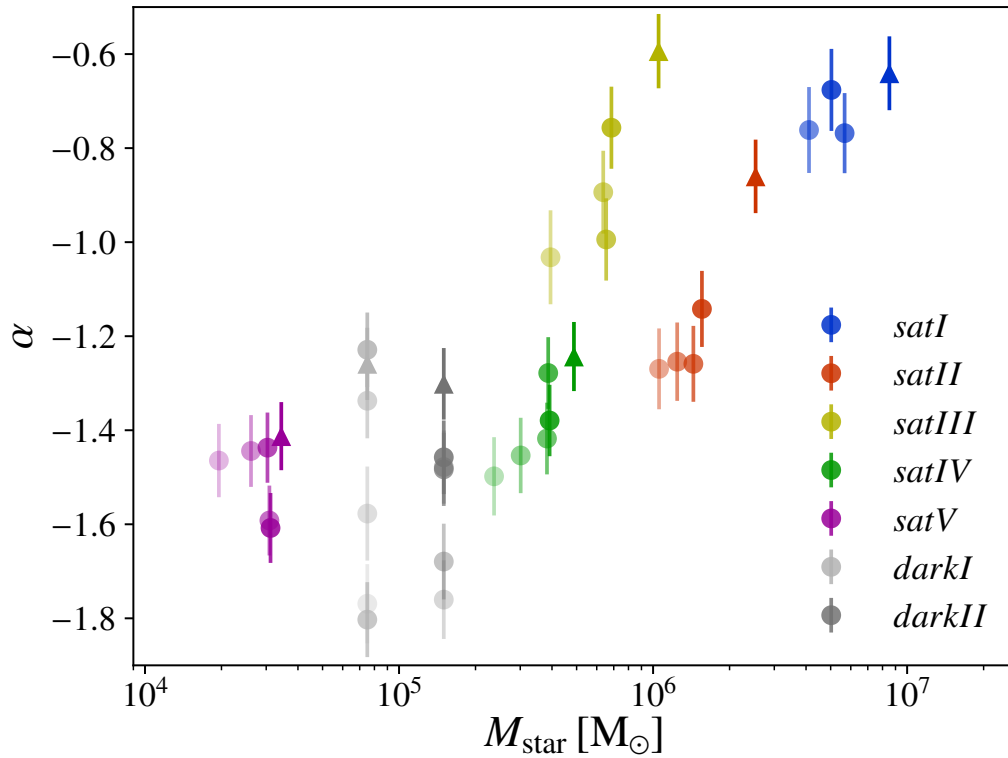


Figure 7.13: Inner logarithmic slope of the dark matter density profile α fitted between 1% and 2% of the virial radius as a function of stellar mass inside three 3D half mass radii. Stars denote measurements at infall, while triangles denote the isolated simulations and filled circles the orbit runs at redshift $z = 0$. The more violent the orbit, the fainter is the color.

reduce the noise. It is evident that the steepening of the profile is present even for satellites that are completely shredded apart by tidal forces.

When the results are combined with those of chapter 6, they imply that the observational discovery of a dark matter core in one of the low mass satellites of our own Galaxy will strongly challenge the predictions of the Λ CDM model. It will be very difficult to explain such dark matter core invoking the effect of baryons (see chapter 6 and triangles in Fig. 7.13) or the effect of environment and accretion (again Fig. 7.13). The discovery of a flat dark matter distribution will then be an indication of a different nature for dark matter: warm (but see Macciò et al., 2012a), self interacting (Vogelsberger et al., 2014b; Elbert et al., 2015) or even more exotic models (e.g. Macciò et al., 2015).

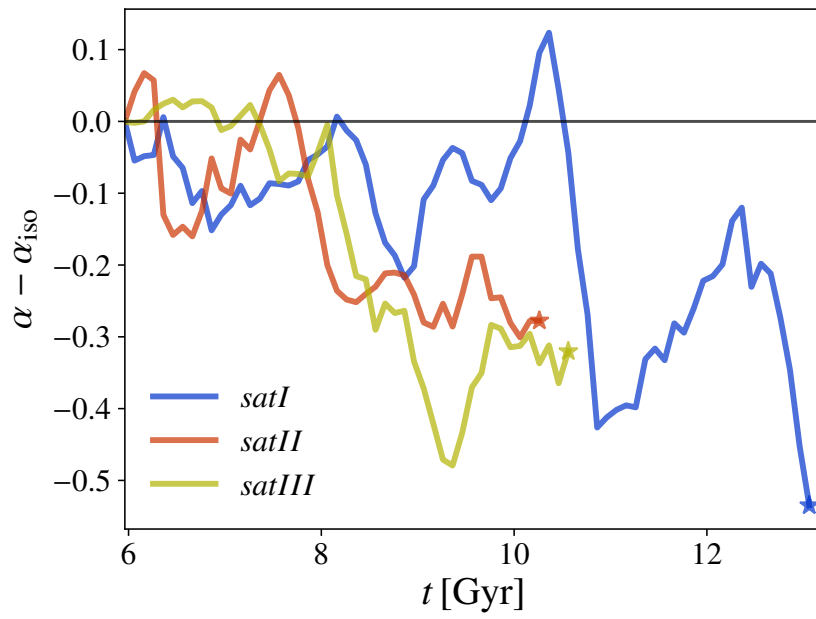


Figure 7.14: Time evolution of the deviation of α on *orbitIV* and *orbitV* from α_{iso} (for the isolated runs) for *satI*, *satII* and *satIII*, respectively. The stars denote the time where there are less than 150 dark matter particles left inside a sphere of a radius of $1\% r_{200}$.

7.2.2.2 Central dark matter density slope and satellite survival

Previous works studying environmental effects on satellite galaxies (e.g. Kazantzidis et al., 2004a; Peñarrubia et al., 2010, and references therein) have shown that satellites with cored dark matter density profiles are more easily stripped and disrupted than cuspy ones. The results shown in Fig. 7.13 seemed to confirm such a correlation also in our cosmologically based simulations, but we want to be more quantitative.

In Fig. 7.15 we show the ratio of the dark matter enclosed within three half mass radii for the different satellites on the different orbits with respect to the isolated case as a function of the initial (at infall) density profile slope at redshift $z = 0$. It is quite evident that on every orbit, cuspy satellites like *satV* ($\alpha_{\text{infall}} = -1.5$) are able to retain a larger fraction of their initial mass than cored ($\alpha_{\text{infall}} > -1.0$) satellites like *satI* and *satIII*. These cored satellites lose more than 70% of their initial (dark) mass even on the more gentle orbit (darker colors) and up to almost 100% on the most extreme ones (fainter colors).

The different initial dark matter density slope also affects the stellar mass loss, since the dark matter acts as shield for the stars. In Fig. 7.16 we plot the mass loss as defined in Fig. 7.15 as function of the initial dark matter profile density slope but this time for stars and dark matter. In order to avoid a too crowded plot we only show results for *orbitIV*, which is the most disruptive orbit for which all five satellites still have a well defined center.

In general stars are more resilient to tidal forces than dark matter, and this is due to their smaller spatial extent and larger stellar density; for example *satIII* is able to retain 40% of its stars while it is practically totally stripped of dark matter. Nevertheless there is still a correlation between the stellar mass loss and the initial dark matter slope. An exception to this relation seems to be given by *satI*, which has a very strong mass loss both in the stellar and dark matter components despite having a similar α_{infall} as *satIII*. This is due to the different slope for the *stellar* density profiles between *satI* and *satIII*, while the first satellite has a slope of -1.80 (again evaluated between 1 and 2% of the virial radius), the stellar slope for *satIII* (and all the other satellites) it is close to -3.0 . This difference in stellar slope is most likely related to a major merger event that occurred for *satI* shortly before redshift one and strongly reshuffled the stellar particle orbits.

Finally we note that some satellites (especially *satI*) are left at $z = 0$ with practically no dark matter in their central region, where they are fully stellar dominated, resembling more an extended globular cluster than a dwarf galaxy, we plan to look more into this issue in a forthcoming paper.

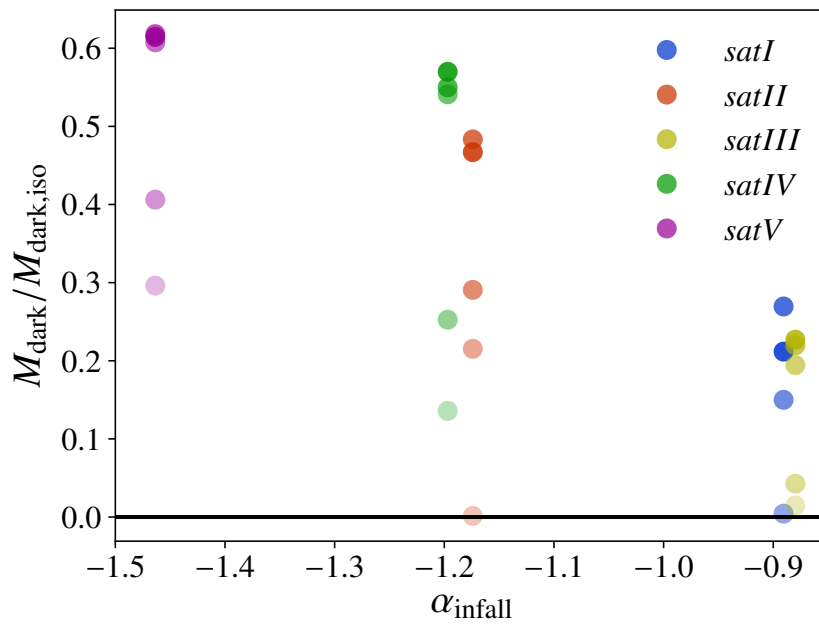


Figure 7.15: Dark matter mass enclosed in a constant sphere with a radius of three stellar half mass radii at infall on the individual orbits compared to the isolated run as a function of the central dark matter density slope at infall α_{infall} .

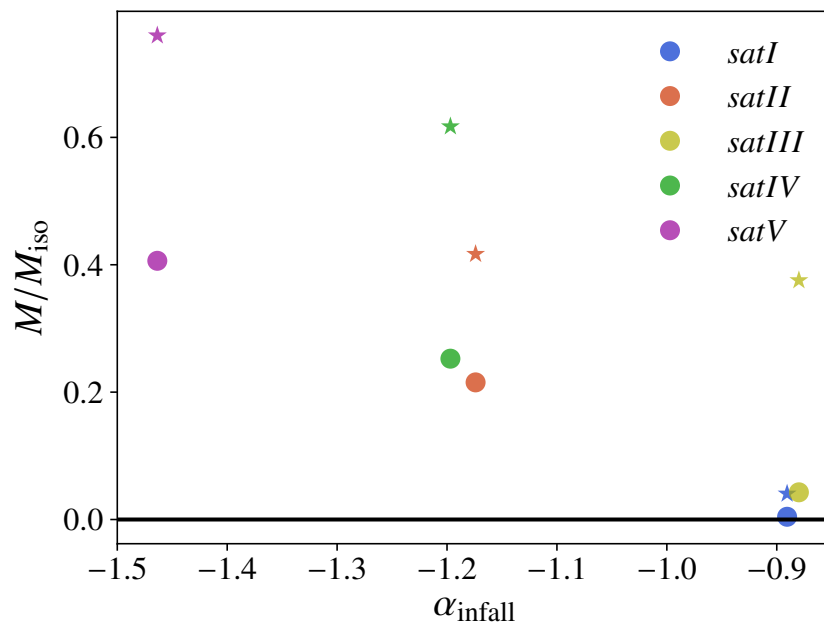


Figure 7.16: Dark matter (dots) and stellar (stars) mass enclosed in a constant sphere with a radius of three stellar half mass radii at infall on *orbitIV* compared to the isolated run as a function of the central dark matter density slope at infall α_{infall} .

Part IV

Warm dark matter

In this second part I present the results from a repetition of the analysis done in chapter III but replacing the cold dark matter with a 3 keV warm dark matter model. It is based on the third paper in the series “The edge of galaxy formation” (Frings, Macciò (in prep.)) that is currently in preparation.

8 Introduction

In part III we focused on the formation of the smallest galaxies in a Λ CDM universe and predicted the scaling relations for field galaxies as well as the deviation from those relations due to interaction with a Milky Way like host galaxy on their way of becoming satellites and further compared our results with current observational data. Now we want to look at the influence of the nature of dark matter onto the smallest galaxies. In our standard model the dark matter is thermally produced in the early universe which, depending on the dark matter particle mass, leaves the particles at non-zero thermal velocities at the formation time (see section 3.4). For large masses and hence small thermal velocities we speak of cold dark matter. For lower masses, however, the thermal speeds are large enough to damp the dark matter power spectrum efficiently at relevant scales and we speak of Warm Dark Matter (WDM). This damping scales is directly related to the particle mass and strongly effects the structures we see in the Universe today. In this study we want to investigate the effect of warm dark matter with a particle mass of $m = 3 \text{ keV}$ on properties of field dwarfs and satellite galaxies of the Milky Way. Even if the particle mass is ruled out by the most recent constraints from Lyman- α forest observation in high redshift quasar spectra (after the beginning of the project) that allow dark matter particle masses down to 3.5 keV (Iršič et al., 2017), the model makes the effects of the warm dark matter emerge more clearly and lets us disentangle them more easily from other effects.

9 Dwarf galaxies

9.1 Simulations

We performed a total of 42 hydrodynamical zoom-in simulations of 21 halos both in a CDM and WDM scenario using the smoothed particle hydrodynamics code GASOLINE2 (Wadsley et al., 2017). Compared to chapter III we updated the cosmological parameters according to (Ade et al., 2014): Hubble parameter $H_0 = 67.1 \text{ km s}^{-1} \text{ Mpc}^{-1}$, matter density $\Omega_m = 0.3175$, dark energy density $\Omega_\Lambda = 1 - \Omega_m - \Omega_r = 0.6824$, baryon density $\Omega_b = 0.0490$, normalization of the power spectrum $\sigma_8 = 0.8344$, slope of the initial power spectrum $n = 0.9624$. The code setup is described in detail in Wang et al. (2015) and is similar to the one described in chapter 6 but including the changes related to the migration to GASOLINE2 as described in section 4.4.

The halos were initially selected as isolated overdensities in two dark matter only cosmological volume box simulations. The first box with a volume of 20^3 Mpc^3 and 300^3 particles was already used in the NIHAO project (Wang et al., 2015) and the CDM runs of the halos selected from this box are galaxies from the NIHAO sample. In addition we ran a box with a volume of 10 Mpc^3 and 600^3 particles from which we chose further halos to increase the size of our sample and we also ran both volumes in a WDM scenario. As a result of the thermal production in the early Universe, the microscopic warm dark matter particles retain non-zero streaming velocities. These restrict the accessible phase space volume for the dark matter fluid and smooth the density field below a certain length scale. However, assigning thermal velocities to the macroscopic particles in a simulation with masses of the order of $10^4 M_\odot$ is not correct. On the other hand, for a particle mass of 3 keV the streaming velocities are smaller than the Zel'dovich velocities (see Macciò et al. (2012b)) introduced in section 4.3 and therefore lie below our resolution limit. Hence we only need to describe the damping of small scales introduced by the streaming velocities in the linear WDM power spectrum P_{WDM} that is related to the CDM power spectrum P_{CDM} by the transfer function $A^2(k)$ (see section 3.4). We use a fitting formula

$$A^2(k) = \frac{P_{\text{WDM}}}{P_{\text{CDM}}} = [1 + (\alpha k)^{2\nu}]^{-10/\nu} \quad (9.1)$$

Table 9.1: Name, virial mass, stellar mass, stellar particle number and dark matter particle mass. Data from the CDM and WDM runs are indicated by blue and red background colors, respectively. The gravitational softening for the stellar particles ranges from $\varepsilon_{\text{star}} = 90$ pc to $\varepsilon_{\text{star}} = 40$ pc depending on resolution.

Name	$M_{200}[\text{M}_{\odot}]$	$M_{200}[\text{M}_{\odot}]$	$M_{\text{star}}[\text{M}_{\odot}]$	$M_{\text{star}}[\text{M}_{\odot}]$	N_{star}	N_{star}
g8.94e8	8.19e+08	2.31e+08	0	0	0	0
g1.89e9	1.42e+09	1.07e+09	0	0	0	0
g3.54e9	2.85e+09	2.51e+09	3.89e+05	0	4704	0
g3.67e9	3.12e+09	2.56e+09	9.20e+04	0	1110	0
g4.36e9	9.71e+09	5.43e+09	3.30e+04	0	38	0
g4.48e9	3.63e+09	3.13e+09	6.51e+05	9.69e+04	7883	1172
g4.99e9	5.70e+09	4.29e+09	3.76e+05	0	538	0
g5.22e9	6.30e+09	3.48e+09	1.17e+05	0	171	0
g5.59e9	6.43e+09	6.28e+09	1.73e+06	7.00e+05	2509	1012
g6.31e9	5.13e+09	4.48e+09	3.71e+05	2.48e+02	4457	3
g7.05e9	1.05e+10	8.68e+09	2.26e+06	2.01e+06	3230	2854
g8.63e9	5.59e+09	4.34e+09	5.90e+05	0	2022	0
g9.91e9	7.42e+09	7.25e+09	1.50e+06	8.96e+05	5238	3097
g1.17e10	8.60e+09	9.07e+09	3.34e+06	2.90e+06	11613	10109
g1.18e10	1.09e+10	1.44e+10	3.37e+06	8.73e+06	4887	12551
g1.23e10	9.06e+09	1.32e+10	1.58e+06	2.36e+06	2278	3405
g1.44e10	1.69e+10	1.22e+10	6.64e+06	3.24e+06	9562	4664
g1.47e10	1.52e+10	1.03e+10	8.92e+06	5.15e+06	12910	7476
g1.50e10	1.40e+10	1.22e+10	3.32e+06	2.31e+06	4840	3222
g1.95e10	1.37e+10	1.20e+10	3.79e+06	2.33e+06	5429	3327
g2.94e10	3.22e+10	3.05e+10	5.63e+07	4.75e+07	81608	68629

suggested by [Bode et al. \(2001\)](#) to calculate the transfer function. The parameters are set to $\nu = 1.12$ and

$$\alpha = 0.049 \left(\frac{m_{\text{WDM}}}{1 \text{ keV}} \right)^{-1.11} \left(\frac{\Omega_{\text{DM}}}{0.25} \right)^{0.11} \left(\frac{h}{0.7} \right)^{1.22} h^{-1} \text{Mpc} \quad (9.2)$$

following [Viel et al. \(2005\)](#). For more details and the effects of streaming velocities see [Macciò et al. \(2012a\)](#). We choose a dark matter particle mass of $m = 3 \text{ keV}$ being still at the edge of viability regarding current constraints ([Iršič et al., 2017](#)) and low enough to expect having an observable impact on the dwarf galaxy scale. The counterparts to the objects in the CDM box simulation are identified by tracking the objects' particle id's in the WDM box. Starting from the cosmological volume simulations, we perform zoom-in simulations of the selected objects both in the CDM and WDM scenario. For the NIHAO objects we stick to resolution given by the NIHAO simulations while for the newly selected object we choose the zoom factor such that we end up with at least 10^6 dark matter particles inside the virial radius at redshift $z = 0$. The high resolution dark matter particle mass is $1.9 \times 10^4 M_{\odot}$ for the NIHAO galaxies and their WDM counterparts and lies between 2.4×10^3 and $8.0 \times 10^3 M_{\odot}$ for halos selected from the 10 Mpc box. In [table 9.1](#) we present virial and stellar mass, and stellar particle number (in 10% of the virial radius) for each simulation. Gas particles have an initial mass of $m_{\text{gas,init}} = f_{\text{bar}} \cdot m_{\text{DM}}$ while stellar particle start with initial masses $m_{\text{star,init}} = \frac{1}{3} m_{\text{gas,init}}$, where $f_{\text{bar}} = \frac{\Omega_{\text{b}}}{\Omega_{\text{dark}}}$ is the cosmic baryon fraction.

9.2 Results

While for CDM dwarf galaxies the evolution is essentially finalized at redshift $z = 1$, we will show later in this section that WDM dwarfs show more recent evolution. Hence unlike in [chapter 6](#) we evaluate our sample of cosmological simulations at redshift $z = 0$ to study the properties of dwarf galaxies in the field.

9.2.1 Halo masses

Since structure formation in WDM happens slightly different we first want to look at the virial masses of the halos and how they are effected by WDM. In [fig. 9.1](#) the ratio of virial masses in the WDM and CDM run is plotted against the CDM virial mass. The black line indicates the ratio of one and purple points are the simulation data. We can see that simulations in a WDM scenario end up with consistently less massive halos at the low mass end of

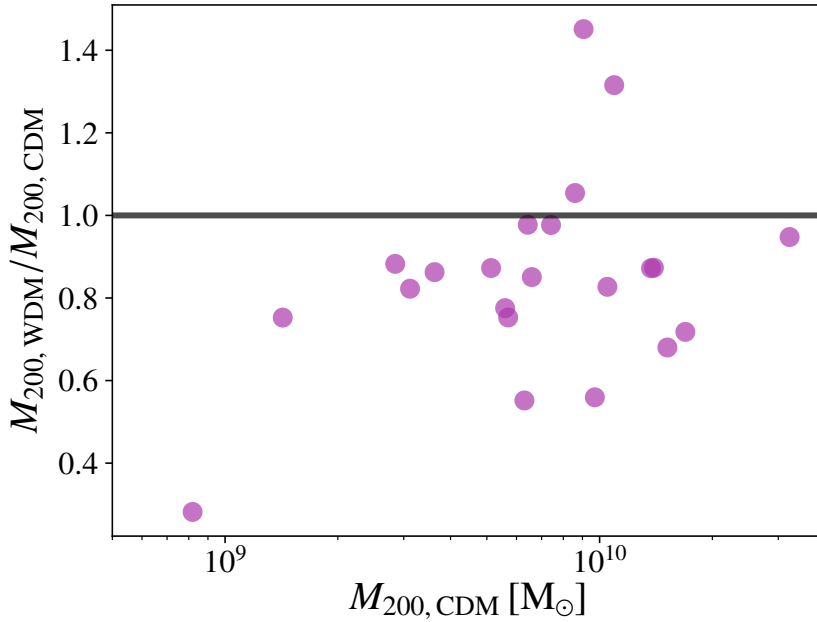


Figure 9.1: Virial mass ratio of WDM to CDM run as a function of virial masses in CDM. The black line indicates the ratio of one and purple points are the simulation data.

the sample. At higher masses the stochasticity of the merging history induces a large scatter which also allows WDM halos to be more massive than their CDM counterparts.

9.2.2 Star formation and luminous fraction

Further we wanted to address is the efficiency for dwarf galaxies to form stars in a warm dark matter scenario. In fig. 9.2 we show the stellar mass of the galaxies (i.e. stars inside 10% of the virial radius) as a function of the virial mass. Throughout this study the virial masses and radii are always given with respect to $200 \rho_c$ (with ρ_c being critical density defined in section 3). The grey dashed line in the background is the low mass extrapolation of the Moster - relation (Moster et al., 2013) and the associated scatter around the relation. Blue and red circles denote halos that form galaxies in their center in CDM and WDM, respectively and triangles the halos that stay dark until redshift zero. We can see that for down to a certain mass scale in both dark matter scenarios halos will always form stars, followed by a region where we can find both luminous and dark halos, and finally a minimum mass below which no star formation takes place. It is interesting to point out that even if there is

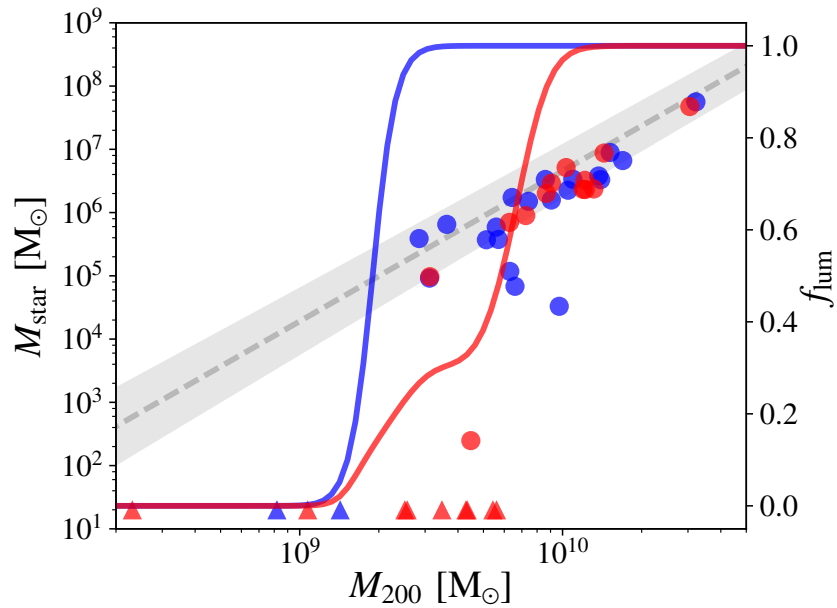


Figure 9.2: Stellar mass versus the virial mass of the halo for the CDM (blue) and WDM (red) simulations. On the second y -axis the luminous fraction of satellites at given halo mass is shown as solid lines. The grey dashed line and band visualizes the extrapolation of the Moster - relation (Moster et al., 2013) to the low mass end and its scatter.

this offset in halo masses (see 9.2.1), the Moster - relation is still fulfilled for the star forming WDM galaxies. In other words, WDM may affect halo masses but not star formation efficiency. However, it seems that for the WDM halos the critical mass for star formation is offset to higher masses. To visualize this we also show the luminous fraction on the second y -axis as solid lines. The luminous fraction is here estimated by assigning the luminous halos the value 1 and the dark ones the value 0 and smoothing the data with a Gaussian of a width that is fixed in logarithmic space. The luminous fraction clearly visualizes the offset in the critical mass for star formation and also seem to show a broader region of masses allowing both dark and luminous halos for WDM. In agreement to 6 we observe an increased scatter of the CDM dwarf galaxies at halo masses below $10^{10} M_{\odot}$, for the luminous WDM halos, however, the relation seems to be slightly tighter. A possible explanation for this we give at the end of section 9.2.4.

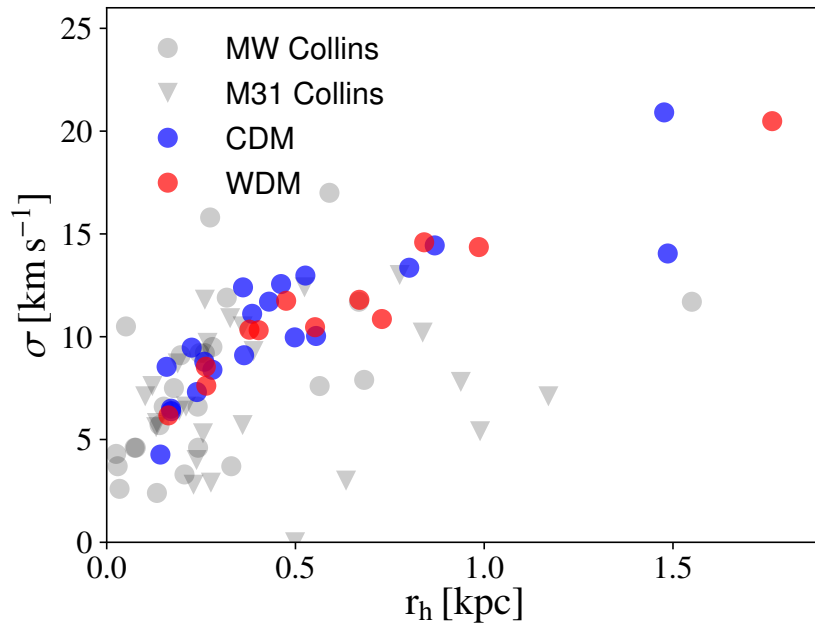


Figure 9.3: Velocity dispersion - size relation. Blue and red circles denote CDM and WDM simulations, respectively and observations of Milky Way and M31 satellites (for references see section 9.2.3) are shown as grey dots and triangles, respectively.

9.2.3 Scaling relations

To compare our simulations with observational data we want to investigate two observable scaling relations, the “dispersion - size relation” and the “metallicity - stellar mass relation”. For this section and the following section we analyzed all simulations containing stars except for the WDM run of $g6.31e9$. We removed this simulation from the sample because it only contains three stellar particles and the deduction of quantities as velocity dispersion and metallicity needs a certain number of stellar particles to be resolved and lead to sensible results. In fig. 9.3 we show the one dimensional velocity dispersion (averaged over the three dimensions) and the projected half mass radius (averaged accordingly). The data are taken from a compilation from M.Collins (private communication) including data from Walker et al. (2009) for the Milky Way and Tollerud et al. (2012, 2013); Ho et al. (2012); Collins et al. (2013); Martin et al. (2014) for M31 satellites. As we already pointed out in chapter 6 the simulations of field galaxies tend to lie on the upper half of the cone spanned by the observational data of satellites. However, WDM and CDM galaxies both occupy the same parameter space and the two populations are not separable. The same is true for the metallicity - stellar mass relation shown in fig. 9.4. The color coding is the same as before and observational data of Milky Way and M31 satellites from Kirby et al. (2014) are shown as grey dots and triangles. Again, the CDM simulations as well as the WDM simulations fulfill the relation down to intermediate masses. For lower stellar masses, however, the star formation in the simulations often happens in a single short burst and time resolution of the gas recycling is too poor to resolve in reliable results (for more details see chapter 6 and chapter 7). This leads to the lack of metals in simulations with stellar masses below $10^5 M_{\odot}$.

9.2.4 Stellar ages

Since structure formation is slightly delayed in WDM we want to look at the stellar formation times. In fig. 9.5 we show the mass averaged stellar age of the galaxies as a function of stellar mass. We additionally show the mean (solid line), 1σ region (shaded area) in the same color coding as before and observational data taken from Weisz et al. (2014) as grey circles. While the average formation times of stars in CDM galaxies scatter around a stellar age of ≈ 10 Gyr, the WDM galaxies seem to form slightly later with a mean age around 8 Gyr and struggle to reproduce the observations of galaxies at intermediate mass that were in place very early ($\langle T_{\text{age}} \rangle > 10$ Gyr). In the CDM simulations those galaxies usually form stars before the reionizing background sets in, but are quenched during reionization leading to a very old average

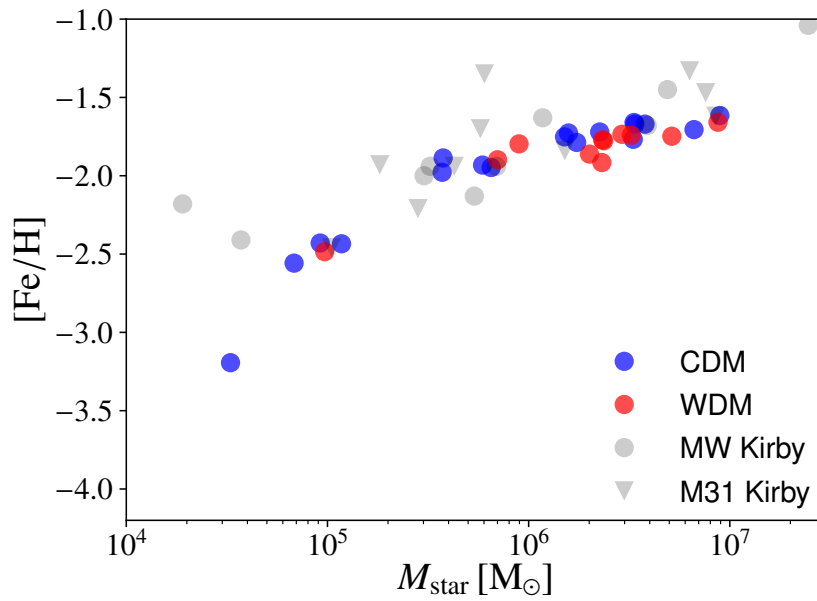


Figure 9.4: Metallicity - stellar mass relation. Blue and red circle denote CDM and WDM simulations, respectively. Observations of Milky Way and M31 satellites from Kirby et al. (2014) are shown as grey dots and triangles, respectively.

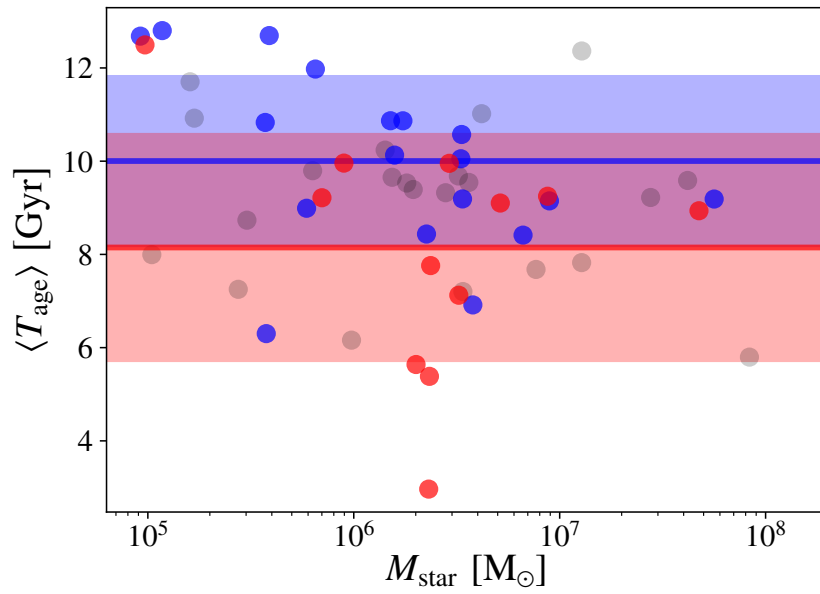


Figure 9.5: Average stellar age as a function of stellar mass. Blue and red circle denote CDM and WDM simulations, respectively and in the same color coding lines and shaded areas represent the mean value and 1σ regions. Observational data (grey circles) are taken from [Weisz et al. \(2014\)](#).

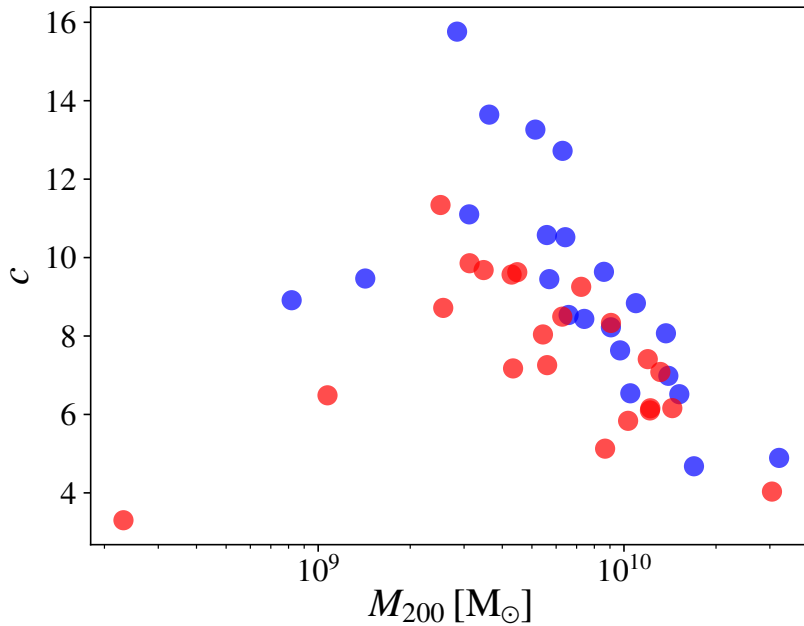


Figure 9.6: The dark matter halo concentrations $c = r_{200}/r_s$ of the CDM run (blue) and WDM run (red) as a function of the virial mass of the halo.

stellar age. But in WDM structure formation is delayed (Bode et al., 2001) and halos that already are massive enough to form stars before reionization will most likely still grow enough to continue to form stars and end up with younger populations. In this way, the effect of quenching of ongoing star formation due to the ionizing background is much smaller in WDM compared to CDM. This might also be one reason for the smaller amount of scatter in the stellar mass - halo mass relation (fig. 9.2) for the luminous galaxies in WDM.

9.2.5 Halo structure

Finally we want to investigate the internal dark matter structure of the halos. The concentrations defined by $c = r_{200}/r_s$, where r_s is the scale radius of a Navarro-Frenk-White (NFW) profile (Navarro et al., 1996) fit to the dark matter component of the halos, we show in fig. 9.6. In agreement with previous studies on warm dark matter structure formation (Macciò et al., 2012b) the concentrations of the halos in the WDM simulations lie well below their CDM counterparts. This is correlated with the later formation times for WDM structures that hence collapse at a lower background density.

Another very sensible quantity to look at is the inner logarithmic dark matter

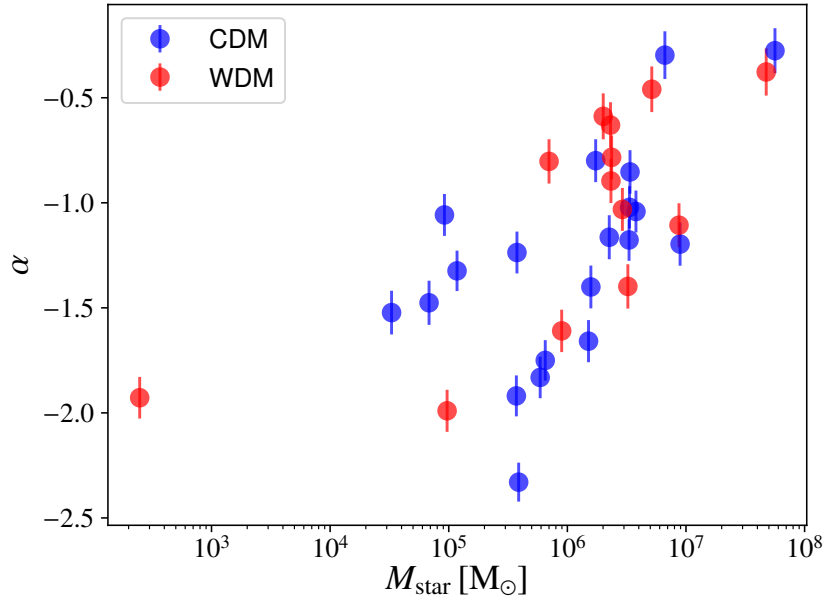


Figure 9.7: The logarithmic inner dark matter density slope α of the CDM (blue) and WDM (red) halos as a function of stellar mass.

density slope α . A value of $\alpha = 0$ indicates a cored profile while $\alpha = -1$ is the inner slope of a Navarro-Frenk-White profile (Navarro et al., 1996). In fig. 9.7 we show the inner logarithmic dark matter density slope as a function of stellar mass for the CDM runs (blue) and WDM runs (red). As already pointed out in previous work (Tollet et al., 2016) we see the trend of higher stellar masses producing more and more cored profiles in this mass range. On the other hand, galaxies with little star formation tend to live in very steep dark matter profiles. The comparison between CDM and WDM in fig. 9.7 shows that the slope is predominantly related to the stellar mass. One could argue that for the low stellar mass end the WDM galaxies usually live in much more massive halos than CDM galaxies of the same stellar mass (see fig. 9.1) and hence feedback effects have less impact on the central dark matter structure and at stellar masses below $10^6 M_{\odot}$ WDM halos tend to be more cuspy. Unfortunately, we are lacking the data at this stellar mass range (because most WDM halos stay dark) to make it a valid statement. In the one-to-one comparison between individual cdm and wdm halos presented in section 10.2.2 this scenario is supported more significantly.

10 Milky Way satellites

10.1 Simulations









From the redshift $z = 1$ outputs of the cosmological simulations of the galaxies $g1.23e10$, $g1.17e10$, $g9.91e9$ and $g4.48e9$ we proceed as described in chapter 7 by cutting the galaxies from their surroundings, and evolving them in a Milky Way like potential (including a Navarro-Frenk-White (NFW) potential (Navarro et al., 1996) and a Miyamoto & Nagai potential (Miyamoto & Nagai, 1975)) with a gas removal scheme mimicking the effects of ram pressure. Each satellite is then evolved on the same five orbits as for the satellite study in CDM (chapter 7, listed in tab. 7.2), with the exception of the radial infall scenario. All trajectories start at the virial radius of the with the NFW potential associated host halo in the plane of the disk and the satellites will undergo two pericenter passages on all orbits until redshift $z = 0$. We also performed simulations in isolation (no potential, no gas removal) until redshift $z = 0$ to compare with the simulations on a orbit in the potential.

10.2 Results

10.2.1 Mass loss

Now that we know about the effects of WDM on the field dwarfs we want to see if there is a difference in the way galaxies evolve to satellites. To quantify the stellar and dark matter mass loss we show the stellar mass at redshift $z = 0$ inside a sphere of three stellar half mass radii at infall as a function of the maximum value of the circular velocity profile v_{\max} . The color coding of the plots in this section is explained in tab. 10.2. Triangles denote the isolated runs while the filled circles denote the runs on orbit. The circles are

Table 10.1: color coding for the figures 10.1 to 10.3.

	g4.48e9	g9.91e9	g1.17e10	g1.23e10
CDM				
WDM				

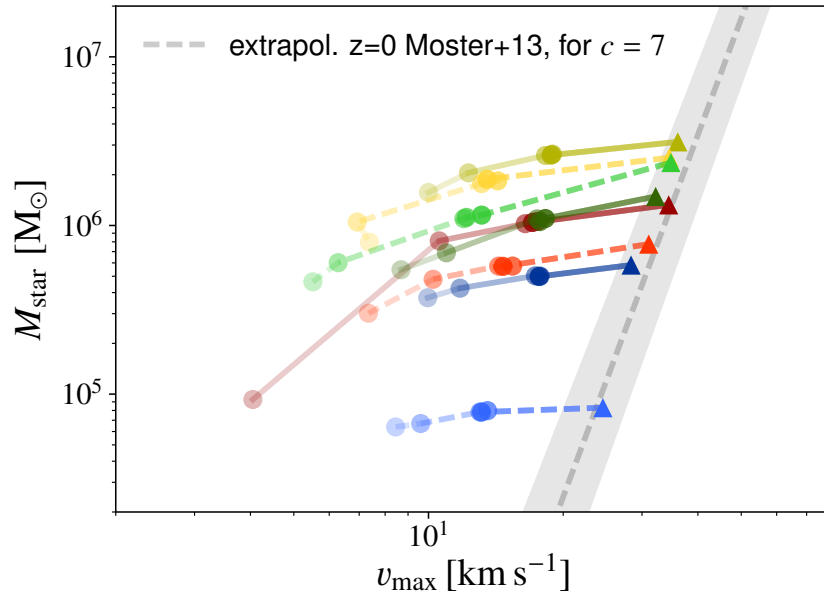


Figure 10.1: The stellar mass within three stellar 3D half mass radii (at infall) as a function of the maximum circular velocity. The gray band shows the Moster relation (Moster et al., 2013) and its errors translated to a function of v_{\max} for a concentration of $c = 7$. Triangles denote the isolated simulations while the filled circles denote the different orbits. The more violent the orbit, the fainter is the color of the dots. For the color coding see tab 10.2.

getting fainter for each orbit listed in tab. 7.2. While all the galaxies lie on the Moster - relation in isolation the WDM counterparts have lower v_{\max} and stellar mass with the exception of $g1.23e9$ that is both more massive and richer in stars. If evolved on a more gentle orbit, stellar masses are not touched at all while v_{\max} already decreases substantially. On the more violent orbits, however, stellar masses are efficiently reduced. The results are comparable to chapter 6. On *orbitV*, however, $g9.91e9$ is stripped heavily while its WDM counterpart seems to be more resistant. We will pick this point up again in section 10.2.2. For now we want to compare the mass loss in WDM and CDM directly. Therefore we take a look at the fractional decrease of v_{\max} given by $f = v_{\max}(t)/v_{\max,\text{infall}}$. In fig. 10.2 we show the ratio of the fractional decrease in WDM and CDM over time. Starting out with a lot of scatter, after the first pericenter passage we already see the trend that mass at radii of the maximum circular velocity is removed more efficiently in WDM. This trend continues after the second pericenter passage. This behavior can be explained by the lower concentrations of the WDM halos that we presented in fig. 9.6. The lower concentration means that the system is less gravitationally bound and therefore mass can be removed more easily. An additional effect is that a lower concentrations at fixed mass is related to a larger scale radius r_s . The maximum circular velocity for an NFW profile is reached at $\approx 2.16 r_s$ thus at larger radii, making it more sensible to mass loss in the outer regions for less concentrated halos. However, we see a similar behavior as in fig. 10.2 for the total mass in a fixed percentage of the initial virial radius which tells us that WDM satellites are more affected by tidal stripping than their CDM counterparts.

%endfigure

10.2.2 Central dark matter density slope

Since the mass loss and survival is linked to the central dark matter structure (for more detail see Kazantzidis et al. (2004a); Peñarrubia et al. (2010)) it is interesting to also look at logarithmic inner dark matter density slope α . We evaluated α between 1 and 2% of the virial radius at infall. In fig. 10.3 we show α over the stellar mass inside three half mass radii at infall. The runs in isolation is denoted by the triangles while the filled circles show *orbitI*. For the isolated runs we see in agreement to chapter 7 the profiles becoming more cored for higher stellar masses (see also (Tollet et al., 2016)). As a consequence the density profiles of WDM galaxies seem to be a little steeper as long as they form less stars. However, for $g1.23e9$ that is more massive and forms more stars in WDM we end up with a flatter profile. In very good agreement to chapter 7 we again see a significant steepening of the central slope due to tidal

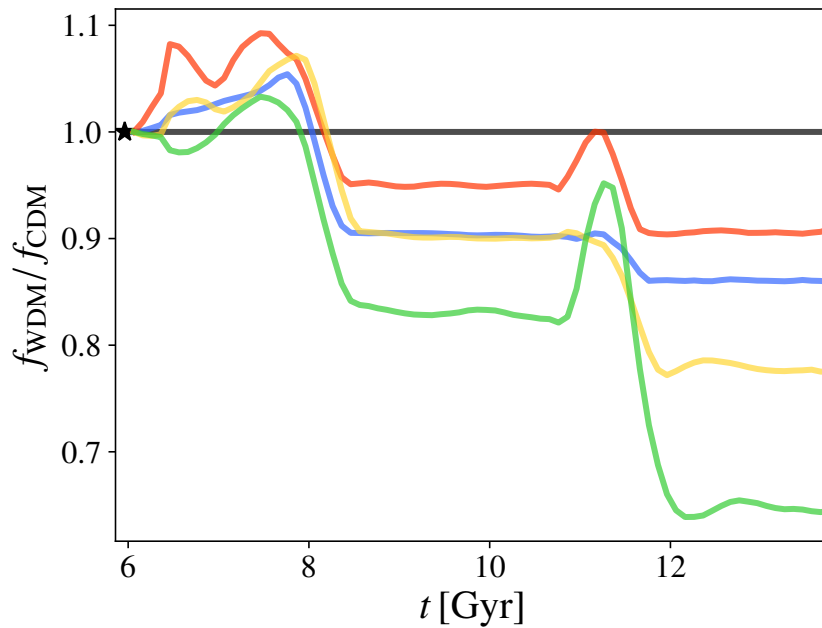


Figure 10.2: Fractional change of maximum circular velocity ($f = v_{\max}(t)/v_{\max,\text{infall}}$) of the WDM run compared to CDM as a function of time. The black line indicates a ratio of 1.

interactions: all values for the central density slope of the stripped satellites lie in the range of -2.0 to -1.5 and show no more dependence on stellar mass.

g9.91e9 shows a remarkable difference in α for WDM and CDM with a value of α_{CDM} around -1 and $\alpha_{\text{WDM}} = -1.75$. This leaves the central region of *g9.91e9* much more vulnerable to stripping and also leads to the huge difference in mass loss on *orbitV* (see fig. 10.1). While Total mass is removed more easily in WDM (see fig. 10.2) because of the lower halo concentrations the survivability and stability of the central region and particular the stars is still linked to the dark matter density slope as well. Since α predominantly depends on the feedback, i.e. star formation, for most WDM galaxies which contain less stars compared to their CDM counterparts the density profile is more cuspy. In the end it is an interplay between concentration and central density slope that decide over the survival of a satellite. So apriori there seems to be no clear difference in the survivability between WDM and CDM satellites.

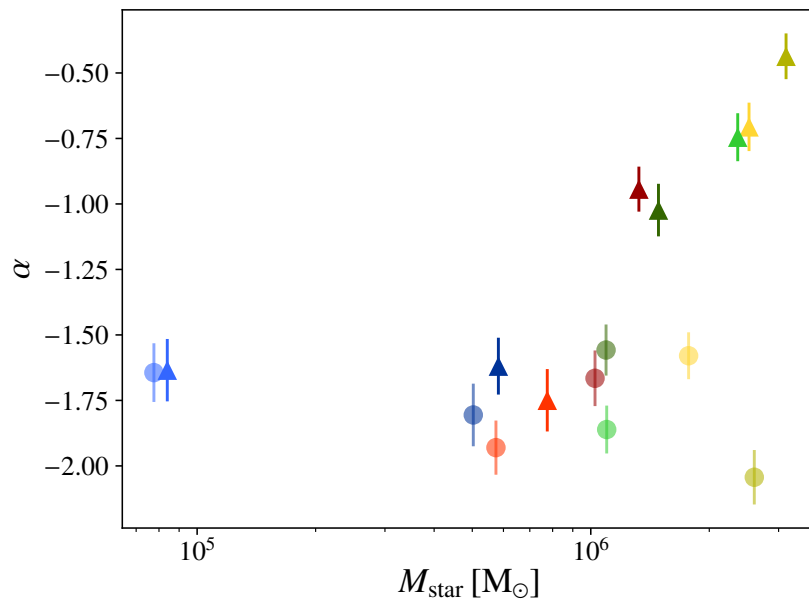


Figure 10.3: Logarithmic inner dark matter density slope α over the stellar mass inside three half mass radii at infall. Triangles denote the runs in isolation while circles show *orbitI*. For the color coding see tab. 10.2.

Part V

Summary and conclusions

10.3 Summary

In this thesis I have presented the investigation of a large sample of cosmological simulations of dwarf galaxies and simulations of their evolution as satellite galaxies in a Milky Way like halo. This study which was performed in a Λ CDM Universe (part III) I have repeated in part IV in a Λ WDM scenario.

In chapter 6 I have presented a set of 27 cosmological hydrodynamical simulations of the formation of several galaxies around the threshold mass of galaxy formation with halo masses (at $z = 1$) between $5 \times 10^8 < M_{200} < 2 \times 10^{10} M_{\odot}$. Initially selected from a low resolution box, we performed zoom-in simulations of the selected halos to reach very high mass resolutions of a few hundred solar masses and be able to resolve the innermost few hundred parsec of the galaxies.

From the sample of 27 halos 19 end up forming a luminous galaxy with stellar masses between 5×10^8 and $2 \times 10^{10} M_{\odot}$. We showed that the formed galaxies are able to reproduce the size-velocity dispersion relation and the stellar mass metallicity relation in comparison with dwarf galaxies and satellites of the Milky way and M31. The large range in star formation histories induces a large scatter in the stellar mass - halo mass relation.

To investigate the scatter we compared the mass accretion and the star formation histories of four halos with the same total halo mass but a range of stellar masses. We showed that mergers have strong impact on the star formation rate as this mass scale and the scatter in stellar mass can be explained by the diversity of merging histories. If the mass accretion is too slow and even before the onset of the UV background a density high enough for star formation can not be reached the halo will very probably end up dark.

We have further investigated the dark matter halo response on baryons in terms of the central dark matter density slope and observed a clear correlation with the stellar mass fraction of the halo. Below stellar masses of $10^6 M_{\odot}$, however, feedback is not effective enough to influence the dark matter structure.

To investigate the evolution of Milky Way satellites I used a total of seven halos (5 luminous and 2 dark) with a virial mass in the range 4×10^9 to $10^{10} M_{\odot}$ from the original sample. I modeled the central halo with an analytic potential of halo (NFW) plus disk (Miyamoto & Nagai), and I run the simulations from redshift one until redshift zero. I used five different orbits (plus a radial orbit) for a total of 42 simulations. Each galaxy was also evolved “in isolation” meaning without the presence of the central halo for the same amount of time as our “orbit” runs. I also added an analytic model for ram pressure and we test the results of our analytic potential against a live halo.

I found that our cosmological initial conditions differ from model (pre cooked)

galaxies in their kinematics: our galaxies, even before accretion do not have a well defined rotating stellar disk and are dispersion supported, with an average value of v_ϕ/σ of 0.14, and as low as 0.04.

While orbiting around the central host, all galaxies lose a considerable fraction of their halo mass, as a consequence they drift away from the widely used abundance matching relations, due to a reshuffling of the mass rank order of the satellites. Only the more extreme orbits, with small pericenter distances are effective in stripping the stellar component too, and the stripping is substantial only for our most massive (and extended) galaxies. Star formation is strongly suppressed after the infall (in comparison with the isolation run), this happens regardless of the presence or absence of ram pressure.

The environment has different effects on different scaling relations. In the stellar mass - metallicity plane, galaxies, even when they lose stellar mass, tend to keep an almost constant metallicity, due to the lack of strong metallicity gradients in the galaxy. In the size - velocity dispersion relation, galaxies move substantially, becoming more extended and reducing their velocity dispersion (due to dark matter stripping). This explains the overall large observed scatter in the $r - \sigma$ plane.

Finally, the interaction with the host leads to a flattening of the stellar velocity dispersion profiles of the satellites, possibly due to the potential perturbation redistributing the stellar orbits into a more “thermalized” system.

The dark matter component is also very strongly perturbed, first of all the removal of particles from the outer part of the halos does not happen in an “onion-like” fashion, with the external layers removed first. The whole density profile reacts to the accretion and even the most internal regions are affected by mass removal even if at a lower degree of the external ones. This implies an overall suppression of the circular velocity curves with respect to the isolation runs, even in the central part.

I found a correlation between the initial (at infall) inner dark matter density slope and the efficiency of mass removal and satellite survival that is in good agreement with previous studies. Cored satellites are less resilient to stripping and tidal forces and are more prone to lose a very large fraction of their dark matter mass (if not all of it) on orbits with close pericenter passages. Some cored satellites are so heavily stripped in their dark matter component that they end up being almost entirely stellar dominated within three stellar half mass radii. Stars are also more easily stripped when embedded in a halo with a flat density profile, even though to a lower extent.

I witnessed a steepening of the central slope of the dark matter profile during accretion, with more extreme orbits ending up with the most cuspy dark matter profiles. Even profiles that initially (before accretion) have a dark matter density profile shallower than NFW (due to baryonic effects) evolve into cuspy

profiles with slopes consistent with pure N-body simulations when set on orbits with small pericenter passages (7-20 kpc). Interestingly also our dark halos (without stars) do steepen their profiles.

In part IV I repeated the study on dwarf galaxies and Milky Way satellites for a 3 keV warm dark matter model. I presented a sample 42 cosmological simulations of 21 halos that were run both in CDM and WDM.

As expected from the damping of the power spectrum the virial masses of the WDM halos lie well below their CDM counterpart for masses below $10^7 M_{\odot}$. Halos at larger masses are much less affected.

Like the CDM galaxies, in WDM the galaxies fulfill the extrapolated Moster - relation even with slightly less scatter. The critical mass for halos to host luminous galaxies is much higher in WDM, where we find a lot of dark halos up to a halo mass of $6 \times 10^9 M_{\odot}$. Further WDM seems to allow a larger range of masses where one finds both dark and luminous halos.

I found that WDM and CDM galaxies show no different behavior in the observable dispersion - size and metallicity - stellar mass relation.

I have further investigated the average stellar formation times and finally found a way to distinguish the two populations: though there is large scatter in the formation times in the observations as well as in the simulation, on average the WDM galaxies form slightly later, around 8 Gyr ago while CDM galaxies form on average at 10 Gyr. In addition WDM struggles to reproduce galaxies at masses around $10^6 M_{\odot}$ with mean stellar ages of 12 Gyr, i.e. that formed in the early Universe before the UV background sets in.

In agreement with previous work we find that the WDM halos are less concentrated compared to their CDM counterparts. The central dark matter density slope, on the other hand, is not directly affected by WDM but through the lower star formation efficiency. The few data points in the relevant mass range suggest that below stellar masses of $10^6 M_{\odot}$ the lower star formation efficiency in WDM galaxies causes a slightly steeper central slope at given stellar mass.

I used four galaxies of the WDM sample and their CDM counterparts to simulate their evolution in a Milky Way potential as described above.

I witnessed the lower concentrations of the WDM halos causing the halos to be more sensitive to mass loss through tidal stripping. Thus their deviation from the stellar mass - halo mass relation is more distinct.

However, the survival of the stellar component of the satellites is also related to central dark matter density slope which for WDM galaxies with a lower star formation efficiency can be much lower. In the end, one of the CDM satellites is stripped close to the point of disruption while its counterpart, showing a much more cuspy profile, is less affected. Since survival depends on both concentration and central slope, neither WDM nor CDM satellites are a priori more likely to survive.

10.4 Final conclusions and outlook

Within this thesis I wanted to test if hydrodynamical high resolution simulations of galaxies at the lower end of the mass spectrum make predictions that, if compared to current observational data, challenge the current model of structure formation. I have shown that observable scaling relations and their scatter for field galaxies and satellites of M31 and the Milky Way are reproduced. The simulations suggest that baryonic effects on the central dark matter density slope are much less effective at the low mass end of galaxy formation and cease to have any effect below a stellar mass of $10^6 M_{\odot}$. Further, the central slope, even if flattened by star formation and feedback before accretion, is effectively steepened by tidal stripping. This means that an unambiguous observation of a core in a low mass ($M_{\text{star}} < 10^6 M_{\odot}$) galaxies and especially in low mass satellites forces us to reconsider (at least) the cold and collisionless dark matter model.

To explore the effects of a thermal warm dark matter candidate on the above mentioned predictions I repeated the simulations in a warm dark matter scenario with a WDM particle mass of 3 keV. I have shown that using observable scaling relation one can not distinguish galaxies that formed in WDM from those who formed in CDM. Average stellar formation times might be a tool to differentiate between CDM and WDM. My simulations suggest that WDM galaxies struggle in reproducing enough galaxies whose stellar mass was in place already in the early Universe. Additionally, the change in the luminous fraction will have a consequence on the satellite and dwarf galaxy number counts in cosmological volume simulations. Thus introducing a slightly warm dark matter can, without affecting the halo mass function at relevant scales, reduce tension concerning the missing satellite problem besides the effects of baryonic feedback. This is interesting since some recent cosmological volume simulation, e.g. the Illustris simulation (Vogelsberger et al., 2014a), show still a humble overprediction of the low mass end of the luminosity function despite of stellar feedback. A warm dark matter candidate that is able to produce kpc scale cores in low mass galaxies is excluded by current constraints on the velocity dispersion of WDM (Iršič et al., 2017) and would very likely prevent the formation of dark galaxies in the first place (Macciò et al., 2012b). Furthermore WDM had no influence on the generation of very cuspy central density profile of Milky Way satellites through tidal effects. Hence an observation of a cored profile in such an object would have to be explained by more drastic change in the dark matter model than a lower particle mass. Interacting dark matter models like coupled dark energy (Penzo et al., 2016) or self interacting dark matter (Vogelsberger et al., 2014b) might provide an answer here. On the other hand, very recent analysis of stellar kinematics of the Milky Way

satellite Sculptor seems to suggest a cuspy profile that is consistent with the prediction of CDM ([Massari et al., 2018](#)).

In my opinion the Λ CDM model is the best and easiest model that provides an explanation to a plenty of observations in cosmology, structure formation, stellar and galactic kinematics and cluster interactions. I have come to the conclusion that up-to-date observation of dwarf galaxies and satellite do not necessarily represent a problem for Λ CDM.

The more we learn about star formation, feedback and other sub-grid physics implemented in simulations, the better can baryonic processes be modeled and the contribution of baryons to the alleviation of the small scale crisis be clarified.

Anyway, as long as the dark matter particle has not been detected, CDM stays a speculation, although a nice one.

Appendix

10.5 List of Figures

2.1	The bullet cluster shows the collision of two galaxy clusters, the lensing mass is shown in blue, X-rays from the hot gas in magenta.	9
3.1	The cosmic microwave background temperature anisotropies by Adam et al. (2016).	12
3.2	Stellar mass-halo mass relation by Moster et al. (2013)	20
3.3	Comparison of observations (SDSS, CFA and 2d FGRS) and large scale structure in the Millenium simulation by Springel et al. (2006).	20
3.4	Halo mass function for dark matter simulations of a cluster and a Milky Way size halo and galaxy mass function of the Virgo cluster and Milky Way satellites. The mass is expressed in terms of the circular velocity normalized to the host halo circular velocity (Moore et al., 1999).	22
3.5	The logarithmic inner dark matter density slope alpha as a function of star formation efficiency, the ratio of stellar and virial mass of the halo (Tollet et al., 2016).	22
3.6	Dark matter power spectrum for the Planck 2015 cosmology (Ade et al., 2016) for cold (blue) and warm thermal relic dark matter with a particle mass of 3 keV (red) at redshift $z = 99$.	25
3.7	Concentration mass relation for CDM (black circles), 1 keV (red diamonds), 0.5 keV (green triangles) and 0.25 keV (blue squares) simulations performed by Schneider et al. (2012).	25
3.8	Density profiles for CDM (black) and WDM models that are associated with thermal velocities of particles with masses between 0.05 (WDM5) and 2 keV (WDM1).	26
6.1	The mass accretion history of our simulations. Solid (dotted) lines indicate halos that are "centrals" ("satellites") at $z = 0$. Red is used for luminous satellites, while black represents dark ones.	40
6.2	The stellar mass halo mass relation for our simulated galaxies at $z = 1$. The colorful points are halos with stars, while the red empty circles represent dark halos. The abundance matching relations from Moster et al. (2013) and Behroozi et al. (2013) are shown in black and cyan respectively, the dashed lines indicate the extrapolation to lower masses.	41

6.3	The gas to total mass ratio as a function of stellar mass. The grey dashed line represents the cosmic value $\Omega_b/\Omega_m = 0.155$ for the WMAP7 cosmology. The galaxy color coding is the same as in figure 6.2.	43
6.4	The gas to total mass ratio as a function of virial mass. The grey dashed line represents the cosmic value $\Omega_b/\Omega_m = 0.155$ for the WMAP7 cosmology. The galaxy color coding is the same as in figure 6.2, while empty circles represent dark halos (i.e. halos that did not form stars).	44
6.5	The cold gas mass fraction as function of stellar mass. Cold gas is defined as gas with $T < 15000\text{K}$. The galaxy color coding is the same as in figure 6.2.	44
6.6	The 2D half mass radius vs. the line of sight stellar velocity dispersion. Simulation results are color coded as in figure 6.2, the error bars represent the $1 - \sigma$ scatter from ten different projections. Crosses with error bars represent observational data from Collins et al. (2013), see text for more details.	46
6.7	Same as figure 6.6 but using a random redshift between 1 and 3 to compute the properties of the galaxies.	46
6.8	Stellar mass - metallicity relation. Observations from Kirby et al. (2011, 2013) are represented by black and grey symbols with error-bars. Simulation results are color coded as in figure 6.2; the triangles represent an upper limit to the satellite metallicity.	47
6.9	Galaxy star formation histories computed over a period of 100 Myrs. The galaxies are ordered with decreasing total mass (as in table 6.2). The values of the stellar masses are reported in each single box. The color coding is the same as in figure 6.2.	48
6.10	Cumulative stellar mass growth up to $z = 1$. Simulations are color coded according to their final stellar mass (right side bar). Observations from Weisz et al. (2014) are also limited to $z = 1$ and are shown in grey.	49
6.11	Logarithmic slope of the dark matter halo profiles in the hydro simulation (color symbols) and in the dark matter only simulation (black dots). The solid line shows the fitting formula proposed in the NIHAO-IV paper (Tollet et al. 2016). The slope α is computed between 1 and 2% of the virial radius, while the error bars represent the uncertainty from the fitting routine.	50

6.12	Logarithmic slope of the dark matter halo profiles in the hydro simulation (color symbols) and in the dark matter only simulation (black dots) as a function of galaxy stellar mass. The slope α is computed between 1 and 2% of the virial radius.	51
6.13	Logarithmic slope of the dark matter halo profiles at the scale of the half mass radius. Color symbols represent the hydro simulation (same scheme as previous plots), the black squares the dark matter only runs.	52
6.14	The star formation rate (upper panels), the mass accretion history (middle panels) and the fraction of stars form from in-situ vs. ex-situ gas particles (lower panesl). The results are shown for four galaxies with similar halo mass at $z = 1$, but very different stellar mass. There is a clear correlation between mergers, i.e. sudden jump in the mass accretion history, and strong star formation episodes.	54
6.15	Mass accretion history of luminous and dark halos with similar $z = 1$ masses. The grey dash line shows the characteristic mass M_c (mass at which halos on average have lost half of their baryons) as computed by Okamoto et al. 2008.	55
7.1	Visualization of the orbits (<i>orbitI</i> to <i>orbitV</i>) presented in Table 7.2 from infall to 5.7 <i>Gyr</i> after infall. The color coding is the same as in Table 7.2.	60
7.2	Projection of <i>orbitII</i> onto the $x - z$ plane comparing the evolution in an analytic potential (blue), in a live halo with 10^5 (green) and 10^7 (red) dark matter particles. A star marks the start of the orbit while the dot marks the end.	60
7.3	Amount of rotation along the axis of total stellar angular momentum of the stars compared to stellar velocity dispersion as a function of stellar mass.	61
7.4	The stellar mass within three stellar 3D half mass radii (at infall) as a function of the maxium circular velocity. The gray band shows the Moster relation and its errors translated to a function of v_{\max} for a concentration of $c = 7$. Triangles denote the isolated simulations while the filled circles denote the different orbits. The more violent the orbit, the fainter is the color of the dots.	62
7.5	Evolution of the dark matter mass in terms of the dark matter mass at infall of the seven satellites on <i>orbitII</i> . Only the mass in 10% of the virial radius at infall is considered.	64

7.6	Evolution of the dark matter mass in terms of the dark matter mass at infall for <i>satII</i> on the five orbits. Only the mass in 10% of the virial radius at infall is considered.	65
7.7	Evolution of the stellar mass of the 5 luminous satellites before (dashed) and after (solid) the infall time ($z = 1$). Isolated runs are shown with darker colors while orbits (specifically <i>orbitIII</i>) are shown with fainter ones. The stellar mass is shown in terms of the stellar mass at time $z = 0$	66
7.8	Metallicity as a function of the stellar mass. The colored triangles denote the isolated simulations while the filled circles denote the different orbits. The more violent the orbit, the fainter is the color of the dots. Observations of Milky Way and M31 satellites from (Kirby et al., 2014) are shown as grey dots and triangles, respectively.	67
7.9	Projected velocity dispersion inside the stellar 2D half mass radius as a function of the stellar 2D half mass radius. colored triangles denote the isolated simulations while the filled circles denote the different orbits. The more violent the orbit, the fainter is the color of the dots. Observations of Milky Way and M31 satellites (for references see section 7.2.2) are shown as grey dots (and a star for the recently discovered satellite Crater 2) and triangles, respectively.	68
7.10	Three dimensional velocity dispersion of the stellar particles on <i>orbitIII</i> evaluated at infall (solid), 3 Gyr and 7.8 Gyr ($z \approx 0$) (faint, solid). Grey points denote line of sight velocity dispersion measurements from Walker et al. (2009) of the nine most massive Milky Way satellites rescaled by a factor of $\sqrt{3}$ (Wolf et al., 2010).	69
7.11	Circular velocity profiles for the five luminous satellites for the isolated run (black) and the orbits (color coding as before). The more violent the orbit, the fainter is the line color. Grey points denote line of sight velocity dispersion measurements from Walker et al. (2009) of the nine most massive Milky Way satellites rescaled by a factor of $\sqrt{3}$ (Wolf et al., 2010).	71
7.12	Dark matter density profile of all the satellites in isolation (black) and on the orbits (color coding as before) at redshift $z = 0$. The more violent the orbit, the fainter is the line color. The profiles are shown from twice the softening length up to the virial radius at infall.	72

7.13	Inner logarithmic slope of the dark matter density profile α fitted between 1% and 2% of the virial radius as a function of stellar mass inside three 3D half mass radii. Stars denote measurements at infall, while triangles denote the isolated simulations and filled circles the orbit runs at redshift $z = 0$. The more violent the orbit, the fainter is the color.	74
7.14	Time evolution of the deviation of α on <i>orbitIV</i> and <i>orbitV</i> from α_{iso} (for the isolated runs) for <i>satI</i> , <i>satII</i> and <i>satIII</i> , respectively. The stars denote the time where there are less than 150 dark matter particles left inside a sphere of a radius of 1% r_{200}	75
7.15	Dark matter mass enclosed in a constant sphere with a radius of three stellar half mass radii at infall on the individual orbits compared to the isolated run as a function of the central dark matter density slope at infall α_{infall}	77
7.16	Dark matter (dots) and stellar (stars) mass enclosed in a constant sphere with a radius of three stellar half mass radii at infall on <i>orbitIV</i> compared to the isolated run as a function of the central dark matter density slope at infall α_{infall}	78
9.1	Virial mass ratio of WDM to CDM run as a function of virial masses in CDM. The black line indicates the ratio of one and purple points are the simulation data.	85
9.2	Stellar mass versus the virial mass of the halo for the CDM (blue) and WDM (red) simulations. On the second y -axis the luminous fraction of satellites at given halo mass is shown as solid lines. The grey dashed line and band visualizes the extrapolation of the Moster - relation (Moster et al., 2013) to the low mass end and its scatter.	86
9.3	Velocity dispersion - size relation. Blue and red circles denote CDM and WDM simulations, respectively and observations of Milky Way and M31 satellites (for references see section 9.2.3) are shown as grey dots and triangles, respectively.	87
9.4	Metallicity - stellar mass relation. Blue and red circle denote CDM and WDM simulations, respectively. Observations of Milky Way and M31 satellites from Kirby et al. (2014) are shown as grey dots and triangles, respectively.	89
9.5	Average stellar age as a function of stellar mass. Blue and red circle denote CDM and WDM simulations, respectively and in the same color coding lines and shaded areas represent the mean value and 1σ regions. Observational data (grey circles) are taken from Weisz et al. (2014).	90

9.6	The dark matter halo concentrations $c = r_{200}/r_s$ of the CDM run (blue) and WDM run (red) as a function of the virial mass of the halo.	91
9.7	The logarithmic inner dark matter density slope α of the CDM (blue) and WDM (red) halos as a function of stellar mass.	92
10.1	The stellar mass within three stellar 3D half mass radii (at infall) as a function of the maximum circular velocity. The gray band shows the Moster relation (Moster et al., 2013) and its errors translated to a function of v_{\max} for a concentration of $c = 7$. Triangles denote the isolated simulations while the filled circles denote the different orbits. The more violent the orbit, the fainter is the color of the dots. For the color coding see tab 10.2.	94
10.2	Fractional change of maximum circular velocity ($f = v_{\max}(t)/v_{\max,\text{infall}}$) of the WDM run compared to CDM as a function of time. The black line indicates a ratio of 1.	96
10.3	Logarithmic inner dark matter density slope α over the stellar mass inside three half mass radii at infall. Triangles denote the runs in isolation while circles show <i>orbit</i> . For the color coding see tab. 10.2.	97

10.6 List of Tables

6.1	The four different Mass and spatial resolution levels used in our simulations.	38
6.2	Parameters of the simulated galaxies: total halo mass (M_{200}), stellar mass (M_{star}), cold ($T < 15000$) gas mass ($M_{\text{gas}}^{\text{cold}}$), 2D half mass radius (r_h^{2D}), l.o.s. stellar velocity dispersion (σ_v). The last column (Res) indicates the resolution of the simulation, see table 6.1 for more details. Galaxies are listed in order of (decreasing) halo mass, dark halos have zero stellar mass.	39
7.1	Virial dark matter mass, stellar mass, virial radius (defined by an overdensity of $200 \rho_{\text{crit}}$) and dark matter particle mass of the selected subsample of simulations. For all simulations the gravitational softening for the dark matter, stellar and gas particles is $\varepsilon_{\text{DM}} = 31 \text{ pc}$ and $\varepsilon_{\text{gas}} = \varepsilon_{\text{star}} = 14 \text{ pc}$, respectively.	57

7.2	Compilation of the different orbit scenarios with their initial velocity, pericenter distance and orbit inclination with respect to the host galaxy disk. All orbits initiate at the coordinates $x = 210\text{kpc}$, $y = z = 0$. The color indicates the color coding in Fig. 7.1.	59
9.1	Name, virial mass, stellar mass, stellar particle number and dark matter particle mass. Data from the CDM and WDM runs are indicated by blue and red background colors, respectively. The gravitational softening for the stellar particles ranges from $\varepsilon_{\text{star}} = 90\text{pc}$ to $\varepsilon_{\text{star}} = 40\text{pc}$ depending on resolution.	83
10.1	color coding for the figures 10.1 to 10.3.	93

11 Bibliography

- Adam R., et al., 2016, *Astron. Astrophys.*, 594, A1
- Ade P. A. R., et al., 2014, *Astron. Astrophys.*, 571, A16
- Ade P. A. R., et al., 2016, *Astron. Astrophys.*, 594, A13
- Appel A. W., 1985, *SIAM Journal on Scientific and Statistical Computing*, vol. 6, no. 1, January 1985, p. 85-103., 6, 85
- Aumer M., White S. D. M., Naab T., Scannapieco C., 2013, *MNRAS*, 434, 3142
- Baer H., Choi K.-Y., Kim J. E., Roszkowski L., 2015, *Phys. Rept.*, 555, 1
- Banerjee H., Chatterjee D., Mitra P., 2003, *Physics Letters B*, 573, 109
- Bartelmann M., 2012, in *Lecture Notes on Cosmology*. <http://www.ita.uni-heidelberg.de/research/bartelmann/files/cosmology.pdf>
- Bartelmann M., Fabis F., Berg D., Kozlikin E., Lilow R., Viermann C., 2014, preprint, ([arXiv:1411.0806](https://arxiv.org/abs/1411.0806))
- Becker R. H., et al., 2001, *AJ*, 122, 2850
- Behroozi P. S., Wechsler R. H., Conroy C., 2013, *ApJ*, 770, 57
- Benítez-Llambay A., et al., 2017, *MNRAS*, 465, 3913
- Bertschinger E., 2001a, in *Cosmology 2000: Proceedings, Conference, Lisbon, Portugal, 12-15 Jul 2000*. pp 1–25 ([arXiv:astro-ph/0101009](https://arxiv.org/abs/astro-ph/0101009))
- Bertschinger E., 2001b, *ApJS*, 137, 1
- Bertschinger E., Gelb J. M., 1991, *Computers in Physics*, 5, 164
- Blumenthal G. R., Faber S. M., Primack J. R., Rees M. J., 1984, *Nature*, 311, 517
- Bode P., Ostriker J. P., Turok N., 2001, *ApJ*, 556, 93
- Boylan-Kolchin M., Bullock J. S., Kaplinghat M., 2011, *MNRAS*, 415, L40
- Bryan S. E., Mao S., Kay S. T., Schaye J., Dalla Vecchia C., Booth C. M.,

- 2012, [MNRAS](#), **422**, 1863
- Buck T., Macciò A. V., Dutton A. A., Obreja A., Frings J., 2018, preprint, ([arXiv:1804.04667](#))
- Bullock J. S., Kravtsov A. V., Weinberg D. H., 2000, [ApJ](#), **539**, 517
- Bullock J. S., Kolatt T. S., Sigad Y., Somerville R. S., Kravtsov A. V., Klypin A. A., Primack J. R., Dekel A., 2001, [MNRAS](#), **321**, 559
- Caldwell N., et al., 2017, [ApJ](#), **839**, 20
- Chabrier G., 2003, [PASP](#), **115**, 763
- Chan T. K., Kereš D., Oñorbe J., Hopkins P. F., Muratov A. L., Faucher-Giguère C.-A., Quataert E., 2015, [MNRAS](#), **454**, 2981
- Chang J., Macciò A. V., Kang X., 2013, [MNRAS](#), **431**, 3533
- Clowe D., Bradač M., Gonzalez A. H., Markevitch M., Randall S. W., Jones C., Zaritsky D., 2006, [ApJ](#), **648**, L109
- Collins M. L. M., et al., 2013, [ApJ](#), **768**, 172
- D’Onghia E., Besla G., Cox T. J., Hernquist L., 2009, [Nature](#), **460**, 605
- Di Cintio A., Brook C. B., Macciò A. V., Stinson G. S., Knebe A., Dutton A. A., Wadsley J., 2014, [MNRAS](#), **437**, 415
- Dutton A. A., 2012, [MNRAS](#), **424**, 3123
- Dutton A. A., Macciò A. V., 2014, [MNRAS](#), **441**, 3359
- Dutton A. A., Macciò A. V., Frings J., Wang L., Stinson G. S., Penzo C., Kang X., 2016a, [MNRAS](#), **457**, L74
- Dutton A. A., et al., 2016b, [MNRAS](#), **461**, 2658
- Einstein A., 1916, [Annalen der Physik](#), **354**, 769
- Elbert O. D., Bullock J. S., Garrison-Kimmel S., Rocha M., Oñorbe J., Peter A. H. G., 2015, [MNRAS](#), **453**, 29
- Fierlinger K. M., Burkert A., Ntormousi E., Fierlinger P., Schartmann M., Ballone A., Krause M. G. H., Diehl R., 2016, [MNRAS](#), **456**, 710
- Fitts A., et al., 2017, [MNRAS](#), **471**, 3547
- Flores R. A., Primack J. R., 1994, [ApJ](#), **427**, L1
- Friedmann A., 1922, [Zeitschrift fur Physik](#), **10**, 377

- Frings J., Macciò A., Buck T., Penzo C., Dutton A., Blank M., Obreja A., 2017, *MNRAS*, **472**, 3378
- Garrison-Kimmel S., et al., 2017, preprint, ([arXiv:1701.03792](https://arxiv.org/abs/1701.03792))
- Gnedin N. Y., 2000, *ApJ*, **542**, 535
- Governato F., et al., 2012, *MNRAS*, **422**, 1231
- Governato F., et al., 2015, *MNRAS*, **448**, 792
- Grand R. J. J., et al., 2017, *MNRAS*, **467**, 179
- Gunn J. E., Gott III J. R., 1972, *ApJ*, **176**, 1
- Guth A. H., 1981, *Phys. Rev. D*, **23**, 347
- Haardt F., Madau P., 2001, in Neumann D. M., Tran J. T. V., eds, Clusters of Galaxies and the High Redshift Universe Observed in X-rays. ([arXiv:astro-ph/0106018](https://arxiv.org/abs/astro-ph/0106018))
- Haardt F., Madau P., 2012, *ApJ*, **746**, 125
- Ho N., et al., 2012, *ApJ*, **758**, 124
- Hoefl M., Yepes G., Gottlöber S., Springel V., 2006, *MNRAS*, **371**, 401
- Hopkins P. F., Kereš D., Oñorbe J., Faucher-Giguère C.-A., Quataert E., Murray N., Bullock J. S., 2014, *MNRAS*, **445**, 581
- Hubble E., 1929, *Proceedings of the National Academy of Science*, **15**, 168
- Iršič V., et al., 2017, *Phys. Rev. D*, **96**, 023522
- Kang X., van den Bosch F. C., 2008, *ApJ*, **676**, L101
- Kapteyn J. C., 1922, *ApJ*, **55**, 302
- Kauffmann G., White S. D. M., Guiderdoni B., 1993, *MNRAS*, **264**, 201
- Kazantzidis S., Mayer L., Mastropietro C., Diemand J., Stadel J., Moore B., 2004a, *ApJ*, **608**, 663
- Kazantzidis S., Kravtsov A. V., Zentner A. R., Allgood B., Nagai D., Moore B., 2004b, *ApJ*, **611**, L73
- Kazantzidis S., Mayer L., Callegari S., Dotti M., Moustakas L. A., 2017, *ApJ*, **836**, L13
- Keller B. W., Wadsley J., Benincasa S. M., Couchman H. M. P., 2014, *MNRAS*, **442**, 3013

- Kim S. Y., Peter A. H. G., Hargis J. R., 2017, preprint, ([arXiv:1711.06267](https://arxiv.org/abs/1711.06267))
- Kirby E. N., Cohen J. G., Smith G. H., Majewski S. R., Sohn S. T., Guhathakurta P., 2011, *ApJ*, **727**, 79
- Kirby E. N., Cohen J. G., Guhathakurta P., Cheng L., Bullock J. S., Gallazzi A., 2013, *ApJ*, **779**, 102
- Kirby E. N., Bullock J. S., Boylan-Kolchin M., Kaplinghat M., Cohen J. G., 2014, *MNRAS*, **439**, 1015
- Klypin A., 2000, ArXiv Astrophysics e-prints,
- Klypin A., Kravtsov A. V., Valenzuela O., Prada F., 1999, *ApJ*, **522**, 82
- Knollmann S. R., Knebe A., 2011, AHF: Amiga's Halo Finder (ascl:1102.009)
- Komatsu E., et al., 2011, *ApJS*, **192**, 18
- Koposov S. E., et al., 2011, *ApJ*, **736**, 146
- Krawczynski H., Treister E., 2013, *Front.Phys.China*, **8**, 609
- Larson R. B., 1974, *MNRAS*, **169**, 229
- Linde A. D., 2008, *Lect. Notes Phys.*, **738**, 1
- Łokas E. L., Kazantzidis S., Klimontowski J., Mayer L., Callegari S., 2010, *ApJ*, **708**, 1032
- Macciò A. V., Fontanot F., 2010, *MNRAS*, **404**, L16
- Macciò A. V., Kang X., Fontanot F., Somerville R. S., Koposov S., Monaco P., 2010, *MNRAS*, **402**, 1995
- Macciò A. V., Paduroiu S., Anderhalden D., Schneider A., Moore B., 2012a, *MNRAS*, **424**, 1105
- Macciò A. V., Stinson G., Brook C. B., Wadsley J., Couchman H. M. P., Shen S., Gibson B. K., Quinn T., 2012b, *ApJ*, **744**, L9
- Macciò A. V., Mainini R., Penzo C., Bonometto S. A., 2015, *MNRAS*, **453**, 1371
- Macciò A. V., Frings J., Buck T., Penzo C., Dutton A. A., Blank M., Obreja A., 2017, *MNRAS*, **472**, 2356
- Madau P., Shen S., Governato F., 2014, *ApJ*, **789**, L17
- Marinacci F., Pakmor R., Springel V., 2014, *MNRAS*, **437**, 1750

- Martin N. F., et al., 2014, [ApJ](#), **793**, L14
- Massari D., Breddels M. A., Helmi A., Posti L., Brown A. G. A., Tolstoy E., 2018, [Nature Astronomy](#), **2**, 156
- Mayer L., Mastropietro C., Wadsley J., Stadel J., Moore B., 2006, [MNRAS](#), **369**, 1021
- Milgrom M., 1983, [ApJ](#), **270**, 365
- Miyamoto M., Nagai R., 1975, [PASJ](#), **27**, 533
- Moore B., 1994, [Nature](#), **370**, 629
- Moore B., Ghigna S., Governato F., Lake G., Quinn T., Stadel J., Tozzi P., 1999, [ApJ](#), **524**, L19
- Moster B. P., Macciò A. V., Somerville R. S., Johansson P. H., Naab T., 2010, [MNRAS](#), **403**, 1009
- Moster B. P., Naab T., White S. D. M., 2013, [MNRAS](#), **428**, 3121
- Moster B. P., Macciò A. V., Somerville R. S., 2014, [MNRAS](#), **437**, 1027
- Munshi F., Brooks A. M., Applebaum E., Weisz D. R., Governato F., Quinn T. R., 2017, preprint, ([arXiv:1705.06286](#))
- Navarro J. F., Frenk C. S., White S. D. M., 1996, [ApJ](#), **462**, 563
- Noh Y., McQuinn M., 2014, [MNRAS](#), **444**, 503
- Oñorbe J., Boylan-Kolchin M., Bullock J. S., Hopkins P. F., Kereš D., Faucher-Giguère C.-A., Quataert E., Murray N., 2015, [MNRAS](#), **454**, 2092
- Oh S.-H., et al., 2015, [AJ](#), **149**, 180
- Okamoto T., Gao L., Theuns T., 2008, [MNRAS](#), **390**, 920
- Oort J. H., 1932, *Bull. Astron. Inst. Netherlands*, **6**, 249
- Peñarrubia J., Benson A. J., Walker M. G., Gilmore G., McConnachie A. W., Mayer L., 2010, [MNRAS](#), **406**, 1290
- Peccei R. D., 2008, [Lect. Notes Phys.](#), **741**, 3
- Peebles P. J. E., 1984, [ApJ](#), **277**, 470
- Penzo C., Macciò A. V., Casarini L., Stinson G. S., Wadsley J., 2014, [MNRAS](#), **442**, 176
- Penzo C., Macciò A. V., Baldi M., Casarini L., Oñorbe J., Dutton A. A., 2016,

- [MNRAS](#), **461**, 2490
- Perlmutter S., et al., 1998, [Nature](#), **391**, 51
- Perlmutter S., et al., 1999, [ApJ](#), **517**, 565
- Pontzen A., Governato F., 2012, [MNRAS](#), **421**, 3464
- Power C., Navarro J. F., Jenkins A., Frenk C. S., White S. D. M., Springel V., Stadel J., Quinn T., 2003, [MNRAS](#), **338**, 14
- Press W. H., Schechter P., 1974, [ApJ](#), **187**, 425
- Read J. I., Gilmore G., 2005, [MNRAS](#), **356**, 107
- Read J. I., Agertz O., Collins M. L. M., 2016, [MNRAS](#), **459**, 2573
- Riess A. G., et al., 1998, [AJ](#), **116**, 1009
- Rubin V. C., Ford Jr. W. K., Thonnard N., 1980, [ApJ](#), **238**, 471
- Sawala T., et al., 2016a, [MNRAS](#), **456**, 85
- Sawala T., et al., 2016b, [MNRAS](#), **457**, 1931
- Schaye J., et al., 2015, [MNRAS](#), **446**, 521
- Schmidt B. P., et al., 1998, [ApJ](#), **507**, 46
- Schneider A., Smith R. E., Macciò A. V., Moore B., 2012, [MNRAS](#), **424**, 684
- Shen S., Wadsley J., Stinson G., 2010, [MNRAS](#), **407**, 1581
- Silk J., Mamon G. A., 2012, [Research in Astronomy and Astrophysics](#), **12**, 917
- Simpson C. M., Bryan G. L., Johnston K. V., Smith B. D., Mac Low M.-M., Sharma S., Tumlinson J., 2013, [MNRAS](#), **432**, 1989
- Somerville R. S., 2002, [ApJ](#), **572**, L23
- Springel V., 2010, [ARA&A](#), **48**, 391
- Springel V., Di Matteo T., Hernquist L., 2005, [MNRAS](#), **361**, 776
- Springel V., Frenk C. S., White S. D. M., 2006, [Nature](#), **440**, 1137
- Stadel J. G., 2001, PhD thesis, UNIVERSITY OF WASHINGTON
- Stinson G., Seth A., Katz N., Wadsley J., Governato F., Quinn T., 2006, [MNRAS](#), **373**, 1074
- Stinson G. S., Brook C., Macciò A. V., Wadsley J., Quinn T. R., Couchman H. M. P., 2013, [MNRAS](#), **428**, 129

- Tollerud E. J., et al., 2012, [ApJ](#), **752**, 45
- Tollerud E. J., Geha M. C., Vargas L. C., Bullock J. S., 2013, [ApJ](#), **768**, 50
- Tollet E., et al., 2016, [MNRAS](#), **456**, 3542
- Viel M., Lesgourgues J., Haehnelt M. G., Matarrese S., Riotto A., 2005, [Phys. Rev. D](#), **71**, 063534
- Vogelsberger M., et al., 2014a, [MNRAS](#), **444**, 1518
- Vogelsberger M., Zavala J., Simpson C., Jenkins A., 2014b, [MNRAS](#), **444**, 3684
- Wadsley J. W., Stadel J., Quinn T., 2004, [Nature](#), **9**, 137
- Wadsley J. W., Keller B. W., Quinn T. R., 2017, [MNRAS](#), **471**, 2357
- Walker M. G., Mateo M., Olszewski E. W., Peñarrubia J., Wyn Evans N., Gilmore G., 2009, [ApJ](#), **704**, 1274
- Wang L., Dutton A. A., Stinson G. S., Macciò A. V., Penzo C., Kang X., Keller B. W., Wadsley J., 2015, [MNRAS](#), **454**, 83
- Weisz D. R., Dolphin A. E., Skillman E. D., Holtzman J., Gilbert K. M., Dalcanton J. J., Williams B. F., 2014, [ApJ](#), **789**, 147
- Wetzel A. R., Hopkins P. F., Kim J.-h., Faucher-Giguère C.-A., Kereš D., Quataert E., 2016, [ApJ](#), **827**, L23
- Wheeler C., et al., 2017, [MNRAS](#), **465**, 2420
- White S. D. M., Rees M. J., 1978, [MNRAS](#), **183**, 341
- Wolf J., Martinez G. D., Bullock J. S., Kaplinghat M., Geha M., Muñoz R. R., Simon J. D., Avedo F. F., 2010, [MNRAS](#), **406**, 1220
- Zel'dovich Y. B., 1970, [A&A](#), **5**, 84
- Zwicky F., 1933, [Helvetica Physica Acta](#), **6**, 110

Acknowledgements

I would like to thank my two supervisors Björn Schäfer, for raising the money for the graduate college that I was part of, adopting me as my local supervisor in Heidelberg and helping me out with any other problem, and Andrea Macciò, for supporting me over such a long distance from Abu Dhabi, making my trips to Abu Dhabi possible and being a very tolerant project supervisor.

I would also like to thank all my friends and colleagues for all the fun, jokes and science discussions.

Finally, I would like to deeply thank Amanda for taking care of Jaro, me and everything else, while I spent my time finishing this thesis.